

Cluster State Generation in a Phase-modulated Quantum Optical Frequency Comb

Xuan Zhu

Wuhan, Hubei, China

Bachelor of Science, Wuhan University, 2016

A Thesis submitted to the Graduate Faculty
of the University of Virginia in Candidacy for the Degree of
Doctor of Philosophy

Department of Physics
University of Virginia

January 2023

Abstract

Measurement-based quantum computing [1] is a model of quantum computer that begins with preparing a highly entangled quantum state, known as cluster state [2], and is followed by performing measurements on this state to carry out the calculations. Cluster states are crucial resources for measurement-based quantum computing. Quantum optical frequency comb (QOFC), which consists of a lot of two-mode-squeezed states created by an optical parametric oscillator (OPO), provides a highly scalable platform to create continuous variable (CV) cluster state, which have been generated in frequency domain [3], temporal domain [4, 5], spatial domain [6] and hybrid time-frequency domain [7]. All these cluster states require interfering more than one QOFCs.

Here we propose and fully analyze the simplest technique to generate CV cluster states. We use a single QOFC and apply phase modulation to it at frequencies multiple of the comb spacing. The cluster state generated using this method can be n-hypercubic cluster state of arbitrary dimension n, among which 2 dimensional cluster states are resources for universal one-way quantum computing [1].

I will also present the experimental design towards the cluster states generation based on the method mentioned above. I will discuss the design for the optical phase stabilization, the homodyne and heterodyne detection that can be used to perform quadrature measurements.

Acknowledgments

First of all, I would like to express my sincere gratitude to my advisor, Prof. Olivier Pfister. He is very enthusiastic about exploring quantum optics and quantum information, both theory and experiment. I will always remember his advice to start from simple examples that you already know, and use them to solve the complicated things that you don't know. His optimism encourages me to keep trying when facing a problem. I thank him for his patience and trust to give me freedom to let me think on my own. I am really grateful that I can work in his group.

I also would like to thank all the collaborators I have been working with during the last few years. I am very thankful to all my lab mates Chun-Hung Chang, Rajveer Nehra, Miller Eaton, Amr Houssameldin and Carlos González-Arciniegas. We had a lot of inspiring and impressive discussions together. It has been fantastic working with all of you. I also would like to thank our collaborator Prof. Avi Pe'er for his genius ideas and crucial suggestion about our work.

I want to thank my parents. They always support me, encourage me and accompany me with their unconditional love. I would like to thank my husband Zijiao for sharing all the happy and difficult time with me. I also would like thank my son Ryan, who makes the last year of my PhD life so special. I want to thank all of my friends for being with me and adding so many joys to my life in Charlottesville.

Contents

| | |
|---|--------------|
| List of Figures | x |
| List of Tables | xviii |
| 1 Introduction | 1 |
| 2 Quantum optics | 5 |
| 2.1 Field quantization | 5 |
| 2.2 Evolution pictures in quantum mechanics | 7 |
| 2.2.1 Schrödinger picture | 8 |
| 2.2.2 Heisenberg picture | 8 |
| 2.2.3 Interaction picture | 9 |
| 2.3 Quantum state | 11 |
| 2.3.1 Fock state | 11 |
| 2.3.2 Coherent state | 14 |
| 2.3.3 Squeezed state | 16 |
| 2.4 Quantum operators | 20 |
| 2.4.1 Phase rotation operator | 20 |
| 2.4.2 Beam splitter | 21 |

| | | |
|----------|--|-----------|
| 2.5 | Continuous-variable quantum computing | 23 |
| 2.5.1 | Measurement based quantum computing | 23 |
| 2.5.2 | Qubits and qumodes | 25 |
| 2.5.3 | Cluster state | 26 |
| 3 | Hypercubic cluster states generated by the phase modulated quantum optical frequency comb | 31 |
| 3.1 | Gaussian state evolution | 32 |
| 3.1.1 | Symplectic representation of Gaussian unitary transformation | 34 |
| 3.1.2 | Symplectic representation of Gaussian pure state | 37 |
| 3.2 | Finite squeezing and graph errors | 41 |
| 3.2.1 | Effect of a spurious graph edge: bipartite case | 42 |
| 3.2.2 | Effect of spurious graph edges: multipartite case | 47 |
| 3.3 | Phase modulation | 48 |
| 3.4 | Phase modulated quantum optical frequency comb | 53 |
| 3.4.1 | General procedure | 54 |
| 3.4.2 | Generation of 1-d cluster state | 58 |
| 3.4.3 | Generation of 2-d cluster state | 65 |
| 3.4.4 | Generation of 3-d cluster state | 69 |
| 4 | Optical system stabilization | 73 |

| | | |
|----------|--|------------|
| 4.1 | Optical parametric oscillator | 75 |
| 4.1.1 | Optical cavity | 75 |
| 4.1.2 | Nonlinear crystal | 80 |
| 4.1.3 | 4-mirror OPO used in the experiment | 86 |
| 4.2 | Pound-Drever-Hall (PDH) locking | 88 |
| 4.2.1 | PDH locking principles | 88 |
| 4.2.2 | PDH locking setup | 91 |
| 4.3 | Pump and probe phase locking | 94 |
| 4.3.1 | Theoretical calculation | 95 |
| 4.3.2 | Circuit design | 97 |
| 4.3.3 | Experimental setup and locking results | 99 |
| 4.4 | Local oscillator and probe phase locking | 101 |
| 5 | Quadrature measurement by homodyne/heterodyne detection | 104 |
| 5.1 | Fourier transform and sampling | 105 |
| 5.1.1 | Fourier transform basics | 105 |
| 5.1.2 | Data acquisition | 107 |
| 5.2 | Quantum detection | 112 |
| 5.2.1 | Quantum-homodyne detection by balanced frequency-homodyne detection | 112 |

| | | |
|----------|---|------------|
| 5.2.2 | Quantum-homodyne detection by balanced frequency-heterodyne detection | 114 |
| 5.3 | Quantum homodyne measurement of the entangled comb | 116 |
| 5.4 | Quantum heterodyne measurement of the entangled comb | 119 |
| 5.4.1 | Fourier transform spectrum | 120 |
| 5.4.2 | Quadrature measurement | 123 |
| 6 | Conclusion | 131 |
| | Bibliography | 133 |
| | Appendices | 144 |
| | Appendix A Quadrature derivations in quantum heterodyne detection | 145 |
| | Appendix B Virtually imaged phase array for qumode separation | 149 |
| B.1 | Basic principles | 149 |
| B.1.1 | Setup | 149 |
| B.1.2 | Fresnel approximation | 151 |
| B.2 | Experimental and simulation results | 154 |
| B.2.1 | Setup design | 154 |
| B.2.2 | Discussion | 155 |
| | Appendix C Pulsed-squeezing quantum states | 161 |

| | |
|---|-----|
| C.1 Pulsed squeezing in optical parametric oscillator | 162 |
| C.1.1 Single mode squeezing | 163 |
| C.1.2 N-fold single mode squeezing | 164 |
| C.2 Pulsed squeezing with nonlinear crystal | 166 |
| C.2.1 Two mode squeezing | 166 |
| C.2.2 N-fold bipartite squeezing | 167 |

List of Figures

| | | |
|-----|--|----|
| 2.1 | Fock state phase space representation. | 13 |
| 2.2 | Coherent state in phase space. | 15 |
| 2.3 | Squeezed state in phase space. | 18 |
| 2.4 | Beam splitter with two input mode a, b , and two output mode c, d | 22 |
| 2.5 | Circuit-based quantum computing example [11]. | 24 |
| 2.6 | Quantum computing by measuring two-state qubit on lattice [1]. Circles \odot symbolize measurements of σ_z , vertical arrows are measurements of σ_x , while tilted arrows refer to measurements in the x-y plane. | 25 |
| 2.7 | Two-qubit state demonstrating the information teleportation. | 25 |
| 2.8 | Two-qubit cluster state. | 28 |
| 3.1 | Two qumodes connected by a C_Z gate with weak interaction strength ϵ | 43 |

- 3.2 Quantum model of phase modulation at frequency Ω by a 3×3 frequency-domain beamsplitter, Eq.3.56 [57], symbolized by the unphysical gray element that features two frequency-domain “reflective,” and one “transmissive,” possibilities for each input beam (blue lines) at $\omega_{\pm} = \omega_o \pm \Omega$. For simplicity, we didn’t draw modulation sidebands of order greater than 1. An arbitrary input state is given in green, containing 3 qumodes (red lines) indexed by their frequency. A key point is that the carrier qumode at ω_o is coupled by PM to the input vacuum modes. When $|\psi\rangle$ is a coherent state, the output remains a product of coherent states. 50
- 3.3 EOM \mathbf{M} matrix numerical plot. (a) EOM modulation frequency $\Omega = 1$ FSR, $m = 0.2$. (b) EOM modulation frequency $\Omega = 1$ FSR, $m = 1$. . . 52
- 3.4 Principle of cluster state engineering by phase modulation, whose action, here in the limit of small modulation index (first-order sidebands only), is equivalent to beamsplitter mode-coupling, as per the blue lines, of the initial quantum states, in green; (a), classical phase modulation, in which *vacuum* sidebands couple in to the initial quantum state $|\psi\rangle$; (b), phase modulation of the QOFC at the mode frequency spacing: there is no vacuum input and a complex unitary operation on initial state $|\psi\rangle$ is realized. 53
- 3.5 Phase modulation of a single QOFC. An OPO with a single pump frequency, whose half is denoted by the green arrow, creates TMS qumode pairs as indicated by the red dashed lines. Electro-optic phase modulation, or Kerr-medium cross phase modulation, is then done at index m and frequencies $\Omega_{1,2,3}$, all multiple of the comb tooth spacing 54

3.6 Phase modulation of a single QOFC. An OPO with a single pump frequency, whose half is denoted by the green arrow, creates TMS qumode pairs as indicated by the red dashed lines. An EOM applies phase modulation with index m , frequency Ω , and phase ϕ (irrelevant in this case). 59

3.7 \mathbf{V} and \mathbf{U} graphs for the state generated by OPO-extrinsic PM at $\Omega_1=1$ and $r=2.3$, for different m . The pump frequency is equal to the sum of the frequencies of all vertical qumode pairs in the \mathbf{V} and \mathbf{U} graph columns. Note that the mode labeled “0” in the PM spectrum column is any of the QOFC qumodes in the \mathbf{V} and \mathbf{U} graph columns. All self loops that have the same color in each \mathbf{U} graph have a value of 0.02, regardless of the value of m 60

3.8 Plot of the average trace of \mathbf{U} versus the squeezing parameter r , compared to the function $\text{sech}(2r)$. This \mathbf{U} matrix is for the externally modulated QOFC at $\Omega_1=1$ 61

3.9 Effect of graph “trimming” (removing all graph edges smaller than ε_{\min}), on the trace of \mathbf{U} , in the case of the state shown in Fig.3.7 with $m = 0.2$ 62

3.10 Γ plot for PM either external or internal to the OPO. $\Omega_1 = 1$, $\varepsilon_{\min}=0.01$. 64

3.11 (a), \mathbf{V} graph of Fig.3.7, revealing its typical structure for 1D cluster state. Two modes that are in the red dashed circle are the EPR-qumodes. (b), compact representation of the graph using EPR macronodes. 65

| | | |
|------|---|----|
| 3.12 | Phase modulation of one QOFC at two modulation frequencies Ω_1 and Ω_2 . Same conventions as Fig.3.6. | 65 |
| 3.13 | (a), square-grid cluster state created with $\Omega_1=1, \Omega_2=10$. Two modes circled by red dashed lines are EPR-qumodes, one of which is on the upper layer and the other one is on the bottom layer. (b), same graph, over EPR macronodes. The width of this square lattice is the number of "spokes" in the graph: $\Omega_2/\Omega_1 = 10$ | 66 |
| 3.14 | Γ plot for PM either external or internal to the OPO. $\Omega_1 = 1, \Omega_2 = 10$. | 67 |
| 3.15 | Cubic cluster state, over $N=400$ EPR macronodes, obtained from $\{\Omega_1, \Omega_2, \Omega_3\} = \{1, 8, 80\}$. Number of "spokes":10. Length: 8 macronodes. Spoke length: 5 macronodes. | 69 |
| 3.16 | Γ plot for PM either external or internal to the OPO. $\Omega_1 = 1, \Omega_2 = 8, \Omega_3 = 80$ | 71 |
| 4.1 | Experimental setup. HWP: half wave plate. PZT: piezoelectric transducer. Moku: Moku:Lab. PC: personal computer. EOM: electro-optic modulator. AOM: acousto-optic modulator. PDH: Pound-Drever-Hall locking. | 74 |
| 4.2 | Different kinds of cavities. (a) Two-mirror cavity. (b) Three-mirror ring cavity. (c) Four-mirror ring cavity. | 75 |
| 4.3 | Optical field inside, reflected and transmitted from a two-mirror cavity. E_0 is the input field. r_1 and r_2 are the reflection coefficient of those two mirrors. | 76 |

| | | |
|------|--|-----|
| 4.4 | Frequency comb generated by a two-mirror cavity. The reflectance coefficients of two mirrors are $r_1 = r_2 = 0.95$. The y axis is the ratio between the intensity of field inside the cavity (Eq. (4.7)) and the maximum value. The x axis is the phase of the field given by Eq. (4.2). | 77 |
| 4.5 | Optical parametric oscillator consists of 4-mirror bow-tie cavity and a nonlinear crystal PPKTP. | 86 |
| 4.6 | Quantum optical frequency comb. | 87 |
| 4.7 | The basic layout for PDH locking. Solid lines are optical paths and dashed lines are signal paths. The signal going to the laser controls its frequency [71]. | 88 |
| 4.8 | PDH error signal when (a) modulation frequency Ω is small ($\Omega \approx$ half of linewidth), (b) Modulation frequency is large ($\Omega = 20$ linewidth). | 90 |
| 4.9 | (a) The experimental setup of OPO PDH locking. (b) Moku:Lab control panel. Upper part is the electronic scheme including mixer, low pass filter, fast and slow controller. Lower part is the PDH locking error signal. | 93 |
| 4.10 | Detector circuit design. The AC and DC outputs are used for balanced homodyne detection. The single PD output signal gives the power of probe beam. | 98 |
| 4.11 | Probe beam power changes with the pump phase scanning. | 99 |
| 4.12 | Pump-probe beam phase lock set up. | 100 |
| 4.13 | Probe beam and LO beat signal amplitude measured with and without pump phase locking. | 101 |

| | | |
|------|--|-----|
| 4.14 | LO and probe beam phase lock experimental setup. | 102 |
| 4.15 | LO and probe beam phase lock error signal. | 103 |
| 5.1 | (a) Sampling a continuous function $f(t)$ using a comb function with sample interval Δt , sampling rate $F_s = 1/\Delta t$. (b) Frequency spectrum of sampled data. $\Delta\nu$ is the bandwidth of signal. | 109 |
| 5.2 | (a) Periodic signal generated based on finite data acquisition time ΔT . (b) Frequency domain data separation. | 111 |
| 5.3 | Intra-modes definition. | 112 |
| 5.4 | Balanced homodyne detection setup. | 112 |
| 5.5 | Balanced heterodyne detection (a) setup, and (b) frequency relation. | 114 |
| 5.6 | Experimental setup for intra-mode squeezing measurement. | 116 |
| 5.7 | Intra-mode squeezing frequency relationship. | 117 |
| 5.8 | Two-mode squeezing inside an OPO cavity mode. | 119 |
| 5.9 | Heterodyne measurement signal bandwidth. | 120 |
| 5.10 | Fourier transform amplitude of different signals. (a) Spectrum of dark noise, measured without any light. (b) Spectrum of LO. (c) Spectrum of LO and probe beam without pump. (d) Spectrum of LO and probe beam with pump. | 121 |

| | | |
|------|---|-----|
| 5.11 | Fourier transform phase of 50 MHz beat signal between LO and probe beam with pump turned on and off. (a) and (c) are 50 MHz phase distribution of 1000 times of measurements with pump turned on and off. There are 5 phase sets in both cases. (b) and (d) show the 50 MHz phase average for 5 different phase sets with pump turned on and off. Error bar shown the range including 95.8% data points. | 124 |
| 5.12 | Probe beam quadrature plot. | 127 |
| 5.13 | Intra-mode Q_{minus} and Q_{plus} variance plot. | 129 |
| B.1 | VIPA setup [77]. A glass plate that is 100 mm thick has 95%-reflection coating on the right surface and 100%-reflection coating on the left surface. There is a window area on the left surface, which has antireflection coating (AR) instead of 100%-reflection coating. The glass plate produces many beams diverging from individual virtual images of the beam waist. These beams interfere and form collimated light. | 150 |
| B.2 | VIPA geometry [79]. θ_i is the incident angle. θ_λ is the dispersion angle of the output light from VIPA. F is the focal length of the convex lens after VIPA. | 151 |
| B.3 | Schematic setup of VIPA. | 154 |
| B.4 | VIPA separates frequencies with difference of 979 MHz. (a) EOM turned off. (b) EOM turned on. | 155 |
| B.5 | VIPA intensity distribution for different incident angles. | 156 |
| B.6 | VIPA intensity distribution for different distance t between two flat mirrors. | 158 |

B.7 VIPA intensity distribution for different initial beam waist. 158

B.8 VIPA intensity distribution for different focal length f before VIPA. . 159

B.9 VIPA intensity distribution for different reflectance r 160

C.1 (a) Single-mode squeezing mode frequency relations. Dashed line indicate the phase-matching bandwidth. Green arrow represents the half of pump frequency. There is only one pump frequency in this case.
 (b) Single-mode squeezing \mathcal{H} -graph. 163

C.2 (a) N-fold single-mode squeezing mode frequency relations. Dashed line indicate the phase-matching bandwidth. Arrows represents the half of pump frequency. (b) N-fold single-mode squeezing \mathcal{H} -graph. . 164

C.3 (a) Two-mode squeezing mode frequency relations. Dashed line indicate the phase-matching bandwidth. Green arrow represents the half of pump frequency. (b) Two-mode squeezing \mathcal{H} -graph. 167

C.4 (a) N-fold bipartite squeezing mode frequency relations. Dashed line indicate the phase-matching bandwidth. Arrows represents the half of pump frequency. (b) N-fold bipartite squeezing \mathcal{H} -graph. 168

List of Tables

| | |
|--|----|
| 2.1 Correspondence between qubit and CV quantum information. \oplus is the exclusive or gate which yields true if and only if the two inputs are the same. | 27 |
|--|----|

Chapter 1

Introduction

Quantum computing has gained tremendous attention and rapid development since it was first proposed in the early 1980s. It is a type of computation that uses the laws of quantum mechanics. Quantum computers are devices that perform quantum computing.

In 1982, Richard Feynman first proposed using a quantum computer to simulate quantum systems [8], which can't be accomplished efficiently by classical computers. A classical computer is binary computing based on calculation unit "bit", which can have values either 0 or 1. A system consists of n bits has 2^n possible states in total, but can only be one state at a given time. Meanwhile, for a quantum computer, the calculation unit is "quantum bit" (qubit), which can be state $|0\rangle$, $|1\rangle$ and linear combination of them $|\psi\rangle = \alpha|0\rangle + \beta|1\rangle$, originated from quantum superposition. $|\alpha|^2$ and $|\beta|^2$ are the probabilities of getting a measurement result of either $|0\rangle$ or $|1\rangle$. When there are n qubits that are all entangled, the system can be in 2^n states simultaneously, although they are not all simultaneously addressable and this alone doesn't explain the power of quantum computing. However, it is possible to develop proper quantum algorithms that can solve certain problems faster than classical computation [9, 10, 11]. For example, in 1994, Peter Shor proposed a quantum algorithms for finding the prime factors of large integers [12], faster than a classical computer. In 2019, Google announced achievement of quantum supremacy

in sampling instances of a quantum circuit using a 53-qubit quantum system [13]. With these advantages demonstrated, quantum computing has attracted more and more research and investment from facilities all around the world.

Over the past decades, several different physical implementations of quantum computing platforms have been developed, such as trapped ions, nuclear spin, neutral atoms, nitrogen-vacancy center, superconducting circuit [13], quantum optics including both photons and squeezed light. In this thesis, I will focus on a squeezed light system, which is used for continuous variable (CV) quantum computing (QC). CV is the opposite to discrete variables (DV). If a QC unit is a two-level system, in other words, the levels are discrete (like spin up or down, there is no other states in between), the unit is qubit and used for DV quantum computing. If a quantum computing unit has continuous basis, we call it qumode, used for CV QC. Squeezed light system has advantages such as high scalability, operating at room temperature and potential for being integrated on chips [14]. The discovery that CV QC can be made fault tolerant at reachable squeezing levels makes it very promising [15, 16, 17]. More details about CV quantum computing can be found in Chapter 2.

Based on the methods that are used to apply quantum operators to achieve different quantum logical gates, there are two different models: circuit-based QC and measurement-based QC. For the circuit-based QC [11], the qubits go through a sequence of quantum gates and measurements to give a calculation results at last. On the other hand, for the measurement-based QC [1], a highly entangled quantum state, named cluster state, is first prepared, and then by applying measurements on each qubit to carry out calculations. Because the measurements will destroy the cluster state, this kind of QC also known as one-way QC. In 2006, Nicolas Menicucci and Peter van Loock proposed CV one-way QC by using CV cluster state as an analogue

to qubit cluster state [18]. Therefore, cluster states are crucial resource for one-way QC. A 2-d cluster state is required to perform universal quantum computing [1] and a 3-d cluster state makes quantum error correction topological encoding possible [19].

Thesis plan

The work presented in this thesis mainly consists of 2 parts. The first part is the theoretical work of generating higher dimensional CV cluster states using phase modulated quantum optical frequency comb. The second part introduces the experiment and data processing methods toward generating and measuring the cluster states. This thesis is organized as follows:

In Chapter 2, I introduce some basic concepts of quantum optics starting from electromagnetic field quantization. Then I discuss the quantum system evolution in three different pictures and present several commonly used quantum states and operators. Also, I will give a brief introduction to CV QC.

Chapter 3 is the main chapter and I present the theoretical work of generating 1-d, 2-d and 3-d cluster states by phase modulated quantum optical frequency comb. I provide the mathematical description of the generation process, including the Gaussian state symplectic representation, graphical calculus for CV cluster state and quantum model of phase modulation and analysis of the graph error caused by omitting the spurious graph edges and finite squeezing.

Chapter 4 switches to the main experiment that is designed based on the theoretical work in Chapter 3. I focus on introducing the stabilization systems of this experiment, including Pound-Drever-Hall locking, pump and probe beam phase locking and LO-probe beam phase locking.

In Chapter 5, I discuss the method of using the quantum homodyne and heterodyne detection combined with Fourier transform to measure the nullifiers of two-mode squeezed state and extract the quadratures information. The mathematical derivation of cluster state covariance matrix using quantum heterodyne detection and Fourier transform is presented in Appendix A.

In Appendix B, I first present the design of virtually imaged phase array (VIPA) to experimentally separate the light that has frequency difference of 1 GHz, which provides the possibility of spatially separating qumodes with different frequencies. Then I discuss how those parameter related to VIPA affects its output field based on some simulation results.

In Appendix C, I analyze the super entanglement structure in a pulsed system, with or without optical parametric oscillator, and show that the squeezing of this super entangled mode can be leveraged to form a highly squeezed eigen-quadrature.

Chapter 2

Quantum optics

In this chapter, I will first introduce some basic concepts of quantum optics. I will start with electromagnetic field quantization and then present some commonly used quantum states and operators. Finally, I will briefly summarize some basics of continuous variable quantum computing. Some good references are [20, 21, 22].

2.1 Field quantization

The classical electric field constrained in a physical volume V solved from Maxwell's equations is

$$\vec{E}(\vec{r}) = i \sum_j \sqrt{\frac{\hbar\omega_j}{2\epsilon_0 V}} \hat{e}_j [a_j e^{i(\vec{k}_j \cdot \vec{r} - \omega t)} - a_j^\dagger e^{-i(\vec{k}_j \cdot \vec{r} - \omega t)}], \quad (2.1)$$

where \hbar is the scaled Plank constant, ϵ_0 is the electric permittivity of vacuum and j is the mode number. A electric field mode is specified by the polarization, frequency ω and wave vector k . For classical electromagnetic wave, the a_j and a_j^* are complex Fourier amplitudes. The quantization of the electromagnetic field can be achieved by defining a_j and a_j^* as mutually adjoint operators a_j and a_j^\dagger , satisfying the boson communication relations

$$[a_j, a_{j'}] = [a_j^\dagger, a_{j'}^\dagger] = 0, \quad [a_j, a_{j'}^\dagger] = \delta_{j,j'}. \quad (2.2)$$

The Hamiltonian for the electromagnetic field is

$$H = \frac{1}{2} \int (\epsilon_0 E^2 + \mu_0 H^2) dV, \quad (2.3)$$

where μ_0 is the magnetic permittivity of vacuum and H is the magnetic field. Substituting the quantized E field and equivalent H field, the Hamiltonian is expressed as

$$H = \sum_j \hbar \omega_j \left(a_j^\dagger a_j + \frac{1}{2} \right), \quad (2.4)$$

where a_j and a_j^\dagger are the annihilation and creation operators for electromagnetic mode j , indexed, e.g. for a plane wave, by wave vector, frequency, and polarization. The photon number operator is defined as $N = a_j^\dagger a_j$. The Hamiltonian of quantum optical field has the same form as the quantum harmonic oscillator. Each quantum mode j has an independent Hilbert space \mathcal{H}_j . The entire field is defined as tensor product of the Hilbert space for all the different modes $\mathcal{H} = \otimes_j \mathcal{H}_j$.

With the definition of creation (a^\dagger) and annihilation (a) operators

$$a = \sqrt{\frac{m\omega}{2\hbar}} \left(\hat{X} + \frac{i}{m\omega} \hat{P} \right). \quad (2.5)$$

We take the parameter $\beta = \sqrt{\frac{m\omega}{\hbar}}$ to have the dimension of inverse length and define a dimensionless operators

$$Q = \beta \hat{X}, \quad (2.6)$$

$$P = \frac{\hat{P}}{\beta \hbar}, \quad (2.7)$$

where Q is amplitude (or position) quadrature and P is phase (or momentum) quadra-

ture. Then we have the photon creation and annihilation operator in the expressions of

$$a = \frac{1}{\sqrt{2}}(Q + iP), \quad (2.8)$$

and

$$Q = \frac{1}{\sqrt{2}}(a + a^\dagger), \quad (2.9)$$

$$P = \frac{1}{i\sqrt{2}}(a - a^\dagger). \quad (2.10)$$

The canonical commutator of amplitude and phase quadratures is

$$[Q, P] = i, \quad (2.11)$$

and they satisfy the Heisenberg uncertainty principle

$$\Delta Q \Delta P \geq \frac{1}{2}. \quad (2.12)$$

2.2 Evolution pictures in quantum mechanics

In quantum mechanics, the time evolution can be described mathematically in three different pictures: Schrödinger picture, Heisenberg picture and interaction picture (also known as Dirac picture).

2.2.1 Schrödinger picture

In Schrödinger picture, the state vectors evolve with time and the operators are time-independent initially. The state vector evolution is given by the Schrödinger equation

$$\frac{d|\psi\rangle}{dt} = -\frac{i}{\hbar}H|\psi\rangle, \quad (2.13)$$

where H is the time-independent Hamiltonian of the system. The solution to the Schrödinger equation equation is

$$|\psi(t)\rangle = U(t, t_0) |\psi(t_0)\rangle, \quad (2.14)$$

where t_0 and t are the initial time and final time of evolution. $U(t, t_0)$ is a unitary operator

$$U(t, t_0) = e^{-\frac{i}{\hbar}H(t-t_0)}. \quad (2.15)$$

Therefore, the expectation value of an operator A_0 is

$$\begin{aligned} \langle A_0 \rangle &= \langle \psi(t) | A_0 | \psi(t) \rangle \\ &= \langle \psi(t_0) | U^\dagger A_0 U | \psi(t_0) \rangle. \end{aligned} \quad (2.16)$$

Here we use A_0 to represent the initial operator which is defined for $t = t_0$.

2.2.2 Heisenberg picture

In Heisenberg picture, the state vectors remain unchanged while the operators evolve with time. Again, A_0 is the initial operator. From Eq. (2.16), the time evolved

operator at t is defined as

$$A(t) = U^\dagger A_0 U. \quad (2.17)$$

Therefore, in Heisenberg picture with the unchanged wave function $\psi(t_0)$, the expectation value of an operator is

$$\begin{aligned} \langle A \rangle &= \langle \psi(t_0) | A(t) | \psi(t_0) \rangle \\ &= \langle \psi(t_0) | U^\dagger A_0 U | \psi(t_0) \rangle, \end{aligned} \quad (2.18)$$

which gives the same result as Eq. (2.16).

Using the expression of U in Eq. (2.15), taking the time derivative of the operator $A(t)$

$$\begin{aligned} \frac{dA(t)}{dt} &= \frac{dU^\dagger}{dt} A_0 U + U^\dagger \frac{dA_0}{dt} U + U^\dagger A_0 \frac{dU}{dt} \\ &= \frac{i}{\hbar} (U^\dagger H A_0 U - U^\dagger A_0 H U) + U^\dagger \frac{dA_0}{dt} U, \end{aligned} \quad (2.19)$$

with the condition that $[U, H] = [U^\dagger, H] = 0$ and A_0 is constant since taken at $t = t_0$ so that $\frac{dA_0}{dt} = 0$, the Eq. (2.19) is simplified to

$$\frac{dA(t)}{dt} = -\frac{i}{\hbar} [A(t), H] \quad (2.20)$$

which is known as Heisenberg equation describing the evolution of operator in Heisenberg picture.

2.2.3 Interaction picture

In interaction picture, also known as Dirac picture, both the state vectors and the operators evolve with time. For simplicity, we consider the case that the Hamiltonian can be written as $H = H_0 + V$, where H_0 is the Hamiltonian of single system (or a

sum of single systems) and V is the Hamiltonian describing the interactions between systems. H_0 and V do not necessarily commute. Writing the Hamiltonian in this form makes it convenient to define that the operators evolve only under the interaction Hamiltonian V and the state vectors evolve only under H_0 . This definition is used to calculate the parametric down conversion process (in Section 4.1.2) and the quantum model of electro-optic modulations (in Section 3.3).

The operator in the interaction picture, $A_I(t)$, can be defined as

$$A_I(t) = U_0 A_H(t) U_0^\dagger = U_0 U^\dagger A_0 U U_0^\dagger, \quad (2.21)$$

where $U_0 = e^{-iH_0 t/\hbar}$ and $U = e^{-iHt/\hbar}$. Here $A_H(t)$ is the operator that evolves with total Hamiltonian H in Heisenberg picture. The time derivative of $A_I(t)$ is

$$\begin{aligned} \frac{dA_I(t)}{dt} &= \frac{dU_0}{dt} A_H U_0^\dagger + U_0 A_H \frac{dU_0^\dagger}{dt} + U_0 \frac{dA_H}{dt} U_0^\dagger \\ &= -\frac{i}{\hbar} (H_0 U_0 A_H U_0^\dagger - U_0 A_H U_0^\dagger H_0) + U_0 \frac{dA_H}{dt} U_0^\dagger \\ &= \frac{i}{\hbar} [A_I, H_0] + U_0 \frac{dA_H}{dt} U_0^\dagger. \end{aligned} \quad (2.22)$$

Use Heisenberg equation Eq. (2.20) to rewrite the second term

$$U_0 \frac{dA_H}{dt} U_0^\dagger = -\frac{i}{\hbar} [A_I, H_0] - \frac{i}{\hbar} [A_I, V]. \quad (2.23)$$

Since H_0 and V are Heisenberg-picture operators, when they commute with themselves at different times, the evolution equation of operators in interaction picture is

$$\frac{dA_I(t)}{dt} = -\frac{i}{\hbar} [A_I, V]. \quad (2.24)$$

Since the state evolves only under H_0 , the state vector in the interaction picture, $|\psi_I\rangle$, is defined as

$$|\psi_I(t)\rangle = U_0 |\psi(t_0)\rangle. \quad (2.25)$$

The state vector evolution equation is

$$\frac{d|\psi_I(t)\rangle}{dt} = -\frac{i}{\hbar} H_0 |\psi_I(t)\rangle. \quad (2.26)$$

2.3 Quantum state

In this section, I will describe several commonly used and important quantum optical states: Fock state, coherent state and squeezed state.

2.3.1 Fock state

Fock states, also known as photon number states, are the eigenstates of the harmonic oscillator Hamiltonian Eq. 2.4. Since this Hamiltonian has the photon number operator $N_j = a_j^\dagger a_j$, Fock states are also the eigenstates of the photon number operator N_j . The eigenvalue of the photon number operator is n_j , thus the eigenstates $|n_j\rangle$ are

$$a_j^\dagger a_j |n_j\rangle = n_j |n_j\rangle. \quad (2.27)$$

Similarly, the the eigenequation of the harmonic oscillator Hamiltonian is

$$(N_j + \frac{1}{2}) |n_j\rangle = (n_j + \frac{1}{2}) |n_j\rangle. \quad (2.28)$$

Here we can review the meanings of operator a_j and a_j^\dagger . They are the lowering

and raising operators for the harmonic oscillator ladder of eigenstates. In terms of photon number, a_j and a_j^\dagger are the annihilation and creation of a photon, which is clear with the expression

$$\begin{aligned} a_j |n_j\rangle &= \sqrt{n_j} |n_j - 1\rangle, \\ a_j^\dagger |n_j\rangle &= \sqrt{n_j + 1} |n_j + 1\rangle. \end{aligned} \tag{2.29}$$

The ground state of the harmonic oscillator is state with $n_j = 0$. The state that has 0 photon is also defined as vacuum state of the field mode. So the vacuum state $|0\rangle$ is

$$a_j |0\rangle = 0. \tag{2.30}$$

The higher excited states can be calculated from the vacuum by successive applications of creation operator. The state vector is

$$|n_j\rangle = \frac{(a_j^\dagger)^{n_j}}{\sqrt{(n_j!)}} |0\rangle. \tag{2.31}$$

The Fock states are orthogonal and complete

$$\begin{aligned} \langle n_j | n_k \rangle &= \delta_{jk}, \\ \sum_{n_j=0}^{\infty} |n_j\rangle \langle n_j| &= 1. \end{aligned} \tag{2.32}$$

These Fock states form an orthonormal basis of the Hilbert space.

Fock state in phase space

The expectation value of P and Q quadratures for Fock state are

$$\begin{aligned}\langle n_j | Q | n_j \rangle &= \langle n_j | \frac{1}{\sqrt{2}} (a_j + a_j^\dagger) | n_j \rangle = 0, \\ \langle n_j | P | n_j \rangle &= \langle n_j | \frac{1}{i\sqrt{2}} (a - a^\dagger) | n_j \rangle = 0.\end{aligned}\tag{2.33}$$

The variance of Q and P quadratures for Fock state are

$$\begin{aligned}\Delta^2 Q &= \langle n_j | Q^2 | n_j \rangle - \langle n_j | Q | n_j \rangle^2 = n_j + \frac{1}{2}, \\ \Delta^2 P &= \langle n_j | P^2 | n_j \rangle - \langle n_j | P | n_j \rangle^2 = n_j + \frac{1}{2}.\end{aligned}\tag{2.34}$$

To represent Fock states in phase space, it is a disk centered at the origin with radius $\Delta P = \Delta Q = \sqrt{n_j + 1/2}$ as shown in Fig.2.1. The vacuum state is the case when $n_j = 0$, which has $\Delta Q = \Delta P = \frac{1}{\sqrt{2}}$.

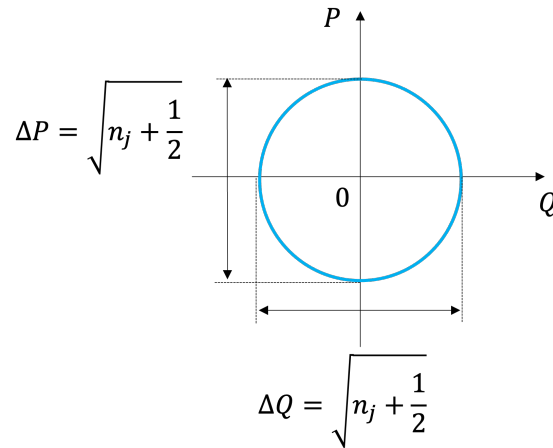


Figure 2.1: Fock state phase space representation.

2.3.2 Coherent state

The coherent state $|\alpha\rangle$ is defined as the the eigenstate of the annihilation operator a

$$a |\alpha\rangle = \alpha |\alpha\rangle, \quad (2.35)$$

where α is the eigenvalue and it is a complex number of the form

$$\alpha = |\alpha|e^{i\phi}, \quad (2.36)$$

with $|\alpha|$ and ϕ are the amplitude and phase of the state $|\alpha\rangle$.

The coherent state can be generated by displacing the vacuum state. The displacement operator is

$$D(\alpha) = e^{\alpha a^\dagger - \alpha^* a}. \quad (2.37)$$

Applying this displacement operator to vacuum state expressed in photon number basis

$$|\alpha\rangle = D(\alpha) |0\rangle = e^{-\frac{|\alpha|^2}{2}} \sum_{n=0}^{\infty} \frac{\alpha^n}{\sqrt{n!}} |n\rangle. \quad (2.38)$$

The expectation of photon number of a coherent state is

$$\langle \alpha | N | \alpha \rangle = |\alpha|^2, \quad (2.39)$$

and its photon number standard deviation is

$$\Delta N = \sqrt{\langle \alpha | N^2 | \alpha \rangle - (\langle \alpha | N | \alpha \rangle)^2} = |\alpha|. \quad (2.40)$$

The expectation of quadratures Q and P for a coherent state is

$$\langle \alpha | Q | \alpha \rangle = \frac{1}{\sqrt{2}} \langle \alpha | a + a^\dagger | \alpha \rangle = \frac{1}{\sqrt{2}} (\alpha + \alpha^*) = \sqrt{2} |\alpha| \cos \phi, \quad (2.41)$$

$$\langle \alpha | P | \alpha \rangle = -\frac{i}{\sqrt{2}} \langle \alpha | a - a^\dagger | \alpha \rangle = -\frac{i}{\sqrt{2}} (\alpha - \alpha^*) = \sqrt{2} |\alpha| \sin \phi. \quad (2.42)$$

and its standard deviation is

$$\Delta Q = \sqrt{\langle \alpha | Q^2 | \alpha \rangle - \langle \alpha | Q | \alpha \rangle^2} = \frac{1}{\sqrt{2}}, \quad (2.43)$$

$$\Delta P = \sqrt{\langle \alpha | P^2 | \alpha \rangle - \langle \alpha | P | \alpha \rangle^2} = \frac{1}{\sqrt{2}}. \quad (2.44)$$

The phase space graph of a coherent state is shown in Fig.2.2. Compared to vacuum state in phase space shown in Fig.2.1, coherent state is a disk with diameter equal to $1/\sqrt{2}$, which is the standard deviation of quadratures Q and P . The center of the disk is displaced from origin along a vector. The vector has the magnitude of $\sqrt{2}|\alpha|$ and its angle is the phase of the coherent state ϕ . The coordinates of the center of the disk is $(\sqrt{2}|\alpha|\cos\phi, \sqrt{2}|\alpha|\sin\phi)$, which are the expectation values of quadratures Q and P as shown in Eq. (2.41).

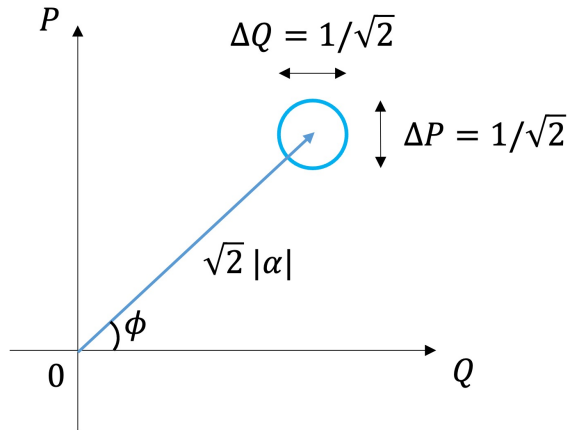


Figure 2.2: Coherent state in phase space.

2.3.3 Squeezed state

The vacuum states and coherent states have the same standard deviation in two quadratures, $\Delta Q = \Delta P = 1/\sqrt{2}$. In this subsection, I will describe squeezed vacuum states, which have less uncertainty than vacuum state in one quadrature and are noisier in the other quadrature to hold the Heisenberg uncertainty. For now, I will focus on the mathematical properties of squeezed state. The experimental generation will be discussed in the Section [4.1.2](#).

Single-mode squeezed state

Single-mode squeezed states are generated by applying squeezing operator to the vacuum state. In Schrödinger picture, the state vector is

$$|0, r\rangle = S(r) |0\rangle, \quad (2.45)$$

where $S(r)$ is the squeezing operator

$$S(r) = e^{\frac{r}{2}(a^{\dagger 2} - a^2)}, \quad (2.46)$$

with r being the squeezing parameter. The single-mode squeezed state is calculated to be

$$|0, r\rangle = \frac{1}{\sqrt{\cosh r}} \sum_{n=0}^{\infty} \frac{\sqrt{2n!}}{2^n n!} \tanh^n r |2n\rangle, \quad (2.47)$$

which can only have even number of photons.

In Heisenberg picture, the annihilation and creation operators evolutions are

$$a(r) = S^\dagger(r)aS(r) = a\cosh r + a^\dagger\sinh r, \quad (2.48)$$

$$a^\dagger(r) = S^\dagger(r)a^\dagger S(r) = a^\dagger\cosh r + a\sinh r, \quad (2.49)$$

which are Bogoliubov transformations. Furthermore, the quadrature transformations are given by

$$Q(r) = S^\dagger(r)QS = Qe^r, \quad (2.50)$$

$$P(r) = S^\dagger(r)PS = Pe^{-r}. \quad (2.51)$$

Using these relations, we can calculate the mean photon number of single-mode squeezed state

$$\langle 0, r | N | 0, r \rangle = \langle 0 | a^\dagger(r)a(r) | 0 \rangle = \sinh^2 r, \quad (2.52)$$

and the standard deviation of photon number is

$$\Delta N = \sqrt{\langle 0, r | N^2 | 0, r \rangle - (\langle 0, r | N | 0, r \rangle)^2} = \frac{1}{\sqrt{2}} |\sinh 2r|. \quad (2.53)$$

The squeezed vacuum state is not vacuum and it has nonzero photon number.

The quadrature expectation values of single-mode squeezed state are

$$\langle 0, r | Q | 0, r \rangle = \langle 0, r | P | 0, r \rangle = 0, \quad (2.54)$$

and the standard deviations are

$$\Delta Q = \frac{e^r}{\sqrt{2}}, \quad (2.55)$$

$$\Delta P = \frac{e^{-r}}{\sqrt{2}}. \quad (2.56)$$

From Eq. (2.55), it is obvious that the noise of phase quadrature P is reduced less than it of the vacuum state and the noise of amplitude quadrature Q is large than it of the vacuum. This state is call phase squeezed vacuum state. The phase space representation of phase squeezed vacuum state is shown in Fig.2.3.

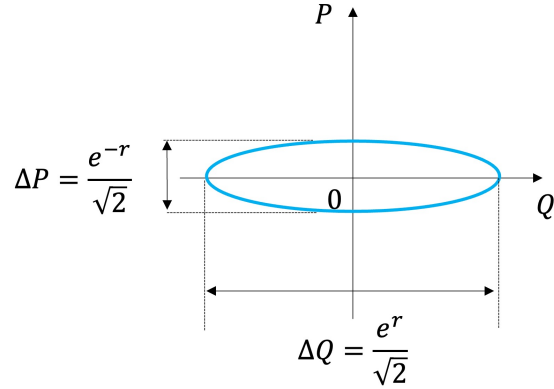


Figure 2.3: Squeezed state in phase space.

Two-mode squeezed state

Single-mode squeezed state is a degenerate case that the quantum optical field has only one frequency. If the states consist of two fields a and b with different frequencies, it is called two-mode squeezed state. The two-mode squeezing operator is

$$S_{ab}(r) = e^{r(a^\dagger b^\dagger - ab)}. \quad (2.57)$$

Two-mode squeezed vacuum state is obtained by

$$S_{ab}(r) |0\rangle_a |0\rangle_b = \frac{1}{\cosh r} \sum_{n=0}^{\infty} \tanh^n r |n\rangle_a |n\rangle_b. \quad (2.58)$$

In this wave vector expression in the Fock state basis, it is obvious to see that the two modes always have the same photon number in two-mode squeezed state.

Solving the Heisenberg equation from the Hamiltonian driving the evolution of Eq. (2.57), $H = i\hbar\kappa(a^\dagger b^\dagger - ab)$, and taking $r = \kappa t$, we obtain the evolution equations of the annihilation and creation operators of the quantum optical fields, i.e., the Bogoliubov transformations for two-mode squeezing

$$a(r) = S_{ab}(r)^\dagger a S_{ab}(r) = a \cosh r + b^\dagger \sinh r, \quad (2.59)$$

$$a^\dagger(r) = S_{ab}(r)^\dagger a^\dagger S_{ab}(r) = a^\dagger \cosh r + b \sinh r, \quad (2.60)$$

$$b(r) = S_{ab}(r)^\dagger b S_{ab}(r) = b \cosh r + a^\dagger \sinh r, \quad (2.61)$$

$$b^\dagger(r) = S_{ab}(r)^\dagger b^\dagger S_{ab}(r) = b^\dagger \cosh r + a \sinh r. \quad (2.62)$$

The squeezed and anti-squeezed quadratures are then given by

$$Q_+(r) = Q_a(r) + Q_b(r) = (Q_a + Q_b)e^r, \quad (2.63)$$

$$Q_-(r) = Q_a(r) - Q_b(r) = (Q_a - Q_b)e^{-r}, \quad (2.64)$$

$$P_+(r) = P_a(r) + P_b(r) = (P_a + P_b)e^{-r}, \quad (2.65)$$

$$Q_-(r) = P_a(r) - P_b(r) = (P_a - P_b)e^r, \quad (2.66)$$

with the standard deviations

$$\Delta Q_+(r) = \frac{e^r}{\sqrt{2}}, \quad (2.67)$$

$$\Delta Q_-(r) = \frac{e^{-r}}{\sqrt{2}}, \quad (2.68)$$

$$\Delta P_+(r) = \frac{e^{-r}}{\sqrt{2}}, \quad (2.69)$$

$$\Delta P_-(r) = \frac{e^r}{\sqrt{2}}. \quad (2.70)$$

Therefore, for two-mode squeezing, the sum of P quadratures and the difference of Q quadratures are squeezed, the noise of which is reduced smaller than the noise of vacuum, while the sum of Q quadratures and the difference of P quadratures are anti-squeezed, the noise of which is greater than that of the vacuum.

2.4 Quantum operators

In the previous section Section 2.3, I introduced the displacement operator and squeezed operator which are used to create coherent state and squeezed state from vacuum. In this section, I will discuss some other commonly used quantum operators including single-mode phase rotation operator and two-mode beam splitter.

2.4.1 Phase rotation operator

The unitary operator associated with field quantization Hamiltonian Eq. (2.4) is given by

$$U_R = e^{-i\omega t(a^\dagger a + \frac{1}{2})}. \quad (2.71)$$

Replacing the phase term $\omega t = \theta$ and ignoring $e^{-i\frac{\omega t}{2}}$ since it is a global phase term and does not affect the state evolution, the unitary operator becomes

$$U_R(\theta) = e^{-i\theta(a^\dagger a)}. \quad (2.72)$$

We can view this evolution from the aspect of operators by solving the Heisenberg equation. The evolution of annihilation and creation operators is given by

$$a(t) = U_R^\dagger a U_R = e^{-i\theta} a, \quad (2.73)$$

$$a^\dagger(t) = U_R^\dagger a^\dagger U_R = e^{i\theta} a^\dagger, \quad (2.74)$$

and therefore using Eq. (2.9) the quadratures evolve as

$$U_R^\dagger Q U_R = Q \cos\theta + P \sin\theta, \quad (2.75)$$

$$U_R^\dagger P U_R = -Q \sin\theta + P \cos\theta. \quad (2.76)$$

From the quadrature evolution, we can see the meaning of operator U_R is rotating the quadratures of a certain state in phase space by an angle θ . Because this phase rotation operator corresponds to free space evolution Hamiltonian, the experimental implementation of phase rotation is changing the path length of a propagating wave.

2.4.2 Beam splitter

The beam splitter (BS) is an important element used in optics. From classical point of view, it can split the incident light into reflected field and transmitted field with reflection coefficient ρ and transmission coefficient τ . With energy conservation, $|\rho|^2 + |\tau|^2 = 1$ must be satisfied. From quantum aspect, the beam splitter always has 2

input port and two output port to make sure this transformation can be implemented by a unitary operator. When there is only one beam incident on the beam splitter, the field incident on the other input port will be considered as vacuum.

Fig.2.4 shows the quantum model of beam splitter. Because of field quantization, we use annihilation operator a and b to represent the two input modes, c and d denote the two output modes. The Hamiltonian of beam splitter is

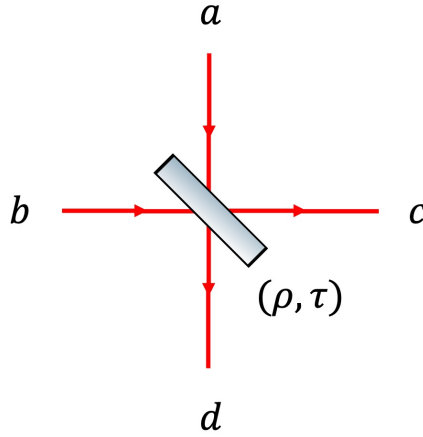


Figure 2.4: Beam splitter with two input mode a , b , and two output mode c , d .

$$H_{BS} = \hbar\kappa(a^\dagger b e^{i\phi} - ab^\dagger e^{-i\phi}), \quad (2.77)$$

where κ is the interaction coefficient and ϕ is the phase difference of two input modes. The unitary operator of beam splitter is therefore given by

$$U_{BS} = e^{-i\theta(a^\dagger b e^{i\phi} - ab^\dagger e^{-i\phi})}, \quad (2.78)$$

where the phase $\theta = \kappa t$, with t being the interaction time of this beam splitter evolution. Solving the Heisenberg equation to get the mode transformation and the

two output modes c and d are

$$\begin{pmatrix} c \\ d \end{pmatrix} = \begin{pmatrix} U_{BS}^\dagger a U_{BS} \\ U_{BS}^\dagger b U_{BS} \end{pmatrix} = \begin{pmatrix} \cos\theta & e^{i\phi}\sin\theta \\ -e^{-i\phi}\sin\theta & \cos\theta \end{pmatrix} \begin{pmatrix} a \\ b \end{pmatrix}. \quad (2.79)$$

Because the phase ϕ can be changed by single mode phase rotation, the beam splitter transform matrix can have different forms. It is convenient to set $\phi = \pi$, with $\rho = \cos\theta$ and $\tau = \sin\theta$, the beam splitter transformation is in the form of

$$\begin{pmatrix} c \\ d \end{pmatrix} = \begin{pmatrix} \rho & -\tau \\ \tau & \rho \end{pmatrix} \begin{pmatrix} a \\ b \end{pmatrix} = \begin{pmatrix} \rho a - \tau b \\ \tau a + \rho b \end{pmatrix}. \quad (2.80)$$

2.5 Continuous-variable quantum computing

In this section, I will introduce some basic concepts of continuous-variable quantum computing (CVQC). The detailed discussion can be found in [22, 23, 24].

2.5.1 Measurement based quantum computing

There are two models for quantum computing (QC). The first one is circuit based QC [11], in which computation is performed by a sequence of quantum logical gates and measurements acting on initial input state. An example [11] is shown in Fig.2.5. State $|\Phi\rangle^+ = (|00\rangle + |11\rangle)/\sqrt{2}$ are input state of channel A and B, while $|\psi\rangle = \alpha|0\rangle + \beta|1\rangle$ is the input state of channel C. Those input states go through a sequence of gates (quantum operators) such as controlled X, Hadamard transform and measurements

to get the final results output state $|\psi\rangle_B$, which is a process to teleport state $|\psi\rangle$ from channel C to channel B.

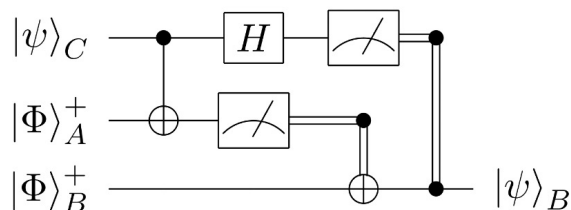


Figure 2.5: Circuit-based quantum computing example [11].

The second model is measurement-based quantum computing. It was proposed by Robert Raussendorf and Hans J. Briegel in 2001 [1]. Measurement-based QC is a method that first prepares an entangled resource state and then performs single qubit measurements on this state along with feedforward to neighboring qubits to process quantum information. It is also called one-way quantum computing because the resource state is partially destroyed by the measurements. The entangled resource state is usually a cluster state or a graph state, which is a highly entangled qubits lattice with all the initial quantum information embedded in it. Fig.2.6 shows an example of measuring qubit lattice cluster state [1]. Before the measurements, the qubits are in a square grid cluster state. Quantum information is processed by measuring each qubit in a certain order and basis. Different basis are represented by circles and arrows in Fig.2.6: circle \odot represents measuring spin Z of the qubit resulting removing the qubit from the state, vertical arrows are measurements of spin X and tilted arrows means measurements in the spin $x - y$ plane. Quantum information is propagated horizontally and the qubits on vertical connections are used to realize quantum gates.

A simpler example of quantum information teleportation through measurement on single qubit is shown in Fig.2.7. A simple two-qubit entangled state is created by

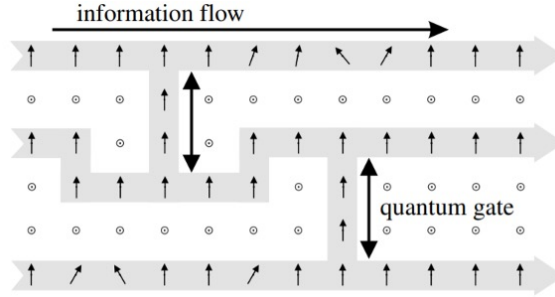


Figure 2.6: Quantum computing by measuring two-state qubit on lattice [1]. Circles \odot symbolize measurements of σ_z , vertical arrows are measurements of σ_x , while tilted arrows refer to measurements in the x-y plane.

applying C_Z gate to qubit 1: $|\varphi_{in}\rangle_1 = a|0\rangle_1 + b|1\rangle_1$ and qubit 2: $|+\rangle_2 = |0\rangle_2 + |1\rangle_2$. The state is a simple example of a cluster state

$$\begin{aligned} \mathbf{C_Z}(|\varphi_{in}\rangle_1 \otimes |+\rangle_2) = & |+\rangle_1 [(a + b)|0\rangle_2 + (a - b)|1\rangle_2] \\ & + |-\rangle_1 [(a - b)|0\rangle_2 + (a + b)|1\rangle_2]. \end{aligned} \tag{2.81}$$

If the result of measuring spin X of qubit 1 projects to $|+\rangle$, qubit 2 must have the output $(a + b)|0\rangle + (a - b)|1\rangle = a|+\rangle + b|-\rangle$. Therefore, the input information a and b is teleported to qubit 2. Note that the basis changed from 01 to +- . This can be fixed by an X Pauli gate, which is an example of “feedforward.”

$$|\varphi_{in}\rangle = a|0\rangle + b|1\rangle \quad \bullet \xrightarrow{\mathbf{C_Z}} \bullet \quad |+\rangle = |0\rangle + |1\rangle$$

Figure 2.7: Two-qubit state demonstrating the information teleportation.

2.5.2 Qubits and qumodes

In previous subsection, the basic unit used to perform QC is qubit. Qubit is a two-state quantum system, such as spin- $\frac{1}{2}$ particle with the two states being spin up and spin down, or the polarization of a photon the two states of which can be horizontal

polarization and vertical polarization. The two-state basis is discrete and denoted as $\{|0\rangle, |1\rangle\}$, which are the eigenstates of spin Z operator.

With the optical field quantization, the quantum optical field, also known as qumode, can be used as another basic unit of quantum computing [25]. The basis vectors of qumode are the eigenstates of amplitude quadrature Q , $\{|q\rangle\}_{q \in \mathbb{R}}$. Because q is continuous, the quantum computing based on qumodes is also named continuous variable quantum computing. Table 2.1 shows correspondences between the basis, states and operators of quantum computing using qubits and qumodes.

2.5.3 Cluster state

Cluster state is crucial to measurement-based quantum computing. It is the resource for all the embedded quantum information and processes. It is also proved that square grid cluster state is essential to realize universal quantum computing [1]. In this subsection, I will first summarize the definition and properties of qubit cluster state, and then I will introduce qumode cluster states using the corresponding relations given in Table 2.1.

Before showing the details of cluster state, I want to point out the difference between “graph state” and “cluster state”. A qubit graph state is a special type of multi-qubit state that can be represented by a graph. Each qubit is represented by a vertex of the graph, and the edges represent the entanglement between qubits. A graph state can have any graph but the term “cluster state” is usually reserved for graph states that are sparse enough to allow measurement-based quantum computing [26, 27, 28]. In the rest of this thesis, I use the “cluster state” only as the states we are discussing are sparse and adequate for one-way QC. I will also use the graph,

| | Qubit | Continuous variable |
|---|--|--|
| Basis | $\{ 0\rangle, 1\rangle\}$ $\langle n m\rangle = \delta_{n,m}, n, m \in \{0, 1\}$ | $\{ q\rangle_{q \in \mathbb{R}}\}$ $\langle q q'\rangle = \delta(q - q'), q, q' \in \mathbb{R}$ |
| Conjugate basis | Hadamard transformation $ \pm\rangle = \frac{1}{\sqrt{2}}(0\rangle \pm 1\rangle)$ | Fourier transformation $ p\rangle = \frac{1}{\sqrt{2\pi}} \int e^{ipq} q\rangle dq$ |
| Single-qubit/qumode state | $ \psi\rangle = \psi_0 0\rangle + \psi_1 1\rangle$ | $ \psi\rangle = \int \psi q\rangle dq$ |
| Single-qubit/qumode operators | Pauli group $\langle X, Z \rangle$ $X j\rangle = j \oplus 1\rangle, j = 0, 1$ $Z j\rangle = e^{ij\pi} j\rangle, j = 0, 1$ $X \pm\rangle = \pm \pm\rangle$ $Z \pm\rangle = \mp\rangle$ | Weyl–Heisenberg group $\langle \{X(\gamma)\}_{\gamma \in \mathbb{R}}, \{Z(\eta)\}_{\eta \in \mathbb{R}} \rangle$ $= \langle \{e^{-i\gamma P}\}_{\gamma \in \mathbb{R}}, \{e^{i\eta Q}\}_{\eta \in \mathbb{R}} \rangle$ $X(\gamma) q\rangle = q + \gamma\rangle$ $Z(\eta) q\rangle = e^{i\eta q} q\rangle$ $X(\gamma) p\rangle = e^{-i\gamma p} p\rangle$ $Z(\eta) p\rangle = p + \eta\rangle$ |
| Two-qubit/qumode operators (Controlled gates) | $C_X j\rangle_1 k\rangle_2 = j\rangle_1 k \oplus j\rangle_2$ $C_Z j\rangle_1 k\rangle_2 = e^{i\pi j k} j\rangle_1 k\rangle_2$ | $C_X q\rangle_1 q'\rangle_2 = e^{-i\epsilon Q_1 P_2} q\rangle_1 q'\rangle_2$ $= q\rangle_1 q' + \epsilon q\rangle_2$ $C_Z q\rangle_1 q'\rangle_2 = e^{i\epsilon Q_1 Q_2} q\rangle_1 q'\rangle_2$ $= e^{i\epsilon q q'} q\rangle_1 q'\rangle_2$ |
| Bipartite entanglement | Bell state (unnormalized) $ B_{00}\rangle_{12} = 00\rangle + 11\rangle$ $ B_{01}\rangle_{12} = X_1 B_{00}\rangle_{12}$ $= 10\rangle + 01\rangle$ $ B_{10}\rangle_{12} = Z_1 B_{00}\rangle_{12}$ $= 00\rangle - 11\rangle$ $ B_{11}\rangle_{12} = Z_1 X_1 B_{00}\rangle_{12}$ $= - 10\rangle + 01\rangle$ | EPR state (unnormalized) $ \text{EPR}(0, 0)\rangle_{12} = \int q\rangle_1 q\rangle_2 dq$ $ \text{EPR}(0, \gamma)\rangle_{12} = X_1(\gamma) \text{EPR}(0, 0)\rangle_{12}$ $= \int q + \gamma\rangle_1 q\rangle_2 dq$ $ \text{EPR}(\eta, 0)\rangle_{12} = Z_1(\eta) \text{EPR}(0, 0)\rangle_{12}$ $= \int e^{i\eta q} q\rangle_1 q\rangle_2 dq$ $ \text{EPR}(\eta, \gamma)\rangle_{12}$ $= Z_1(\eta)X_1(\gamma) \text{EPR}(0, 0)\rangle_{12}$ $= \int e^{i\eta(q+\gamma)} q + \gamma\rangle_1 q\rangle_2 dq$ |

Table 2.1: Correspondence between qubit and CV quantum information. \oplus is the exclusive or gate which yields true if and only if the two inputs are the same.

as defined above for graph state, to represent cluster state.

Qubit cluster state

A qubit cluster state is canonically defined the following way [2, 29]: prepare N qubits in the state $|+\rangle_j = (|0\rangle_j + |1\rangle_j)/\sqrt{2}$, denoted by graph vertices j , and apply controlled Z gates ($C_{Z_{ij}}$) between certain pairs of qubits to create entanglements which are the graph edges (j, k) connecting qubit vertices j and k .

The stabilizers \mathcal{S} of a cluster state $|\psi\rangle$ are the operators that leave the state unchanged:

$$\mathcal{S}|\psi\rangle = |\psi\rangle. \quad (2.82)$$

The stabilizers form a group of Pauli generators $X_j \otimes_{k \in \mathbf{N}_j} Z_k$, where $j=1, \dots, N$ denotes each graph vertex and \mathbf{N}_j is the neighborhood of j , i.e., the set of all vertices sharing an edge with j .



Figure 2.8: Two-qubit cluster state.

The simplest example is a two-qubit cluster state

$$C_{Z_{12}}|+\rangle_1|+\rangle_2 = \frac{1}{2}(|0\rangle_1|0\rangle_2 + |1\rangle_1|0\rangle_2 + |0\rangle_1|1\rangle_2 - |1\rangle_1|1\rangle_2). \quad (2.83)$$

The graph representation of this state is shown in Fig.2.8, with two vertices denoting two qubit $|+\rangle_1$ and $|+\rangle_2$ and edge connecting vertices representing C_Z gate. One

stabilizer of this state is $X_1 Z_2$ as

$$\begin{aligned} (X_1 Z_2) C_{Z_{12}} |+\rangle_1 |+\rangle_2 &= \frac{1}{2} [|1\rangle_1 |0\rangle_2 - |1\rangle_1 |1\rangle_2 + |0\rangle_1 |0\rangle_2 + |0\rangle_1 |1\rangle_2] \\ &= C_{Z_{12}} |+\rangle_1 |+\rangle_2. \end{aligned} \quad (2.84)$$

Continuous variable cluster state

Continuous variable (CV) cluster state are defined as the analogues of qubit cluster state [30, 23, 22]. For the ideal CV cluster state, it is generated by first preparing N zero-momentum eigenstates $|0\rangle_p^{\otimes N}$, and then applying controlled-Z operators $C_Z = \exp(igQ_j Q_k)$ to qumode j and k , where g is the strength of the interaction [31] indicated by the weight of the edge. Therefore, ideal CV cluster states can be described by weighted graphs with real value weights, while qubit graph states are described by unweighted graphs with edges (weighted 1) or without edges (weighted 0). We can define a symmetric adjacency matrix $\mathbf{A} = \mathbf{A}^T$ to mathematically represent the CV cluster state graph. The (j,k) element of the matrix $A_{j,k}$ is the weight of the edge connecting vertices j and k .

The ideal CV cluster state stabilizers are also the analogues of the stabilizers of qubit cluster state. From Table 2.1, using

$$X \rightarrow X(\gamma) = e^{-i\gamma P}, \quad (2.85)$$

$$Z \rightarrow Z(\eta) = e^{i\eta Q}, \quad (2.86)$$

the CV cluster state stabilizers are the generators of the Weyl-Heisenberg displacement group

$$e^{-i\gamma P_j} \bigotimes_{k \in \mathbf{N}_j} e^{i\eta Q_k} = \exp \left\{ -i\gamma_j \left[P_j - \sum_{k \in \mathbf{N}_j} \frac{\eta_k}{\gamma_j} Q_k \right] \right\}. \quad (2.87)$$

It is easy to see that if the exponent part of the stabilizer $\mathcal{N} = 0$, the definition of a stabilizer Eq. (2.82) is satisfied. This exponent part \mathcal{N} leads to the equivalent definition of operators that multiply the state $|\psi_A\rangle$ by 0, as known as nullifiers,

$$\mathcal{N}|\psi_A\rangle = (\mathbf{P} - \mathbf{A}\mathbf{Q})|\psi_A\rangle = 0, \quad (2.88)$$

where $\mathbf{P} = (P_1, P_2, \dots, P_N)^T$ and $\mathbf{Q} = (Q_1, Q_2, \dots, Q_N)^T$ are the column vector of momentum and position operators.

The ideal CV cluster state we discussed so far are unphysical, because a zero-momentum eigenstate requires the uncertainty of momentum quadrature P vanish, which will only happen with infinite squeezing, i.e. $r \rightarrow \infty$. Therefore, what is used in reality is approximate CV cluster state, which belong to Gaussian pure states [31]. The nullifiers of the approximate CV cluster states are measured close to 0. It has been proved that fault-tolerant QC is theoretically possible for finitely squeezed Gaussian states with non-Gaussian resources [15, 16]. A more detailed discussion about approximate CV cluster states graphical calculations will be shown in Chapter 3.

Chapter 3

Hypercubic cluster states generated by the phase modulated quantum optical frequency comb

Cluster states are a crucial resource for measurement-based quantum computing (QC) [1, 18]. Quantum optics provides a scalable platform for continuous-variable (CV) universal QC, based on qumodes (e.g. quantum optical fields) cluster states [22, 32, 18, 33, 34]. The interference of shifted, two-mode-squeezed quantum optical frequency combs (QOFCs), emitted by optical parametric oscillators (OPOs), has been shown to generate cluster states [2, 30] in the spectral domain [35, 3, 36] and in the temporal domain [37, 38, 4, 5], with thousands to millions of entangled qumodes. Spatial interference of QOFCs to generate cluster states also have been accomplished [6] or proposed [39, 40]. Hybrid time-frequency schemes were proposed as well [7]. It is important to note that CVQC can be made fault tolerant at reachable squeezing levels [15, 16, 17]. The aforementioned work in the temporal and spectral domains relied on interfering two to four straddling squeezed QOFC, as originally proposed in Refs. [41] and [42].

Our work shows that a single comb with phase modulation is in fact sufficient to generate n -hypercubic cluster states of arbitrary dimension n . The dimension of

the cluster graph is determined by the number of modulation frequencies and its size is determined by their spacing. Such states are universal resources for quantum computing for $n = 2$ [1]. For $n = 3$, they can also allow quantum error correction topological encoding [19]. This work was published in [43].

This discovery was made possible by a general analysis of the generated Gaussian graph state, factoring in concrete experimental parameters such as finite squeezing, pump amplitude, and modulation depth [44]. Our results account for all graph errors and allow us to drastically simplify experimental configurations, paving the way to compact realizations of large-scale cluster entanglement using a single OPO on chip [45, 46, 47, 48, 49].

In this chapter, I will first review the symplectic representation of Gaussian states and the graphical calculus for CV cluster states. Then I will recall the quantum description of phase modulation and theoretically n -hypercubic cluster states, with the graph errors and full effects of finite squeezing are thoroughly analyzed.

3.1 Gaussian state evolution

Gaussian states are the states that have Wigner functions in the form of Gaussian function. The Wigner function was first introduced by Eugene Wigner in 1932 [50] to describe a quantum state using the quasiprobability distribution in phase space. For a quantum state that has density operator $\rho = \sum_j p_j |\psi_j\rangle\langle\psi_j|$, where $|\psi_j\rangle$ is a pure

state vector prepared with probability p_j , the Wigner function is

$$W(q, p) = \frac{1}{\pi} \int_{-\infty}^{\infty} e^{2ipy} \langle q - y | \rho | q + y \rangle dy, \quad (3.1)$$

where q and p are the eigenvalues of amplitude and phase quadratures.

Gaussian states can be completely determined by first (expectation values) and second (covariance matrix) momentum of quadrature operators. A column vector consists of amplitude and phase quadratures is defined as

$$\mathbf{x} = (\mathbf{Q}, \mathbf{P})^T, \quad (3.2)$$

where $\mathbf{Q} = (Q_1, \dots, Q_N)^T$ and $\mathbf{P} = (P_1, \dots, P_N)^T$. The covariance matrix σ will be discussed later in Subsection 3.1.2. Here I will only give the expression of Wigner function of a Gaussian

$$W(\mathbf{x}) = \frac{1}{2\pi \sqrt{\det(\sigma)}} e^{-\frac{1}{2}(\mathbf{x} - \langle \mathbf{x} \rangle) \sigma^{-1} (\mathbf{x} - \langle \mathbf{x} \rangle)^T}, \quad (3.3)$$

where $\langle \mathbf{x} \rangle$ is the expectation value of \mathbf{x} .

Gaussian operators are those that transform Gaussian states to Gaussian states. The Gaussian states examples include vacuum state, coherent state, squeezed state, etc. The Gaussian operators include displacement, phase rotation, squeezing, beam splitter etc. Some good references to the Gaussian states are [51, 52]. In the following part of this chapter, only Gaussian pure states will be discussed and the detailed derivation can be found in [31].

3.1.1 Symplectic representation of Gaussian unitary transformation

For a N -mode state, in the Heisenberg picture, the action of an unitary operation U makes the quadrature operators evolve as

$$\begin{aligned} Q'_j &= U^\dagger Q_j U, \\ P'_j &= U^\dagger P_j U, \end{aligned} \tag{3.4}$$

where Q_j and P_j are the quadratures of the state before the action and Q'_j and P'_j are the quadratures after the action. In terms of the vector \mathbf{x} as defined in Eq. (3.2), for Gaussian pure state, this evolution can be expressed with a symplectic matrix as

$$x'_j = U^\dagger x_j U = \sum_{k=1}^{2N} S_{jk} x_k, \tag{3.5}$$

where S_{jk} are complex numbers and the elements of a $2N \times 2N$ matrix, which is called symplectic matrix \mathbf{S} . Therefore, the evolution of vector \mathbf{x} is

$$\mathbf{x}' = \mathbf{S}\mathbf{x}. \tag{3.6}$$

The symplectic matrix \mathbf{S} and the Gaussian unitary operator U are one-to-one correspondent. There is a unique \mathbf{S} for every U and there is a unique U for every \mathbf{S} .

According to the mathematical definition of symplectic matrix

$$\mathbf{S}^T \Omega \mathbf{S} = \Omega, \tag{3.7}$$

where \mathbf{S}^T is the transpose of \mathbf{S} and Ω is a nonsingular ($\Omega^{-1}\Omega = I$), skew-symmetric

matrix ($\Omega^T = -\Omega$), explicitly $\Omega = \begin{pmatrix} \mathbf{0} & \mathbf{1} \\ -\mathbf{1} & \mathbf{0} \end{pmatrix}$, where $\mathbf{0}$ is a zero submatrix and $\mathbf{1}$ is an identity submatrix. Next I will show that this symplectic nature of \mathbf{S} is guaranteed.

The canonical multimode commutators $[Q_j, P_k] = i\mathbf{I}\delta_{jk}$ can be rewritten as

$$[\mathbf{x}, \mathbf{x}^T] = i \begin{pmatrix} \mathbf{0} & \mathbf{I} \\ -\mathbf{I} & \mathbf{0} \end{pmatrix} = i\Omega, \quad (3.8)$$

where \mathbf{I} is the identity matrix and the commutator of two vectors is defined as

$$[\mathbf{r}, \mathbf{s}^T] = \mathbf{r}\mathbf{s}^T - (\mathbf{s}\mathbf{r}^T)^T, \quad (3.9)$$

which isn't necessarily zero because the elements of vectors \mathbf{r} and \mathbf{s} are operators. The transpose operator T only changes the index of the vector elements, for example $(\mathbf{s}^T)_{jk} = \mathbf{s}_{kj}$. The transpose operator will not act on each operator element itself, i.e. each operator will not be transposed. This makes $[\mathbf{r}, \mathbf{s}^T]$ not necessarily be 0. Using the condition that the quadrature commutation relation is unchanged under the Gaussian operators, Ω satisfies

$$i\Omega = [\mathbf{x}', \mathbf{x}'^T] = [\mathbf{S}\mathbf{x}, (\mathbf{S}\mathbf{x})^T] = \mathbf{S}[\mathbf{x}, \mathbf{x}^T]\mathbf{S}^T = i\mathbf{S}\Omega\mathbf{S}^T. \quad (3.10)$$

Therefore it is proved that the matrix \mathbf{S} is a symplectic matrix satisfying $\mathbf{S}\Omega\mathbf{S}^T = \Omega$.

A sequence of transformations

When a quantum state evolves under a sequence of unitary operations in order of $U_1, U_2, U_3 \dots U_n$, the quadrature operators change in Heisenberg picture

$$x'_j = U_1^\dagger U_2^\dagger \dots U_n^\dagger x_j U_n \dots U_2 U_1. \quad (3.11)$$

Using Eq. (3.5),

$$\begin{aligned} x'_j &= U_1^\dagger U_2^\dagger \dots U_{n-1}^\dagger \left(\sum_{k=1}^{2N} S_{njk} x_k \right) U_{n-1}^\dagger \dots U_2 U_1 \\ &= \sum_{k=1}^{2N} S_{njk} (U_1^\dagger U_2^\dagger \dots U_{n-1}^\dagger x_k U_{n-1}^\dagger \dots U_2 U_1) \\ &= \sum_{k=1}^{2N} S_{njk} (U_1^\dagger U_2^\dagger \dots U_{n-2}^\dagger \left(\sum_{l=1}^{2N} S_{n-1kl} x_l \right) U_{n-2} \dots U_2 U_1) \\ &= \sum_{k,l} S_{njk} S_{n-1kl} (U_1^\dagger U_2^\dagger \dots U_{n-2}^\dagger x_l U_{n-2} \dots U_2 U_1). \end{aligned} \quad (3.12)$$

Continuing the matrix element substitutions, we see that applying the unitary operator in an order of $U_n, U_{n-1} \dots U_1$ to the quadrature operator yields an expression in terms of symplectic matrix $\mathbf{S}_1, \mathbf{S}_2, \dots \mathbf{S}_n$ as

$$\mathbf{x}' = \mathbf{S}_n \mathbf{S}_{n-1} \dots \mathbf{S}_1 \mathbf{x} = \mathbf{S} \mathbf{x}. \quad (3.13)$$

Different from the order of the Heisenberg-picture unitary operators, the symplectic matrix ordering is that of the Schrödinger picture.

3.1.2 Symplectic representation of Gaussian pure state

Covariance matrix

A Gaussian pure state is uniquely represented by its covariance matrix. Covariance matrix is defined as

$$(\text{Cov } \mathbf{x})_{jk} = \text{Cov}[x_j, x_k] = \langle (x_j - \langle x_j \rangle) (x_k - \langle x_k \rangle) \rangle. \quad (3.14)$$

When the expectation $\langle x_j \rangle = 0$, the covariance matrix is simplified to [31]

$$\text{Cov } \mathbf{x} = \frac{1}{2} \langle \{ \mathbf{x}^\dagger, \mathbf{x}^T \} \rangle, \quad (3.15)$$

where the anticommutator product is defined as

$$\{ \mathbf{x}, \mathbf{y}^T \} = \mathbf{x} \mathbf{y}^T + (\mathbf{y} \mathbf{x}^T)^T. \quad (3.16)$$

This anticommutator is required to symmetrize all products of operators which do not commute. For example, the terms $Q_j P_j$ and $P_j Q_j$ do not commute, and they will be replaced by a symmetrized term $\frac{1}{2}(Q_j P_j + P_j Q_j)$. With the fact that any N-mode Gaussian pure state can be generated from ground state of N harmonic oscillator by applying Gaussian unitary operations, the corresponding quadrature vector \mathbf{x} can be expressed in terms of a total symplectic matrix \mathbf{S}

$$\mathbf{x} = \mathbf{S} \mathbf{x}_0, \quad (3.17)$$

where x_0 is the quadrature vector of ground state (vacuum). The covariance matrix of a vacuum state is

$$\text{Cov } \mathbf{x}_0 = \frac{1}{2}\mathbf{I}. \quad (3.18)$$

Therefore, the covariance matrix of a state which has the quadrature vector \mathbf{x} is

$$\begin{aligned} \text{Cov } \mathbf{x} &= \text{Cov } (\mathbf{S}\mathbf{x}_0) \\ &= \frac{1}{2} \left\langle \left\{ \mathbf{S}\mathbf{x}_0^\dagger, \mathbf{S}\mathbf{x}_0^T \right\} \right\rangle \\ &= \frac{1}{2} \mathbf{S} \left\langle \left\{ \mathbf{x}_0^\dagger, \mathbf{x}_0^T \right\} \right\rangle \mathbf{S}^T \\ &= \mathbf{S}(\text{Cov } \mathbf{x}_0)\mathbf{S}^T \\ &= \frac{1}{2}\mathbf{S}\mathbf{S}^T. \end{aligned} \quad (3.19)$$

Z matrix representation

Any symplectic matrix \mathbf{S} can be decomposed as [31]

$$\mathbf{S} = \begin{pmatrix} \mathbf{I} & \mathbf{0} \\ \mathbf{V} & \mathbf{I} \end{pmatrix} \begin{pmatrix} \mathbf{U}^{-1/2} & \mathbf{0} \\ \mathbf{0} & \mathbf{U}^{1/2} \end{pmatrix} \begin{pmatrix} \mathbf{X} & -\mathbf{Y} \\ \mathbf{Y} & \mathbf{X} \end{pmatrix}. \quad (3.20)$$

where \mathbf{U} and \mathbf{V} are $N \times N$ symmetric matrices. \mathbf{U} is also positive definite ($\mathbf{U} = \mathbf{U}^T > 0$). The third matrix is orthogonal and in optical setting, it corresponds to beamsplitters and phase shifter shown in Section 2.4, which has no effect on vacuum state. Therefore, the third matrix does not affect the state that can be generated from the ground state. For simplicity, it can be set that $\mathbf{X} = \mathbf{I}$ and $\mathbf{Y} = \mathbf{0}$. The

symplectic matrix \mathbf{S} then becomes [53]

$$\mathbf{S} = \begin{pmatrix} \mathbf{U}^{-1/2} & \mathbf{0} \\ \mathbf{V}\mathbf{U}^{-1/2} & \mathbf{U}^{1/2} \end{pmatrix}. \quad (3.21)$$

The covariance matrix can be expressed in terms of \mathbf{U} and \mathbf{V} matrices

$$\text{Cov}\mathbf{x} = \frac{1}{2}\mathbf{S}\mathbf{S}^T = \frac{1}{2} \begin{pmatrix} \mathbf{U}^{-1} & \mathbf{U}^{-1}\mathbf{V} \\ \mathbf{V}\mathbf{U}^{-1} & \mathbf{U} + \mathbf{V}\mathbf{U}^{-1}\mathbf{V} \end{pmatrix}. \quad (3.22)$$

With the expression of covariance matrix, we can write the Wigner function and further get the position-space wave function of a N-mode pure state as [31]

$$\psi(\mathbf{q}) = \pi^{-\frac{N}{4}} (|\mathbf{U}|^{\frac{1}{4}}) \exp \left[-\frac{1}{2} \mathbf{q}^T (\mathbf{U} - i\mathbf{V}) \mathbf{q} \right]. \quad (3.23)$$

Form the equation above, it is possible to specify a Gaussian pure state only using \mathbf{V} and \mathbf{U} . We define a complex matrix \mathbf{Z} :

$$\mathbf{Z} = \mathbf{V} + i\mathbf{U} \quad (3.24)$$

to describe the state. This \mathbf{Z} matrix is a complex-weighted adjacency matrix to an undirected graph, which gives the graph representation for a Gaussian pure state. \mathbf{V} is the exact analog to the adjacency matrix of a qubit graph state (see subsection 2.5.3) [22] and \mathbf{U} is the error matrix, which is used to analyze the error of graph state with finite squeezing approximations compared to an ideal continuous variable cluster state. The error analysis details will be addressed in the next part.

The evolution of an initial state \mathbf{Z} to a final state \mathbf{Z}' under a symplectic transfor-

mation of matrix \mathbf{S} given by

$$\mathbf{S} = \begin{pmatrix} \mathbf{A} & \mathbf{B} \\ \mathbf{C} & \mathbf{D} \end{pmatrix}, \quad (3.25)$$

where \mathbf{A} , \mathbf{B} , \mathbf{C} and \mathbf{D} are $N \times N$ block matrices, is calculated using Möbius transformation [53]

$$\mathbf{Z}' = (\mathbf{C} + \mathbf{DZ})(\mathbf{A} + \mathbf{BZ})^{-1}. \quad (3.26)$$

Nullifier formalism

From previous Section 2.5.3, the ideal CV cluster state can be defined by its nullifying operators, or nullifiers [31], as shown in $(\mathbf{P} - \mathbf{A}\mathbf{Q})|\psi\rangle = \mathbf{0}|\psi\rangle$, which are the logarithms of the stabilizers of $|\psi\rangle$. The matrix \mathbf{A} is the adjacency matrix of the graph state with infinite squeezing. For a finite squeezed graph state, the adjacency matrix \mathbf{Z} satisfies $\lim_{r \rightarrow \infty} \mathbf{Z}_r = \mathbf{A}$ and the nullifiers are

$$(\mathbf{P} - \mathbf{Z}\mathbf{Q})|\psi\rangle = \mathbf{0}|\psi\rangle. \quad (3.27)$$

Note that the nullifier operators $\mathbf{P} - \mathbf{Z}\mathbf{Q}$ are the generators of an additive mathematical group: any linear combination of nullifiers is a nullifier. For example, multiplying a complex number matrix \mathbf{M} to the left of the nullifier can create a new nullifier for the same state

$$\mathbf{M}(\mathbf{P} - \mathbf{Z}\mathbf{Q})|\psi\rangle = \mathbf{0}|\psi\rangle. \quad (3.28)$$

The covariance matrix of the nullifiers is [31]

$$\text{Cov} [\mathbf{P} - \mathbf{Z}\mathbf{Q}] = \mathbf{U}. \quad (3.29)$$

If only calculate the covariance matrix of the real part of the \mathbf{Z} matrix

$$\text{Cov} [\mathbf{P} - \mathbf{V}\mathbf{Q}] = \begin{pmatrix} -\mathbf{V} & \mathbf{I} \end{pmatrix} (\text{Cov } \mathbf{x}) \begin{pmatrix} -\mathbf{V} \\ \mathbf{I} \end{pmatrix} = \frac{1}{2}\mathbf{U}. \quad (3.30)$$

Because \mathbf{Z} is complex in general, these nullifiers are non-Hermitian and cannot be measured, which makes measurement-based quantum computing problematic since it requires a measurable graph [23]. Thus, only Gaussian states with \mathbf{Z} real, i.e. with $\mathbf{Z}=\mathbf{V}$ and $\mathbf{U}=\mathbf{0}$, are proper cluster states.

In summary, \mathbf{Z} matrix of an approximate cluster state provide the information that \mathbf{V} is the graph of the ideal CV cluster state and \mathbf{U} shows the error of the approximated cluster state compared to the ideal cluster state.

3.2 Finite squeezing and graph errors

We deduce from Eq. 3.30 that an arbitrary Gaussian state of matrix \mathbf{Z} can be considered as a cluster state of matrix \mathbf{V} if and only if:

(i), the error matrix \mathbf{U} is diagonal [44] and,

(ii), it verifies $\text{Tr}[\mathbf{U}] \rightarrow 0$ in the limit of infinite squeezing [31].

In that case, the components of $\mathbf{P} - \mathbf{V}\mathbf{Q}$ are *squeezed*, uncorrelated Hermitian operators. Proper examination of \mathbf{U} in light of requirements (i,ii) is crucial and will be presented in this section.

While requirement (ii) has been systematically fulfilled in all previous realizations

of CV cluster states [54, 35, 3, 38, 4, 5], requirement (i) had not been considered until very recently [44], largely because all previous experimental realizations of cluster states had, in theory, a diagonal \mathbf{U} (in practice, they might not have). From Eq. 3.30, an off-diagonal element of \mathbf{U} has the general physical meaning of a correlation between two cluster-state nullifiers. Such covariances must be zero in order for the cluster state to be adequate for one-way quantum computing. In this section, we evaluate the contribution of off-diagonal elements of \mathbf{U} and determine the precise conditions under which they can be neglected, which amounts to relaxing requirement (i) to

(i'), the error matrix \mathbf{U} is diagonally dominant.

Before we deal with error matrix \mathbf{U} , we first assume it fulfills both (i) and (ii) and focus on the effect of the weak, undesirable edges in \mathbf{V} that can be seen in Fig.3.7 but not in Fig.3.11.

3.2.1 Effect of a spurious graph edge: bipartite case

We first take the simplest example of a canonical cluster state: single mode squeezed state. It is obtained by applying the squeezed operator S_1 to a single qumode 1. In the realistic case of finite squeezing with squeezing parameter r_1 , the exact nullifier of this single-mode phase-squeezed (SMS) state is

$$\mathcal{N}_{s1} = S_1(r_1) a_1 S_1^\dagger(r_1) = P_1 - ie^{-2r_1} Q_1. \quad (3.31)$$

Two phase-squeezed qumodes coupled by gate $C_Z = \exp(i\varepsilon Q_1 Q_2)$ form a Gaussian cluster state that has the nullifiers

$$\mathcal{N}_1 = C_Z \mathcal{N}_{s1} C_Z^\dagger = P_1 - ie^{-2r_1} Q_1 - \varepsilon Q_2 \quad (3.32)$$

$$\mathcal{N}_2 = C_Z \mathcal{N}_{s2} C_Z^\dagger = P_2 - ie^{-2r_2} Q_2 - \varepsilon Q_1, \quad (3.33)$$

From the nullifier expression Eq. 3.27, the \mathbf{Z} matrix of this state is

$$\mathbf{Z} = \begin{pmatrix} ie^{-2r_1} & \varepsilon \\ \varepsilon & ie^{-2r_2} \end{pmatrix}, \quad (3.34)$$

$$\mathbf{V} = \begin{pmatrix} 0 & \varepsilon \\ \varepsilon & 0 \end{pmatrix}, \quad (3.35)$$

$$\mathbf{U} = \begin{pmatrix} ie^{-2r_1} & 0 \\ 0 & ie^{-2r_2} \end{pmatrix}. \quad (3.36)$$

$$(3.37)$$

The adjacency graph of \mathbf{V} matrix is shown in Fig. 3.1. It is a two mode state with edge weighted ε . The \mathbf{U} is diagonal and vanishes with increasing squeezing.

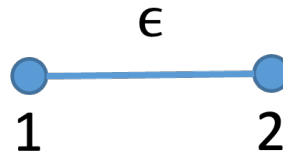


Figure 3.1: Two qumodes connected by a C_Z gate with weak interaction strength ε .

We now ask the following question: if we wrongly assumed qumode 1 to be isolated, however in fact linked to qumode 2 by a graph edge of small weight ε , how

large could ε be before its effects are detectable?

To answer this question, we must first relate it to the actual physical measurements we can make on qumode 1.

Measurement noise induced by a spurious graph edge

Under the assumption that we have two single-mode phase-squeezed states, the lowest measurement noise should be obtained by measuring the phase quadrature operator P_1 , typically by homodyne detection. In the case of a phase-squeezed qumode 1, observable P_1 has squeezed noise given by

$$(\Delta P_1)^2 = {}_1\langle 0 | S_1(r_1)^\dagger P_1^2 S_1(r_1) | 0 \rangle_1 = \frac{1}{2} e^{-2r_1}. \quad (3.38)$$

We now assume P_1 when qumode 1 also has a C_Z graph edge of weight ε with qumode 2 (squeezed by r_2), then we have

$$(\Delta P_1)^2 = {}_{12}\langle 00 | S_2^\dagger S_1^\dagger C_Z^\dagger P_1^2 C_Z S_1 S_2 | 00 \rangle_{12} \quad (3.39)$$

$$= {}_{12}\langle 00 | (P_1 e^{-2r_1} - \varepsilon Q_2 e^{2r_2})^2 | 00 \rangle_{12} \quad (3.40)$$

$$= \frac{1}{2} e^{-2r_1} [1 + \varepsilon^2 e^{2(r_1+r_2)}]. \quad (3.41)$$

Comparing Eqs. (3.38) & (3.41), we deduce the condition for neglecting a graph edge of weight ε :

$$\varepsilon^2 e^{2(r_1+r_2)} \ll 1, \quad (3.42)$$

which can be further clarified as

$$\varepsilon \ll \varepsilon_{\min} = e^{-(r_1+r_2)}, \quad (3.43)$$

where ε_{\min} is the edge weight at which the quantum noise is raised by 3 dB on a single qumode quadrature measurement.

We now connect this reasoning to the formalism of Gaussian graphical calculus [31] and, in particular, Eq. 3.30. The procedure is the following: we define a “trimmed” version of the original graph $\mathbf{Z}' = \mathbf{V}' + \mathbf{iU}'$. The \mathbf{V}' is obtained by zeroing all entries $\mathbf{V}_{jk} \ll \varepsilon_{\min}$. In this case, it yields $\mathbf{V}' = \mathbf{O}$ and a diagonal error matrix

$$\mathbf{U}' = 2 \operatorname{cov}[\mathbf{P} - \mathbf{V}'\mathbf{Q}] \quad (3.44)$$

$$= 2 \operatorname{cov}[\mathbf{P}] \quad (3.45)$$

$$= \begin{pmatrix} e^{-2r_1} [1 + \varepsilon^2 e^{2(r_1+r_2)}] & 0 \\ 0 & e^{-2r_2} [1 + \varepsilon^2 e^{2(r_1+r_2)}] \end{pmatrix} \quad (3.46)$$

with the general condition for each diagonal term in \mathbf{U}' satisfying $U'_{jj} \rightarrow 0$

$$\varepsilon \ll e^{-(r_1+r_2)}, \quad (3.47)$$

identical to Eq. (3.43).

Effect of spurious edges on the cluster state and on quantum computing

Using the Gaussian CV version [23] of the Heisenberg picture evolution under Clifford gates [55], it is straightforward to compute the evolution of the cluster state initially defined by Eqs. (3.32) & (3.33) after the measurement of P_1 : the new nullifiers are

$$\mathcal{N}'_1 = P_1 - \varpi_1 \mathbb{1}_1 \quad (3.48)$$

$$\mathcal{N}'_2 = P_2 - i[(e^{-2r_2} + \varepsilon^2 e^{2r_1}) Q_2 - \varepsilon e^{2r_1} \varpi_1], \quad (3.49)$$

where ϖ_1 is the measurement result (which is corrected by feedforward in one-way quantum computing). From Eq. (3.49), the effect of the spurious graph edge is twofold:

- a decrease of the squeezing of qumode 2 (ε^2 term), and
- an amplitude displacement of qumode 2 (ε term).

Both these effects are actually negligible under the exact same condition given by Eqs. (3.43) & (3.47). This is obvious for the ε^2 term. For the ε term, one need only notice that $\varpi_1 \sim e^{-r_1}$ for a squeezed qumode and that the resulting displacement of qumode 2 should be much smaller than the squeezing to be unnoticeable, i.e., $\varepsilon e^{r_1} \ll e^{-r_2}$, which is equivalent to Eq. (3.43).

The exact same analysis can be conducted in the case of a spurious imaginary (instead of real) graph edge, i.e., a residual off-diagonal element of \mathbf{U} (instead of \mathbf{V}).

To model that case, we just have to do $\varepsilon \mapsto i\varepsilon$ in the nullifiers in Eqs. (3.32) & (3.33) and in Eq. (3.49), which gives

$$\mathcal{N}_1'' = P_1 - \varpi_1 \mathbb{1}_1 \quad (3.50)$$

$$\mathcal{N}_2'' = P_2 - \varepsilon e^{2r_1} \varpi_1 - i(e^{-2r_2} - \varepsilon^2 e^{2r_1}) Q_2, \quad (3.51)$$

with the same type of effects as before (the displacement here being a phase one) and the same condition of Eq. (3.43) for them to be negligible.

Unsurprisingly, spurious edges lead to the aforementioned general Gaussian noise effects on the partner vertex after measurement of one vertex. One can also expect these effects to compound, measurement after measurement, when several spurious edges are present. However, this is not a concern because this type of effect is already known to affect Gaussian quantum computing, as finite squeezing imposes an expo-

ponential decrease of the distance along which quantum information can be propagated by quantum measurements down a linear cluster state [56]. Note that this happens for \mathbf{U} matrices that perfectly fulfill both requirements (i, ii) , and is the reason for the necessity of non-Gaussian resources (such as GKP states or PNR measurements) to achieve universal quantum computing and fault tolerance [15].

Back to our case, we will now show that all detrimental effects of all spurious edges in our cluster states can always be engineered to be at least one order of magnitude smaller than the aforementioned effect of finite squeezing. This means that the imperfections of our cluster state, which verifies requirements (i', ii) , cannot be an obstacle to reaching fault tolerance.

3.2.2 Effect of spurious graph edges: multipartite case

For the multipartite case, it is hard to evaluate how the measurement noise of each qumode changes with neglecting the spurious graph edges connected to it, as previously shown in the two-mode case. Instead, based on the properties of \mathbf{U} , we can derive a good quantitative estimate of the level at which spurious edges can be neglected, for a given squeezing level ($\text{Tr}[\mathbf{U}]$).

We define an error vector $\mathbf{\Gamma}$:

$$\Gamma_j = \frac{1}{\mathbf{U}_{jj}} \sum_{k \neq j} |\mathbf{U}_{jk}|. \quad (3.52)$$

Assuming \mathbf{U}_{jj} is of the order of a squeezing factor e^{-2r_j} (see Fig.3.8), which ensures

(ii), then (i) can be fulfilled if each and every qumode j satisfies

$$\Gamma_j \ll 1. \tag{3.53}$$

The meaning of Eq. (3.53) is straightforward but very important: the sum of the magnitudes of all spurious edge weights is much smaller than the \mathbf{U} diagonals, which is squeezing factor, i.e., the combined effect of all spurious edges is essentially buried in the squeezed noise.

This can even be relaxed a bit if one remember that local imperfections in cluster states can be measured out: if a majority of qumodes verify Eq. (3.53), then the few of them that don't can be taken out of the graph by measuring Q_j [30, 23].

The procedure of Eq. (3.44) can be straightforwardly applied to the multipartite case: after zeroing out weak edges in \mathbf{V} , we seek to diagonalize \mathbf{U} by applying local unitary operators, here Fourier transforms, and inspect the final \mathbf{U}' . If diagonalization wasn't successful (it's not always possible [44]), we evaluate $\mathbf{\Gamma}$ to assess the closeness of the state to a perfect cluster state.

3.3 Phase modulation

Phase modulation (PM) is using a modulation signal to change the phase angle of a carrier signal. A common device that applies phase modulation to optical field is an electro-optical modulator (EOM). A monochromatic carrier field of frequency ω_o and amplitude A enters the EOM, the field of which is $Ae^{i\omega_o t}$. A sinusoidally varying voltage served as modulation signal is applied to the EOM with frequency Ω and

amplitude m . It changed the refraction index of EOM crystal thus adding a time dependent phase term to the carrier field. This phase modulated field can be written as sum of harmonic sidebands at frequencies $\omega_n = \omega_o + n\Omega$ ($n \in \mathbb{Z}$) and of amplitudes the Bessel functions of the first kind

$$Ae^{i[\omega_o t + m \sin(\Omega t + \phi)]} = Ae^{i\omega_o t} \sum_{n=-\infty}^{\infty} J_n(m) e^{in(\Omega t + \phi)}, \quad (3.54)$$

where m is the modulation index and ϕ the PM phase. In the small modulation index limit, we have the approximation that only carrier ($n = 0$) and first order sidebands ($n = \pm 1$) remain

$$Ae^{i[\omega_o t + m \sin(\Omega t + \phi)]} \approx A \left(e^{i\omega_o t} + \frac{m}{2} e^{i(\omega_+)t + i\phi} - \frac{m}{2} e^{i(\omega_-)t - i\phi} \right), \quad (3.55)$$

where the sidebands frequency $\omega_{\pm} = \omega_0 \pm \Omega$.

From the optical fields perspective, the process of this phase modulation is modeled by a nonlinear interaction between two optical fields a_j and $a_{j+\Omega}$, at two frequencies differing by the the modulation frequency $\Omega \in \mathbb{N}$, and the radio frequency field $a_R = \alpha e^{-i\phi}$, $\alpha \geq 0$, at the modulation frequency, which is assumed classical and unchanged (neither depleted not amplified). Under these conditions, it is straightforward to show that the effective Hamiltonian of this interaction has a beamsplitter form [57]

$$H = \hbar \frac{\alpha}{\tau} e^{-i\phi} \sum_{j=-\infty}^{\infty} a_j a_{j+\Omega}^{\dagger} + \text{H.c.}, \quad (3.56)$$

where $\alpha = m/2$, τ is the interaction time in the phase modulator, and a_j is the annihilation operator of the qumode of frequency j in units of the qumode spacing, i.e., of the free spectral range (FSR) of the optical parametric oscillator (OPO), which

will be introduced in Section 4.1. Note that the interaction time τ is introduced in Eq. (3.56) in order to make the results of Heisenberg equations be in terms of modulation depth m as shown later in Eq. (3.59), which means τ is included in m in the final solution. We take Ω in units of the FSR from Eq. (3.56) on, which means Ω is an integer number of FSRs. Therefore, phase modulation can be modeled as a frequency-domain, generalized beamsplitter [57], as illustrated in Fig.3.2.

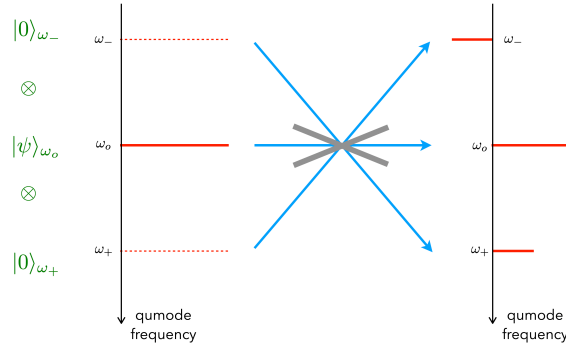


Figure 3.2: Quantum model of phase modulation at frequency Ω by a 3×3 frequency-domain beamsplitter, Eq.3.56 [57], symbolized by the unphysical gray element that features two frequency-domain “reflective,” and one “transmissive,” possibilities for each input beam (blue lines) at $\omega_{\pm} = \omega_o \pm \Omega$. For simplicity, we didn’t draw modulation sidebands of order greater than 1. An arbitrary input state is given in green, containing 3 qumodes (red lines) indexed by their frequency. A key point is that the carrier qumode at ω_o is coupled by PM to the input vacuum modes. When $|\psi\rangle$ is a coherent state, the output remains a product of coherent states.

This yields the Heisenberg equations as

$$\frac{da_j}{dt} = -i\frac{\alpha}{\tau} (e^{-i\phi} a_{j-\Omega} + e^{i\phi} a_{j+\Omega}), \quad (3.57)$$

the solution of which is

$$\begin{pmatrix} a'_1 \\ a'_2 \\ \vdots \\ a'_N \end{pmatrix} = \mathbf{M} \begin{pmatrix} a_1 \\ a_2 \\ \vdots \\ a_N \end{pmatrix}, \quad (3.58)$$

derived by diagonalizing Töplitz matrices, as is clear from Eq. (3.57) for $\Omega = 1$. This still applies for $\Omega > 1$ because the matrix of the equation system Eq. (3.57) can always be block-diagonalized into Töplitz blocks. Using the eigenvalues and eigenvectors of Töplitz matrices [58], we find, for $\Omega = 1$, the elements of \mathbf{M} are

$$M_{jk} = \frac{2}{N+1} \sum_{m=1}^N i^{j-k} \sin \frac{j m \pi}{N+1} \sin \frac{k m \pi}{N+1} \exp \left(i 2 \alpha \cos \frac{m \pi}{N+1} \right) \quad (3.59)$$

$$= J_{k-j}(2\alpha) - (-1)^j J_{k+j}(2\alpha), \quad (3.60)$$

for $\phi = \pi/2$ in Eq. (3.57), where $J_{k \pm j}(2\alpha)$ are the Bessel functions of the first kind, which describe the phase modulation spectrum generated from a single initial mode in a coherent state. This gives the well-known phase modulation spectrum. From now on, we define the modulation index $m = 2\alpha$, which denotes the phase excursion in radians and is the usual parameter convention for phase modulation. Note that $\mathbf{S}^{(PM)}$ may not be block-diagonal for other values of ϕ , which will lead to couplings between amplitude and phase quadratures. These are therefore totally controllable by setting the initial phase ϕ of radio frequency modulation signal experimentally.

For $\Omega > 1$, we can get a similar result by block-diagonalizing \mathbf{M} into Töplitz blocks

$$\begin{cases} M_{jk} \propto i^s \sum_{m=1}^N \sin \frac{\lfloor \frac{j}{\Omega} \rfloor m \pi}{\lfloor \frac{N}{\Omega} \rfloor + 1} \sin \frac{\lfloor \frac{k}{\Omega} \rfloor m \pi}{\lfloor \frac{N}{\Omega} \rfloor + 1} \exp \left(2i \alpha \cos \frac{m \pi}{\lfloor \frac{N}{\Omega} \rfloor + 1} \right), & \text{for } k - j = \Omega s, s \in \mathbb{Z} \\ M_{jk} = 0, & \text{else} \end{cases} \quad (3.61)$$

where $\lfloor X \rfloor$ is the integer part of X .

Fig.3.3 displays numerical calculations of the \mathbf{M} matrix for $\Omega=1$ and with respective modulation depths and indices $m=0.2$ [Fig.3.3(a)] and $m=1$ [Fig.3.3(b)].

Comparing Fig.3.3(a) and Fig.3.3(b), we see that a larger m yields, as expected, more modulation sidebands, and therefore nonzero elements extending farther away from the main diagonal. When applying phase modulation to a quantum optical frequency comb to generate cluster state, those higher order modulation sidebands will create spurious weak edges, the effect of which can be fully analyzed using methods discussed in Section 3.2.

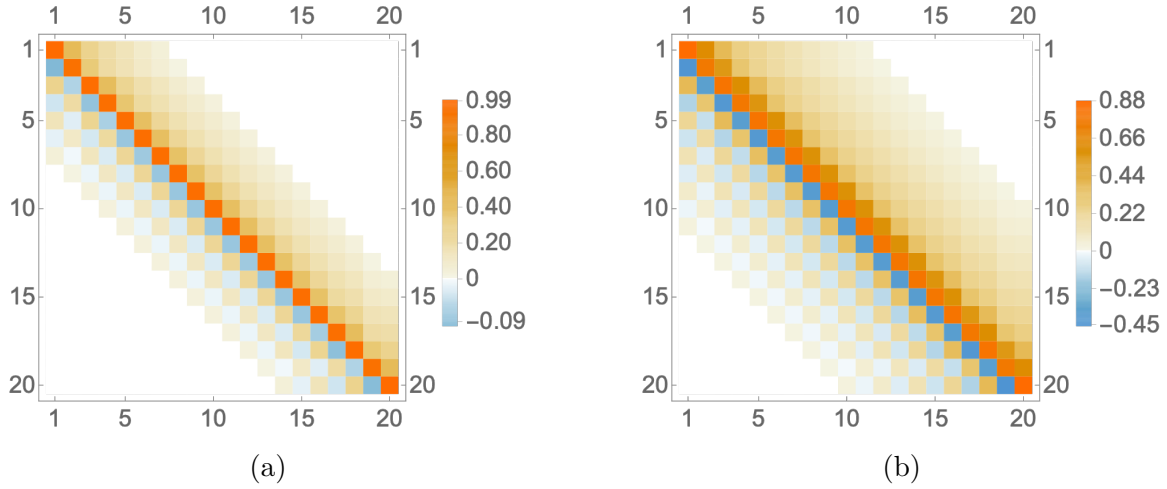


Figure 3.3: EOM \mathbf{M} matrix numerical plot. (a) EOM modulation frequency $\Omega = 1$ FSR, $m = 0.2$. (b) EOM modulation frequency $\Omega = 1$ FSR, $m = 1$.

The definition of the symplectic matrix \mathbf{S} that we'll use applies to the quadrature vector $\mathbf{x} = (\mathbf{Q}, \mathbf{P})^T$. The matrices \mathbf{S} and \mathbf{M} are then related by

$$\mathbf{S} = \begin{pmatrix} \mathbf{A} & \mathbf{B} \\ \mathbf{C} & \mathbf{D} \end{pmatrix} \equiv \begin{pmatrix} \text{Re}[\mathbf{M}] & i \text{Im}[\mathbf{M}] \\ -i \text{Im}[\mathbf{M}] & \text{Re}[\mathbf{M}] \end{pmatrix}. \quad (3.62)$$

3.4 Phase modulated quantum optical frequency comb

Unitarity of quantum mechanics requires there be as many input ports as there are output ports, hence this beamsplitting operation will have vacuum field inputs at the sideband frequencies ω_{\pm} , Fig.3.4(a). Such inputs are undesirable as random vacuum fluctuations will decorrelate squeezed quantum states. The use of a QOFC makes it possible to suppress vacuum inputs, provided Ω is a multiple of the comb's qumode spacing, a.k.a. of the free spectral range of the OPO cavity, Fig.3.4(b).

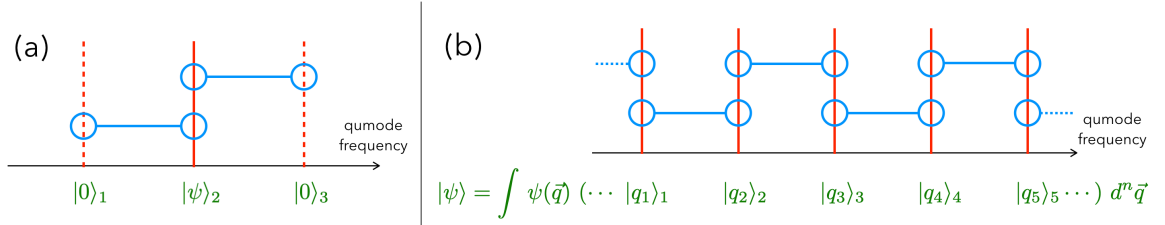


Figure 3.4: Principle of cluster state engineering by phase modulation, whose action, here in the limit of small modulation index (first-order sidebands only), is equivalent to beamsplitter mode-coupling, as per the blue lines, of the initial quantum states, in green; (a), classical phase modulation, in which *vacuum* sidebands couple in to the initial quantum state $|\psi\rangle$; (b), phase modulation of the QOFC at the mode frequency spacing: there is no vacuum input and a complex unitary operation on initial state $|\psi\rangle$ is realized.

In this chapter, I will demonstrate cluster state generation by phase modulation of the EPR QOFC emitted by a monochromatically pumped OPO below threshold. Figure 3.5 depicts the experimental configuration. A doubly resonant OPO, the cavity of which resonates both downconverted modes, is pumped at a single frequency ω_p such that frequency $\omega_p/2$ is set exactly halfway between 2 OPO mode frequencies (usually by a phaselock loop [35, 3]), as per the green arrow in Fig.3.5. This generates independent EPR qumode pairs in two-mode-squeezed (TMS) states [59, 60], a.k.a.

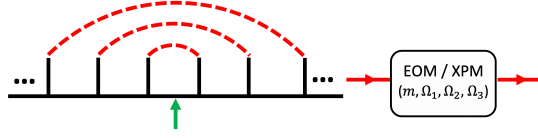


Figure 3.5: Phase modulation of a single QOFC. An OPO with a single pump frequency, whose half is denoted by the green arrow, creates TMS qumode pairs as indicated by the red dashed lines. Electro-optic phase modulation, or Kerr-medium cross phase modulation, is then done at index m and frequencies $\Omega_{1,2,3}$, all multiple of the comb tooth spacing

the EPR QOFC. While entanglement scalability is already present in this case, it manifests itself only as the scaling of the number of copies of a bipartite EPR state, rather than as the scaling of the size of a multipartite state. Phase modulation by the EOM of the OPO QOFC will change that: by modulating at one, two or three frequencies, we can knit up 1D, 2D (square-grid), 3D (cubic) cluster states. We postulate that this extends to n -hypercubic cluster states, using n modulation frequencies.

3.4.1 General procedure

In this part, I will show how we perform the numerical simulations of graphical calculations to generate CV cluster states.

Step 1: Generation of QOFC

The squeezing in the QOFC will be directly generated by an optical parametric amplifier (OPA), i.e., an OPO below threshold. The squeezing Hamiltonian of this system is

$$H = i\hbar \frac{r}{2\tau} \sum_{j=1}^N \sum_{k=1}^N (2 - \delta_{jk}) G_{jk} a_j^\dagger a_k^\dagger + \text{H.c.}, \quad (3.63)$$

where r is the squeezing parameter, τ is the interaction time, and a_j and a_k are the annihilation operators of qumodes j and k , respectively. The $N \times N$ matrix \mathbf{G} is the adjacency matrix of the \mathcal{H} -graph [61]. In graph theory, an adjacency matrix element $G_{jk} \neq 0$ denotes an edge of weight the element between vertices j and k . If the pump is monochromatic, the \mathbf{G} matrix has Hankel form, e.g., for $\omega_p = \omega_1 + \omega_N$,

$$\mathbf{G} = \begin{pmatrix} 0 & \cdots & 0 & 1 \\ \vdots & \ddots & \ddots & 0 \\ 0 & \ddots & \ddots & \vdots \\ 1 & 0 & \cdots & 0 \end{pmatrix}. \quad (3.64)$$

The \mathcal{H} -graph state has the \mathbf{Z} matrix [31]

$$\mathbf{Z} = \mathbf{V} + i\mathbf{U} = ie^{-2r\mathbf{G}} \quad (3.65)$$

Step 2: Evolution with EOM

The Heisenberg equation (Eq. 3.57) of phase modulation process, taking $\phi = -\frac{\pi}{2}$, can be written in the form

$$\frac{d\mathbf{A}^T}{dt} = \frac{m}{2\tau}\mathbf{T}\mathbf{A}^T \quad (3.66)$$

where $\mathbf{A} = (a_1, a_2, \dots, a_N)$ and \mathbf{T} is a Töplitz matrix

$$\mathbf{T} = \begin{pmatrix} 0 & -1 & & \\ 1 & 0 & -1 & \\ & 1 & 0 & -1 \\ & & & \ddots \end{pmatrix} \quad (3.67)$$

Diagonalizing $\mathbf{T} = \mathbf{R}\mathbf{T}_{\text{diag}}\mathbf{R}^{-1}$, the solution $\mathbf{A}(t) = \mathbf{M}\mathbf{A}(0)$ is given by

$$\mathbf{M} = \mathbf{R} e^{\frac{m}{2}\mathbf{G}_{\text{diag}}} \mathbf{R}^{-1}, \quad (3.68)$$

which can be easily determined by numerical calculations. Therefore the symplectic matrix \mathbf{S}_{pm} is obtained by using Eq. 3.62.

Step 3: $\frac{\pi}{2}$ phase shift

The final evolution process is to apply $\pi/2$ phase shift to properly selected modes. In order to assess whether \mathbf{V} is a valid graph adjacency matrix, we need to examine $\text{Tr}[\mathbf{U}]$ and confirm that $\text{Tr}[\mathbf{U}] \rightarrow 0$. As was mentioned above, the minimization of $\text{Tr}[\mathbf{U}]$ can be performed by applying local phase space rotations by $\frac{\pi}{2}$ to individual qumodes, which cannot modify the entanglement. Finding an algorithm to carry out this task had been an open question [31] but was recently solved by our group [44], after we completed this work. The symplectic matrix of this single mode phase rotation (see Section 2.4) is

$$\mathbf{S}_{\frac{\pi}{2}} = \begin{pmatrix} 0 & 1 \\ -1 & 0 \end{pmatrix}. \quad (3.69)$$

Here, we make use of the symmetry of the system, where a permutation symmetry can be found for qumodes symmetrically placed away from the pump's half-frequency, which therefore belong to the same EPR pair. Heeding this, we chose to apply the phase shifts (which are rotations in quantum phase space and therefore exchange Q and P —to a sign left, of course—and can thus be thought of as Fourier transforms of qumodes) to the first half of the N qumode set. This choice does lead to the desired result.

Step 4: Calculate the \mathbf{Z} matrix of the final state

We used two different methods to calculate the \mathbf{Z} matrix of the final state. First method is to use the Möbius transformation Eq. (3.26), starting from \mathbf{Z} of the QOFC, to get the \mathbf{Z} matrix after each evolution. Second method is using Eq. (3.22) to construct the covariance matrix σ_0 of QOFC from its \mathbf{Z} and then evolving this covariance matrix by

$$\mathcal{S} = \mathbf{S}_{\frac{\pi}{2}} \mathbf{S}_{pm} \mathbf{S}_{pm}^T \mathbf{S}_{\frac{\pi}{2}}^T, \quad (3.70)$$

from which the adjacency matrix \mathbf{V} and error matrix \mathbf{U} of the final graph state can be obtained.

Note about intrinsically phase-modulated OPO

The four steps discussed above is for externally modulated OPO, for which the output state is

$$|\text{out}\rangle = \exp\left(-\frac{i\tau}{\hbar} H_{PM}\right) \exp\left(-\frac{i\tau'}{\hbar} H_{TMS}\right) |0\rangle^{\otimes N}, \quad (3.71)$$

We also performed the calculations for an intrinsically phase-modulated OPO (e.g. with intracavity electro-optic modulation—EOM), described by

$$|\text{out}\rangle = \exp\left[-\frac{i\tau'}{\hbar} (H_{TMS} + H_{PM})\right] |0\rangle^{\otimes N}. \quad (3.72)$$

The general calculation procedure for an intrinsically phase-modulated OPO state is the same as it of the externally modulated OPO discussed above, except that the

Hamiltonian of the QOFC and the EOM are combined into one expression

$$\begin{aligned}
H &= H_s + H_p m \\
&= i\hbar \frac{r}{2\tau} \sum_{j=1}^N \sum_{k=1}^N (2 - \delta_{jk}) G_{jk} a_j^\dagger a_k^\dagger + \hbar \frac{\alpha}{\tau} e^{-i\phi} \sum_{j=-\infty}^{\infty} a_j a_{j+\Omega}^\dagger + \text{H.c.}
\end{aligned} \tag{3.73}$$

Using this Hamiltonian to solve the Heisenberg equation to get the solution

$$\frac{d(\mathbf{A}, \mathbf{A}^\dagger)}{dt} = \begin{pmatrix} \mathbf{T} & \frac{r}{2}\mathbf{G} \\ \frac{r}{2}\mathbf{G} & \mathbf{T}^* \end{pmatrix} (\mathbf{A}, \mathbf{A}^\dagger)^T. \tag{3.74}$$

In all cases presented in the next section, i.e., the 1D, 2D, and 3D graphs, we calculated both the extrinsic [Eq. (3.71)] and intrinsic [Eq. (3.72)] cases. We found that both methods give the same graphs, with comparable edge weights, but that the intrinsic method has a lower level of error (see the plots in the following subsections). Because of the experimental simplicity of just placing an EOM after an OPO, I will present these extrinsic-OPO results thereby placing an upper bound on the imperfections.

3.4.2 Generation of 1-d cluster state

The first case we study is the simplest, depicted in Fig.3.6: There is only one EOM modulation frequency which is set to $\Omega = 1$ in this case, with squeezing parameter $r = 2.3$.

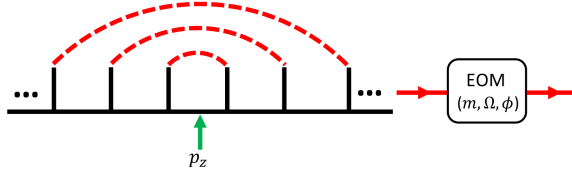


Figure 3.6: Phase modulation of a single QOFC. An OPO with a single pump frequency, whose half is denoted by the green arrow, creates TMS qumode pairs as indicated by the red dashed lines. An EOM applies phase modulation with index m , frequency Ω , and phase ϕ (irrelevant in this case).

Effect of modulation index

Following the steps in Section 3.4.1, we derive the complex adjacency matrix \mathbf{Z} of the created Gaussian state for $m=0, 0.1, 0.2, 0.5$, and 1 rad. Figure 3.7 displays the real and imaginary parts of \mathbf{Z} , \mathbf{V} and \mathbf{U} .

It is clear that phase modulation yields multipartite entanglement. We now examine the particular graphs that can be generated by this method, turning first to the effect of the modulation index parameter m . The initial case $m = 0$ corresponds to EPR pairs from the OPO with no phase modulation. When the latter is turned on, additional edges are created, whose weights increase with m , as the EPR weights decrease. The classical FM spectra in the left column of Fig.3.7 give a good illustration of the effect on the quantum graph of the oscillations with m of the Bessel-function amplitudes.

The onset of next-nearest neighbor couplings in the quantum graph coincides, with the growth of the first-order modulation sidebands, decrease of the carrier, and rise of the second harmonic sidebands. Such nonlocal graph edges are a known hindrance to one-way quantum computing [26, 27, 28]. However, we will show later that this problem can be circumvented upon closer, rigorous inspection of the edges' weights, which can always be found to be too small to be observable, when m isn't

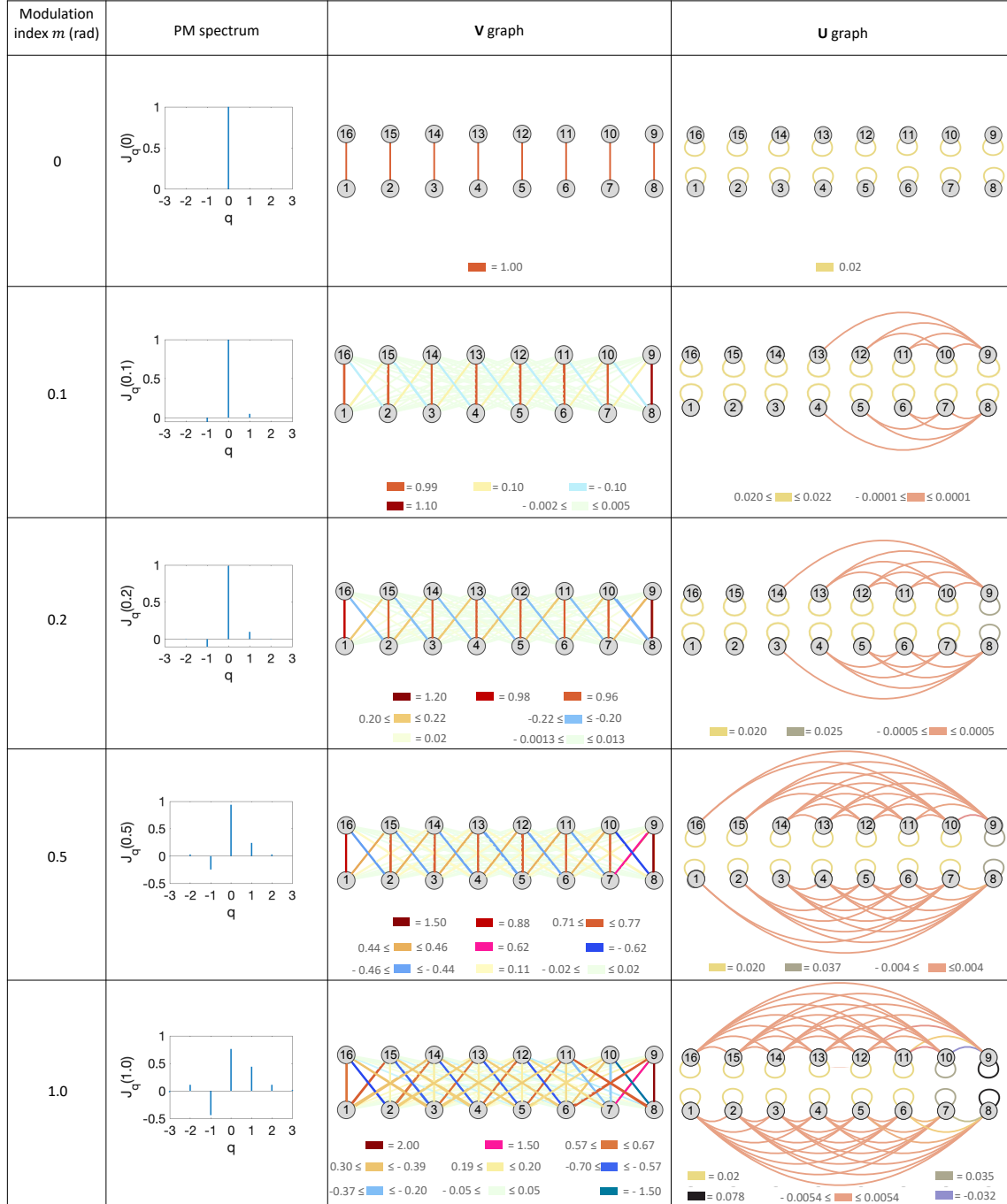


Figure 3.7: **V** and **U** graphs for the state generated by OPO-extrinsic PM at $\Omega_1=1$ and $r=2.3$, for different m . The pump frequency is equal to the sum of the frequencies of all vertical qumode pairs in the **V** and **U** graph columns. Note that the mode labeled “0” in the PM spectrum column is any of the QOFC qumodes in the **V** and **U** graph columns. All self loops that have the same color in each **U** graph have a value of 0.02, regardless of the value of m .

too large. Note also that this optimal m will decrease as the squeezing parameter r increases.

Remarkably, the imaginary part of the graph (rightmost column of Fig.3.7), given by the error matrix \mathbf{U} , complements the \mathbf{V} graph, which clearly tends toward a complete bipartite graph with increasing m . In a sense, the qumode correlations described by \mathbf{U} leave \mathbf{V} globally invariant in terms of its bipartite structure, i.e., while \mathbf{V} only connects qumode set $\{1, \dots, 8\}$ to qumode set $\{9, \dots, 16\}$ in Fig.3.7, \mathbf{U} only connects qumodes within each of these two sets.

It is important to prove that $\text{Tr}[\mathbf{U}] \rightarrow 0$ when $r \gg 1$, as illustrated in Fig.3.8, where $\text{Tr}[\mathbf{U}]$ is plotted and shown to adhere to the theoretical value obtained analytically for two-mode squeezed states [31]. It means that PM of two-mode-squeezed

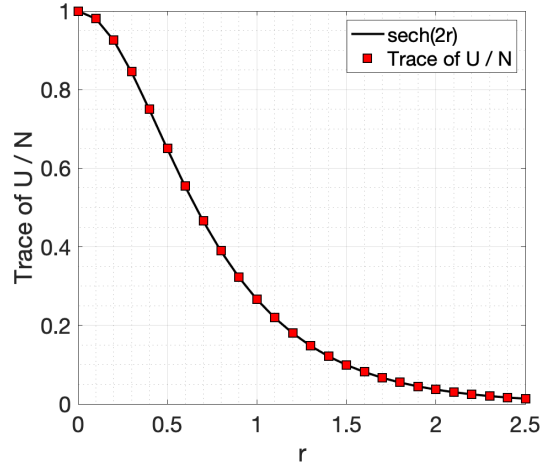


Figure 3.8: Plot of the average trace of \mathbf{U} versus the squeezing parameter r , compared to the function $\text{sech}(2r)$. This \mathbf{U} matrix is for the externally modulated QOFC at $\Omega_1=1$.

pairs doesn't detract from the fact that the overall cluster state error is solely determined by the amount of initial squeezing. Because of \mathbf{U} being symmetric positive semidefinite, it must tend to zero as a whole when its trace tends to zero as per

requirement (ii). However, the requirement (i) remains crucial as we cannot reach the infinite squeezing limit experimentally.

1-d ladder state

Following the procedures in Section 3.2.2, I will present here how the \mathbf{U} changes when the spurious edges are trimmed.

First, we analyzed the deviation, which is the trace of \mathbf{U} ($\text{Tr}[\mathbf{U}]$), to the cluster state described by \mathbf{V} . The \mathbf{V} matrix trimming threshold value ε_{\min} for a given squeezing level is depicted on Fig.3.9. We can see that truncation doesn't change $\text{Tr}[\mathbf{U}]$ for

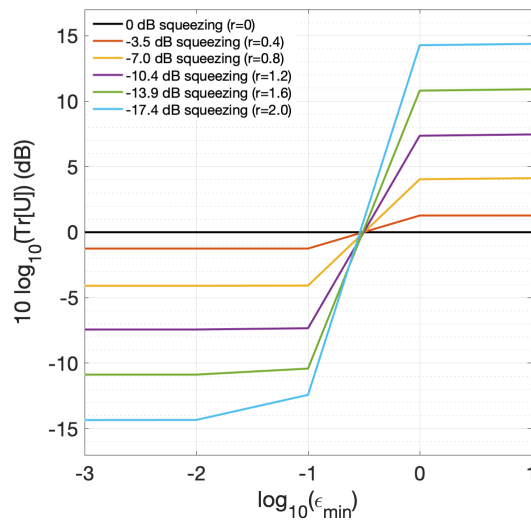


Figure 3.9: Effect of graph “trimming” (removing all graph edges smaller than ε_{\min}), on the trace of \mathbf{U} , in the case of the state shown in Fig.3.7 with $m = 0.2$.

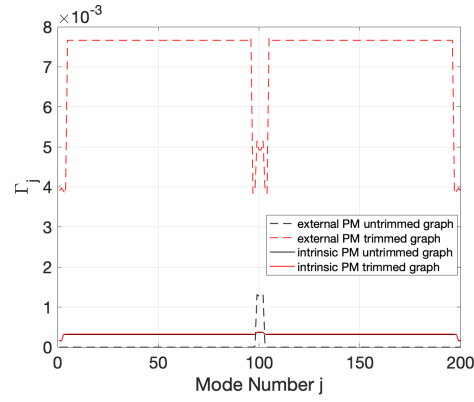
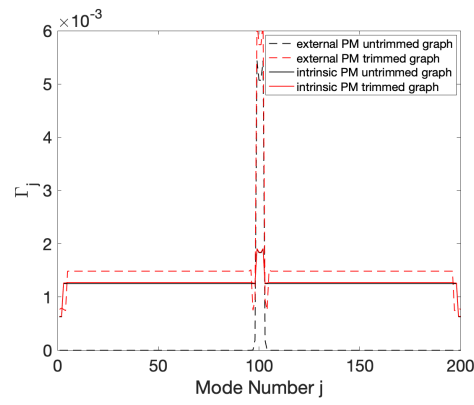
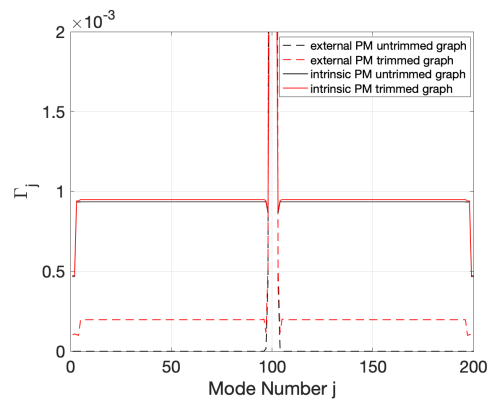
low enough values of ε_{\min} , $\text{Tr}[\mathbf{U}]$ staying essentially at the squeezing level. As ε_{\min} increases, $\text{Tr}[\mathbf{U}]$ rises because we are trimming graph edges which are now detectable by quadrature measurements in the laboratory. Higher values of squeezing mandate lower ε_{\min} : for example, $\varepsilon_{\min} = 10^{-1}$ clearly raises the $\text{Tr}[\mathbf{U}]$ for squeezing > 10 dB

(Fig.3.9). Any value of ε_{\min} above 1 should, of course, be nonsensical as the graph is ultimately destroyed and the computed error rises sharply in confirmation of this.

The important conclusion from this graph is that there always exist an ε_{\min} such that requirement (ii) is fulfilled. Hence, graph trimming can always be performed, no matter how large the squeezing is, which ensures one can perform graph trimming above the fault tolerance threshold. Unsurprisingly, ε_{\min} must decrease when r increases. This will require lowering m in turn so as to keep the spurious edges weak. While this also results in a trend of lower edge weights, also as the dimensionality of the graph increases, note that our trimming procedure of increasing ε_{\min} , until just before $\text{Tr}[\mathbf{U}]$ sharply increases, does ensure that the edges are significant, i.e., that their measurement does yield a quantum processing effect.

Second, we computed the components of error vector $\mathbf{\Gamma}$ of \mathbf{U}' as plotted in Fig.3.10, which addresses both cases of cascaded EPR pair generation and PM, and integrated PM in the OPO. For both cases, unsurprisingly, trimming the graph yields an increase of the error Γ_j (red dashed and solid lines) but, clearly, within manageable levels, because Γ_j are of the order 10^{-3} regardless of whether spurious edges are trimmed or not.

At this point, we come to the result that the weak edges are ignorable in the whole complex graph so that we can focus on the cluster states constructed by the dominant edges. We only have to limit the modulation index m to low enough a value, keeping the PM couplings nearest-neighbor so as not to get nonlocal edges. The resulting graph is given by Fig.3.11(a). Swapping every other vertical pair of qumodes shows the graph to be a 1D “ladder” whose rungs are the initial EPR-pair qumodes. This dual graph structure connected by the initial EPR pairs will actually be a feature of the 2D and 3D graphs as well. In order to simplify the graph rendering in this

(a) $m = 0.05, r = 2.3$ (b) $m = 0.1, r = 1.2$ (c) $m = 0.15, r = 0.4$ Figure 3.10: Γ plot for PM either external or internal to the OPO. $\Omega_1 = 1, \varepsilon_{\min} = 0.01$.

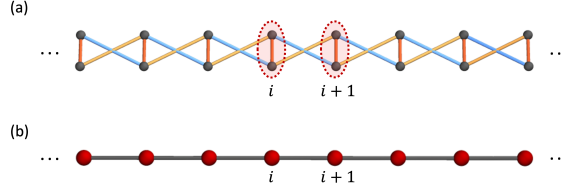


Figure 3.11: (a), \mathbf{V} graph of Fig.3.7, revealing its typical structure for 1D cluster state. Two modes that are in the red dashed circle are the EPR-qumodes. (b), compact representation of the graph using EPR macronodes.

case, we will bunch these EPR pairs into “EPR macronodes,” as in Fig.3.11(b). This ladder state spans the whole phasematching bandwidth of the OPO, which can reach 10 THz in our previous work [62]. With a typical mode spacing of 1GHz [35, 3], this yields on the order of 10^4 entangled qumodes in this linear cluster state.

As is well known, the 1D graph isn’t enough to generate the universal gate set in one-way quantum computing, for which a 2D graph is required. I will discuss the generation of 2D graph next.

3.4.3 Generation of 2-d cluster state

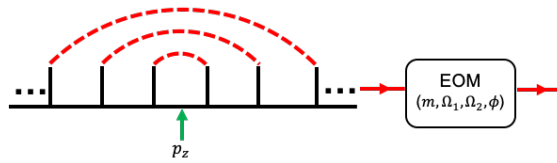


Figure 3.12: Phase modulation of one QOFC at two modulation frequencies Ω_1 and Ω_2 . Same conventions as Fig.3.6.

Based on configuration of making 1D graph as shown in Fig.3.6, we add another modulation frequency to the EOM (Fig.3.12), which will give the EOM Hamiltonian

in the form that

$$H = \hbar \left[\frac{\alpha_1}{\tau} e^{-i\phi_1} \sum_{j=-\infty}^{\infty} a_j a_{j+\Omega_1}^\dagger + \frac{\alpha_2}{\tau} e^{-i\phi_2} \sum_{j=-\infty}^{\infty} a_j a_{j+\Omega_2}^\dagger \right] + \text{H.c.}, \quad (3.75)$$

where τ is the interaction time, $\Omega_{1,2}$ are the two modulation frequencies. Here we set $\phi_1 = \phi_2 = \pi/2$, $\alpha_1 = \alpha_2$, and follow the same procedure as in the 1D case, which yields the square-grid cluster state of Fig.3.13.

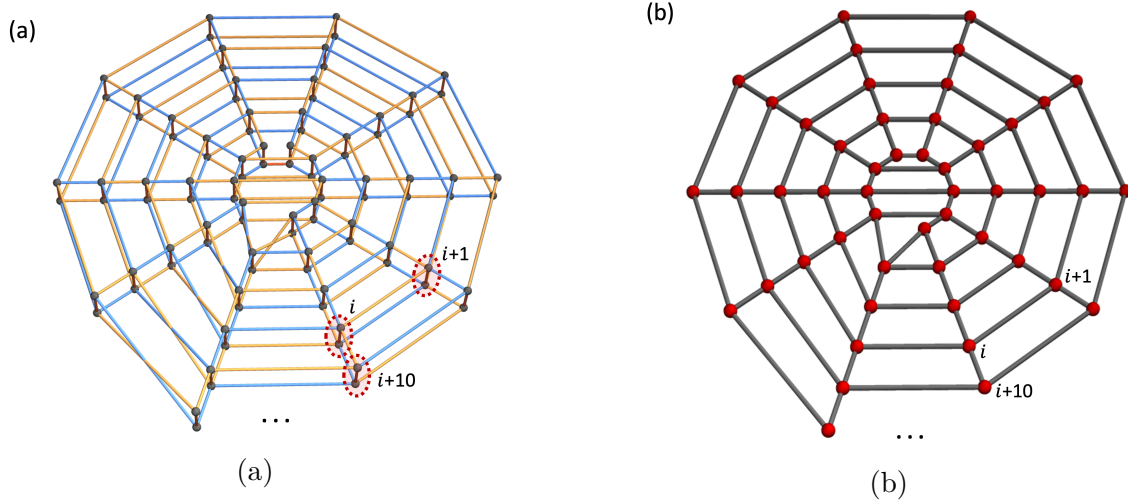
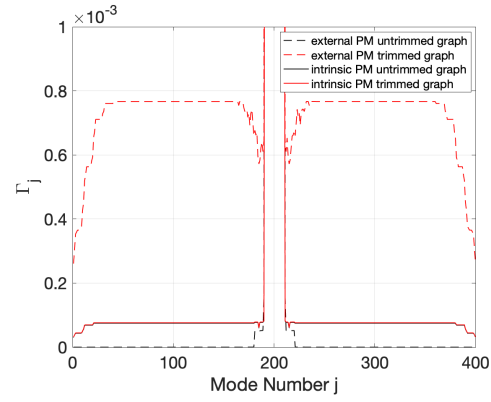
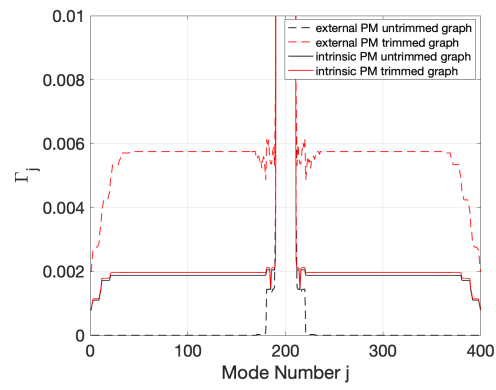
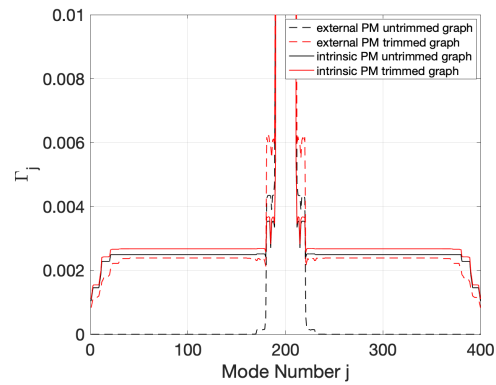


Figure 3.13: (a), square-grid cluster state created with $\Omega_1=1$, $\Omega_2=10$. Two modes circled by red dashed lines are EPR-qumodes, one of which is on the upper layer and the other one is on the bottom layer. (b), same graph, over EPR macronodes. The width of this square lattice is the number of “spokes” in the graph: $\Omega_2/\Omega_1 = 10$.

The Γ vector plot for 2-d graph state are shown in Fig.3.14, which are correspond to square-grid lattice generated with phase modulation frequencies $\Omega_1 = 1$, $\Omega_2 = 10$ at r equal to 2.3, 1.2 and 0.4. Here I only present the conclusion that the value Γ remains small when those spurious edges are neglected. The details of this argument will be discussed along with 3-d graphs in the next part.

One can interpret this case in the following way: PM at frequency $\Omega_1=1$ creates next-neighbor coupling in the QOFC which forms a ladder graph; PM at frequency

(a) $r = 2.3$. $m = 0.01$, $\varepsilon_{\min} = 0.001$ (b) $r = 1.2$. $m = 0.05$, $\varepsilon_{\min} = 0.01$ (c) $r = 0.4$. $m = 0.1$, $\varepsilon_{\min} = 0.01$ Figure 3.14: Γ plot for PM either external or internal to the OPO. $\Omega_1 = 1, \Omega_2 = 10$.

$\Omega_2=10$ then introduces additional coupling every 10 modes which is tantamount to spiraling the ladder into the two-layer square-grid cluster state of Fig.3.13(a). As in Fig.3.11(b), a more streamlined version of the graph can be obtained by considering EPR macronodes, Fig.3.13(b).

As was mentioned earlier, the width of the square lattice, which is the number of "spokes", is simply the ratio Ω_2/Ω_1 , the total number N of qumodes being determined by the phasematching bandwidth of the OPO's nonlinear medium. In the case of our previous experiments [35, 3], for which we estimated $N \sim 10^4$ [62], a 100×100 square cluster grid could therefore be created with PM at 1 and 100 GHz for a 1 GHz mode spacing. Note also that, in this case, the quasi-phasematching bandwidth can be further engineered to be larger.

This is an important result because the square-grid cluster state is a resource for universal quantum computing. Note that this is true even though the cluster state is a Gaussian state and that universal quantum computing requires non-Gaussian resources for exponential speedup and quantum error correction. This is strictly equivalent to the qubit case where cluster states stabilized by Pauli operators, globally invariant under Clifford operations (just like CV clusters are stabilized by Weyl-Heisenberg displacements, globally invariant under Gaussian operations), even though non-Clifford resources are required to achieve exponential speedup. In both cases, the necessary respective non-Gaussian and non-Clifford gates can be realized by like measurements on the cluster state.

3.4.4 Generation of 3-d cluster state

Adding another modulation frequency adds another dimension to the EPR-macronode graph, extending this procedure to yield hypercubic cluster graphs. We illustrate this in the 3D case, which is relevant to quantum computing because the 3D architecture is a known base for implementing topological error encoding over cluster states [19].

With modulation frequencies $\{\Omega_1, \Omega_2, \Omega_3\} = \{1, 8, 80\}$, the quantum derivation yields the graph state pictured over EPR macronodes in Fig.3.15. The 6-edge valence

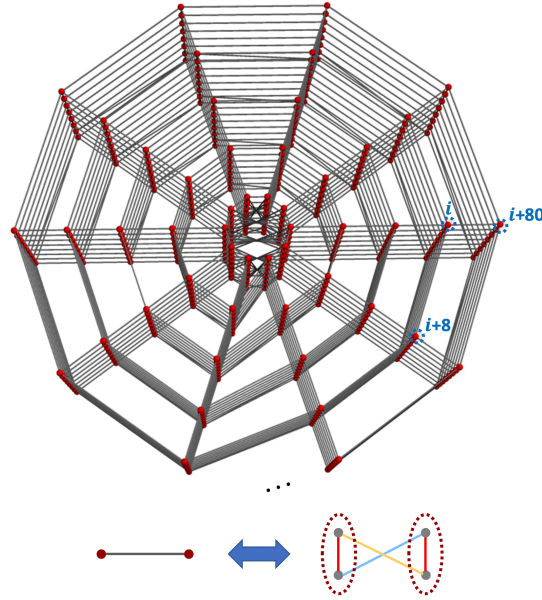


Figure 3.15: Cubic cluster state, over $N=400$ EPR macronodes, obtained from $\{\Omega_1, \Omega_2, \Omega_3\} = \{1, 8, 80\}$. Number of "spokes":10. Length: 8 macronodes. Spoke length: 5 macronodes.

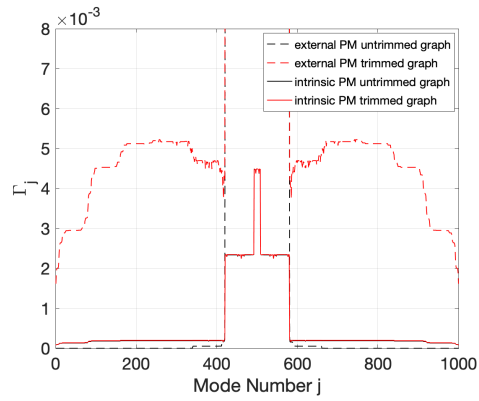
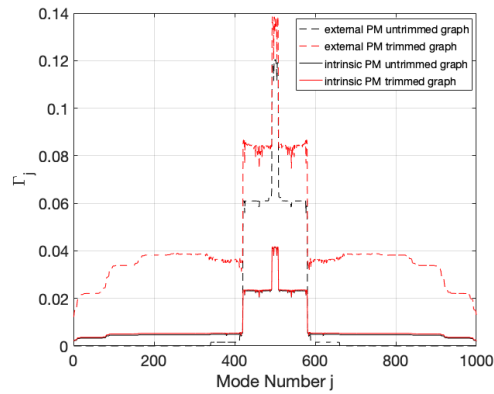
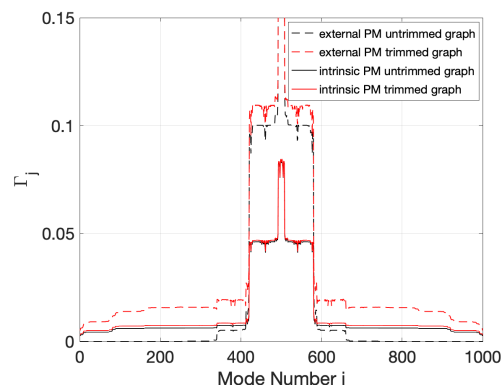
of each graph vertex is clear in their vast majority. Note that, as always for cluster states, any local imperfections (graph center) in the graph can be removed by single-qumode measurements [2, 30, 23].

Finally, the ratio of PM frequencies determines the graph's structure, here cylindrical: the number of "spokes" is set by Ω_3/Ω_2 and the length of the cylinder is set

by Ω_2/Ω_1 . The radius of the spokes increases with the mode number N as N/Ω_3 . In the example of Fig.3.15, a cubic cluster state is created over 400 macronodes in cylindrical shape with 10 "spokes", 5 set of macronodes in the radial direction, and a cylinder 8 macronodes long.

Now I will present how the \mathbf{U} will change by trimming the spurious edges. The $\mathbf{\Gamma}$ vector plot for 3-d graph state are shown in Fig.3.16, which are correspond to cubic graph generated with phase modulation frequencies $\Omega_1 = 1$, $\Omega_2 = 8$, $\Omega_3 = 80$ at r equal to 2.3, 1.2 and 0.4. In every case, the effect of spurious graph edge stays deeply buried in the squeezed noise. The components of error vector of \mathbf{U}' were computed for all 1000 qumodes in the state, which addresses both cases of cascaded EPR pair generation and PM, and integrated PM in the OPO. In the former case (black dashed lines), only a small portion of the graph (the center of Fig.3.15) has values of Γ_j marginally larger than 0.1, and these can be measured out. Remarkably, the values of Γ_j are close to zero for the vast majority of modes of the graph (0-400 and 600-1000), which corresponds to the bulk of the cubic lattice. Unsurprisingly, trimming the graph yields an increase of the error Γ_j (red dashed lines) but, clearly, within manageable levels.

In the case of PM intrinsic to the OPO (solid lines), the cubic graph is clearly "cleaner" from the start as the values of are much lower and trimming has much less of an effect, while the graph edge weights (from \mathbf{V}) are comparable.

(a) $r = 2.3$. $m = 0.01$, $\varepsilon_{\min} = 0.001$.(b) $m = 0.05$, $r = 1.2$, $\varepsilon_{\min} = 0.01$.(c) $r = 0.4$. $m = 0.1$, $\varepsilon_{\min} = 0.01$ Figure 3.16: Γ plot for PM either external or internal to the OPO. $\Omega_1 = 1$, $\Omega_2 = 8$, $\Omega_3 = 80$

Conclusion

We demonstrated that the “bare bone” resources constituted by a monochromatically pumped, below-threshold OPO along with phase modulation at multiples on the cavity spacing enable the generation of CV cluster states of arbitrary dimension, to arbitrarily low error levels compatible with the fault tolerance threshold predicted for CV quantum computing. The graph dimension is fully determined by the number and the ratio of phase modulation frequencies. For all squeezing levels, there exist modulation parameters that yield experimentally valid cluster states. Of particular interest is the enhanced performance of phase modulation intrinsic to the OPO, as opposed to external to it. This experimental configuration is remarkably simple and compact and a marked simplification of all previous experimental realizations of large-scale cluster states, CV or otherwise. Note that these cluster states are deterministically and unconditionally generated, to the difference of other frequency-comb approaches that propose probabilistic linear-optics quantum computing [63] or employ postselected photonic qubits [64]. Note that the frequency bandwidth of the fastest modulator involved dictates the final size of the generated cluster state. Even though we have used, throughout this paper, the example of an EOM for the phase modulator, even faster options exist such as cross phase modulation in a Kerr medium. Finally, the conceptual simplicity of this approach makes it well suited for implementations in integrated photonics.

Chapter 4

Optical system stabilization

Based on the theory in Chap. 3, we designed an experiment. The schematic experimental setup is shown in Fig. 4.1. In this experiment, Laser 1 (L1) emits an IR beam at 1064 nm. It is divided into 4 parts. First part of L1 passes through a doubling crystal and generates a 532 nm light which is used as pump beam inserted into OPO. The pump beam power is 550 mW and polarized at z direction with respect to zzz PPKTP crystal, which is the second order nonlinear crystal inside the OPO cavity. The PPKTP crystal converts one pump photon into 2 photons at 1064 nm, which are the quantum light consists of a lot of two-mode squeezed photon pairs. The OPO has a 4 mirror bow-tie cavity and emits QOFC with free spectral range equal to 1 GHz. The QOFC then passes through an EOM and interferes with local oscillator (LO) to perform balanced heterodyne measurement. LO is the second part of L1. The frequency of LO is shifted by 50 MHz using an acousto-optic modulator (AOM) and LO power is 7.1 mW. The third part of L1 is locking beam which is used to perform Pound-Drever-Hall locking to stabilize the OPO cavity length to make the cavity resonant frequency at L1 frequency. It is inserted into OPO in the counter propagate direction relative to the quantum light. The fourth part of L1 is the probe beam which has the power 37.4 μ W. It propagates in the same direction as the quantum light. The probe beam is used to monitor the quantum light phase, which will be discussed in details in the next chapter. In order to increase the system stabil-

ity, two phase lock loops are used to stabilize the phase of the pump beam and LO. Both the phase of pump and LO are locked to the probe beam through the "Laser Lock Box" instrument in Moku:Lab. Moku:Lab provided by Liquid Instrument is a reconfigurable hardware platform that combines the digital signal processing power of an FPGA with versatile analog inputs and outputs. It has multiple instrument to perform different tasks. We also use the "Laser Lock Box" to perform the PDH locking for OPO.

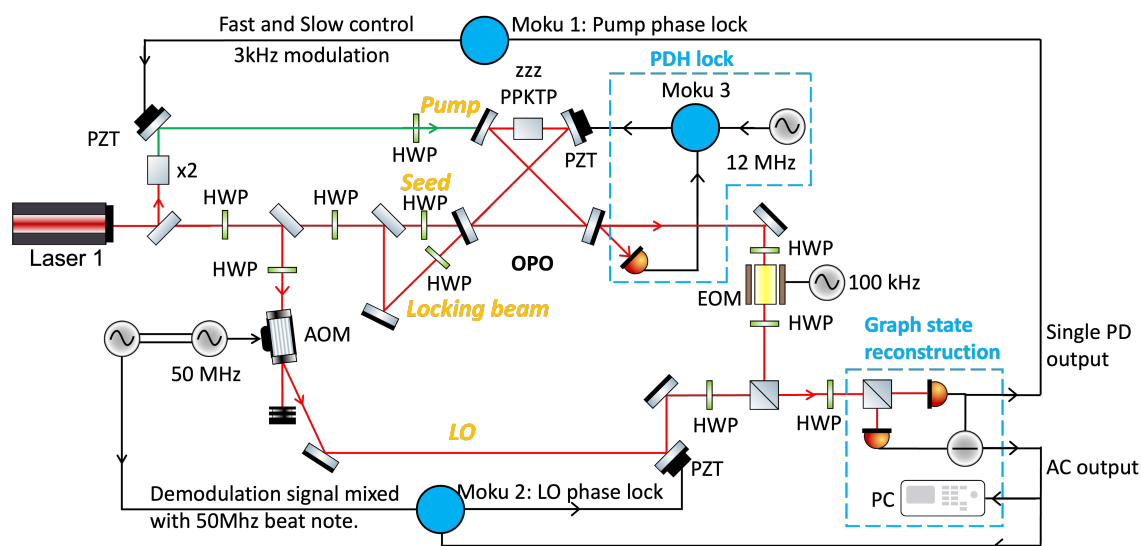


Figure 4.1: Experimental setup. HWP: half wave plate. PZT: piezoelectric transducer. Moku: Moku:Lab. PC: personal computer. EOM: electro-optic modulator. AOM: acousto-optic modulator. PDH: Pound-Drever-Hall locking.

In this chapter, I will first introduce the OPO that is used in our experiment. Then I will discuss the methods that are used to perform the PDH locking, pump-probe beam phase locking and LO-probe beam phase locking and present the locking results.

4.1 Optical parametric oscillator

Optical parametric oscillator (OPO) is an important tool in quantum optics used to generate quantum optical frequency comb (QOFC), consisting of a large number of two-mode squeezed state. OPO has two essential elements: an optical cavity and nonlinear medium. I will review some basic knowledge about the optical cavity and the nonlinear optics. Detailed derivations can be found in [65].

4.1.1 Optical cavity

Optical cavity is also known as optical resonator. For free-space optics, optical cavity is constructed by at least two mirrors. Fig. 4.2 shows different kinds of cavities. A four-mirror ring cavity Fig. 4.2 (c) is used for our OPO, in which the light propagates in one direction during a round trip. Here I will take a two-mirror cavity (Fig. 4.2 (a)) as an example to illustrate some properties without loss of generality.

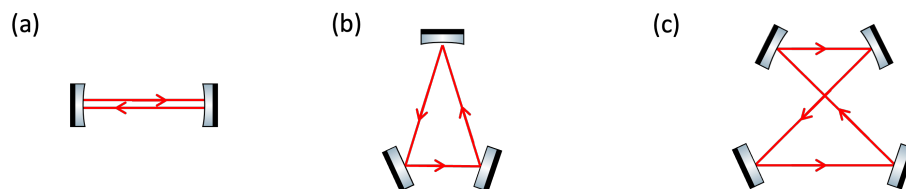


Figure 4.2: Different kinds of cavities. (a) Two-mirror cavity. (b) Three-mirror ring cavity. (c) Four-mirror ring cavity.

Free spectral range

Considering a two-mirror cavity, the reflection coefficient of two mirrors are r_1 and r_2 . An incident optical field is $E_0 = |E_0|e^{i2\pi\nu t + \phi_0}$. The optical field inside the cavity

as shown in Fig.4.3 is

$$E = E_1 + E_2 + E_3 + \dots \quad (4.1)$$

Infinitesimal fields can build up only when light wave can reproduce itself after each

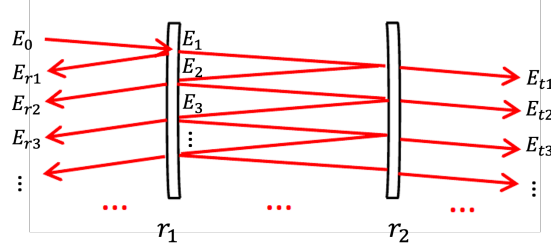


Figure 4.3: Optical field inside, reflected and transmitted from a two-mirror cavity. E_0 is the input field. r_1 and r_2 are the reflection coefficient of those two mirrors.

round trip, so that all the fields inside the cavity have constructively interference. The phase shift caused by each round trip of propagation must be multiples of 2π :

$$\phi = kL = \frac{2\pi\nu L}{c} = 2\pi n, \quad n = 1, 2, 3, \dots, \quad (4.2)$$

where the wave vector $k = \frac{2\pi\nu}{c}$, ν is the light frequency and L is the length of round trip inside a cavity. Therefore, the frequency of the light that can be stored in the cavity must satisfy

$$\nu = \frac{nc}{L}, \quad n = 1, 2, 3, \dots \quad (4.3)$$

The frequencies satisfy this condition forms a frequency comb as shown in Fig.4.4. Each peak represents a cavity mode with different frequency. They are equally spaced to form a frequency comb. The frequency difference between two nearest peak is called the free spectral range (FSR) of the cavity

$$\text{FSR} = \nu_{n+1} - \nu_n = \frac{c}{L}. \quad (4.4)$$

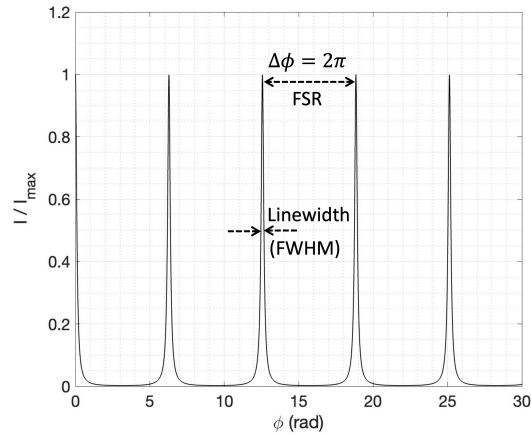


Figure 4.4: Frequency comb generated by a two-mirror cavity. The reflectance coefficients of two mirrors are $r_1 = r_2 = 0.95$. The y axis is the ratio between the intensity of field inside the cavity (Eq. (4.7)) and the maximum value. The x axis is the phase of the field given by Eq. (4.2).

Spectral linewidth

The cavity has losses caused by mirror reflections and the absorption in the medium. The field will be attenuated after each round trip. The complex attenuation factor is

$$h = |r| e^{-i\phi}. \quad (4.5)$$

For a two-mirror cavity as shown in Fig.4.3, neglecting the medium absorption, $r = r_1 r_2$ and the phase change after a round trip given by Eq. (4.2) is $\phi = 2\pi\nu L/c$. The

field after the first round trip $E_2 = hE_1$. The total field inside the cavity is

$$\begin{aligned}
 E &= E_1 + E_2 + E_3 + \dots \\
 &= E_1 (1 + h + h^2 + \dots) \\
 &= \frac{E_1}{1 - h}.
 \end{aligned} \tag{4.6}$$

The intensity of field inside the cavity is given by

$$\begin{aligned}
 I &= |E|^2 \\
 &= \frac{I_1}{1 + |r|^2 - 2|r|\cos\phi} \\
 &= \frac{I_1}{1 + |r|^2 - 2|r|(1 - 2\sin^2\frac{\phi}{2})} \\
 &= \frac{I_1}{(1 - |r|)^2 \left(1 + \frac{4|r|}{(1-|r|)^2} \sin^2\frac{\phi}{2}\right)},
 \end{aligned} \tag{4.7}$$

where $I_1 = |E_1|^2$. The plot of intensity versus the phase ϕ is shown in Fig.4.4. The finesse is defined as

$$\mathcal{F} = \frac{\pi\sqrt{|r|}}{1 - |r|}. \tag{4.8}$$

Therefore Eq. (4.7) becomes

$$I = \frac{I_1}{(1 - |r|)^2 [1 + (2\mathcal{F}/\pi)^2 \sin^2\frac{\phi}{2}]}. \tag{4.9}$$

When $\phi = n\pi, n = 0, 1, 2, \dots$, the maximum intensity is

$$I_{max} = \frac{I_1}{(1 - |r|)^2}. \tag{4.10}$$

When the phase term satisfies $(2\mathcal{F}/\pi)^2 \sin^2 \frac{\phi}{2} = 1$, the intensity decreases to half of the maximum. With $\mathcal{F} \gg 1$, the full width of half maximum (FWHM) is

$$\delta\nu \approx \frac{\text{FSR}}{\mathcal{F}}, \quad (4.11)$$

because of Eq. (4.2) and $\delta\phi \approx 2\pi/\mathcal{F}$.

Cavity transmission and reflection coefficient

As shown in Fig.4.3, adding all the fields on the left side of the cavity gives the reflected light of the cavity

$$\begin{aligned} E_r &= E_{r_1} + E_{r_2} + E_{r_3} + \dots \\ &= -r_1 E_0 + t_1^2 r_2 e^{-i\phi} E_0 + t_1^2 r_2 e^{-i\phi} h E_0 + t_1^2 r_2 e^{-i\phi} h^2 E_0 \dots \\ &= -r_1 E_0 + \frac{t_1^2 r_2 e^{-i\phi}}{1-h} E_0 \\ &= \frac{r_2 e^{-i\phi} - r_1}{1-h} E_0. \end{aligned} \quad (4.12)$$

The reflection coefficient of the cavity is

$$R = \frac{E_r}{E_0} = \frac{r_2 e^{-i\phi} - r_1}{1-h}. \quad (4.13)$$

Similarly, adding all the fields on the right side of the cavity gives the transmitted

light of the cavity

$$\begin{aligned}
 E_t &= E_{t1} + E_{t2} + E_{t3} + \dots \\
 &= t_1 t_2 e^{-i\frac{\phi}{2}} E_0 + t_1 t_2 e^{-i\frac{\phi}{2}} h E_0 + t_1 t_2 e^{-i\frac{\phi}{2}} h^2 E_0 + \dots \\
 &= \frac{t_1 t_2 e^{-i\frac{\phi}{2}}}{1 - h} E_0.
 \end{aligned} \tag{4.14}$$

The transmission coefficient of the cavity is

$$T = \frac{E_t}{E_0} = \frac{t_1 t_2 e^{-i\frac{\phi}{2}}}{1 - h}. \tag{4.15}$$

4.1.2 Nonlinear crystal

Besides optical cavity, another important constituent of OPO is a nonlinear medium. A nonlinear medium is used to generate the squeezed states. In our experiment, we used a second order nonlinear crystal as nonlinear medium. I will introduce the basic concepts of second order nonlinear optics. Some great references I used are [66, 67].

In a linear dielectric medium, the polarization $P(t)$ in a unit volume is proportional to the input optical field $E(t)$

$$P(t) = \epsilon_0 \chi^{(1)} E(t), \tag{4.16}$$

where ϵ_0 is the permittivity of free space and $\chi^{(1)}$ is the linear susceptibility of the medium. In a nonlinear dielectric medium, there is nonlinear relationship between P

and E , so that P can be expressed as power series of E

$$\begin{aligned} P(t) &= \epsilon_0 [\chi^{(1)}E(t) + \chi^{(2)}E^2(t) + \chi^{(3)}E^3(t) + \dots] \\ &= P^{(1)}(t) + P^{(2)}(t) + P^{(3)}(t) + \dots, \end{aligned} \quad (4.17)$$

where $\chi^{(2)}$ and $\chi^{(3)}$ are the second and third order nonlinear susceptibility, $P^{(2)}(t)$ and $P^{(3)}(t)$ are the second-order and third-order nonlinear polarization. In general, because the second-order nonlinear interaction is much stronger than the third-order and other higher order nonlinear interaction, $P^{(2)}(t) \gg P^{(3)}(t) \gg \dots$, we consider only the second-order effect and neglect all the higher order nonlinear interactions.

For the second order nonlinear interactions, three wave mixing happens. Consider two optical fields with frequencies ω_1 and ω_2 and amplitude E_1 and E_2 inserted into the nonlinear medium, the total field is

$$E(t) = E_1 e^{-i\omega_1 t} + E_2 e^{-i\omega_2 t} + c.c. \quad (4.18)$$

The second order nonlinear polarization becomes

$$\begin{aligned} P^{(2)}(t) &= \epsilon_0 \chi^{(2)} E^2(t) \\ &= \epsilon_0 \chi^{(2)} [E_1^2 e^{-2i\omega_1 t} + E_2^2 e^{-2i\omega_2 t} + 2E_1 E_2 e^{-i(\omega_1 + \omega_2)t} \\ &\quad + 2E_1 E_2^* e^{-i(\omega_1 - \omega_2)t} + c.c.] + 2\epsilon_0 \chi^{(2)} [E_1 E_1^* + E_2 E_2^*]. \end{aligned} \quad (4.19)$$

There are several components with difference frequencies which correspond to different physical processes. The second-harmonic generation (SHG) is the process that

makes the frequency ω_1 and ω_2 doubled. The SHG polarization is

$$P(2\omega_1) = \epsilon_0 \chi^{(2)} E_1^2 e^{-2i\omega_1 t}, \quad (4.20)$$

$$P(2\omega_2) = \epsilon_0 \chi^{(2)} E_2^2 e^{-2i\omega_2 t}. \quad (4.21)$$

Sum-frequency generation (SFG) is to generate the field with the sum frequencies of two input fields. SFG polarization is

$$P(\omega_1 + \omega_2) = 2\epsilon_0 \chi^{(2)} E_1 E_2 e^{-i(\omega_1 + \omega_2)t}. \quad (4.22)$$

Difference-frequency generation (DFG) is to generate the field with the difference frequencies of two input fields. DFG polarization is

$$P(\omega_1 - \omega_2) = 2\epsilon_0 \chi^{(2)} E_1 E_2^* e^{-i(\omega_1 - \omega_2)t}. \quad (4.23)$$

Therefore, the second order nonlinear interaction is three wave mixing process. Considering three optical field with ω_1 , ω_2 and ω_3 , with the condition $\omega_3 = \omega_1 + \omega_2$, the coupled wave equation can be derived from Maxwell equations. In an ideal lossless medium, the three couple wave equations is given by:

$$\frac{dE_1}{dz} = \frac{i\omega_1}{cn_1} \chi^{(2)} E_3 E_2^* e^{-i\Delta k z} \quad (4.24)$$

$$\frac{dE_2}{dz} = \frac{i\omega_2}{cn_2} \chi^{(2)} E_3 E_1^* e^{-i\Delta k z} \quad (4.25)$$

$$\frac{dE_3}{dz} = \frac{i\omega_3}{cn_3} \chi^{(2)} E_1 E_2 e^{i\Delta k z} \quad (4.26)$$

where $n_{1,2,3}$ are the linear index of refraction and $\Delta k = k_1 + k_2 - k_3$ is the wave vector mismatch. Using different initial conditions to solve these coupled wave equations,

we can get the wave evolution functions for different nonlinear process. Details of the calculations can be found in [66]. Next, I will talk about parametric amplification (same process as DFG) and spontaneous parametric down conversion, which are the two main interaction in our experiment.

Parametric amplification

Parametric amplification happens when the pump field at frequency ω_3 and a probe beam with frequency ω_1 are interacted in a nonlinear medium. This process produces an output wave at the different frequency $\omega_2 = \Omega_3 - \Omega_1$, and at the same time the probe beam field will be amplified.

Consider a lossless nonlinear medium and assuming the pump beam is strong enough to neglect the depletion, the pump field E_3 can be taken as constant. For perfect phase matching, with the initial boundary condition $E_1(0)$ is arbitrary constant and $E_2(0) = 0$, the solutions to Eq. (4.24) is

$$E_1(z) = E_1(0)\cosh\kappa z, \quad (4.27)$$

$$E_2(z) = e^{i\phi} E_1^*(0)\sinh\kappa z, \quad (4.28)$$

where ϕ is the phase related to the pump field and κ is the coupling constant proportional to χ and E_3 , z is the interaction distance. We define the squeezing parameter $r = \kappa z$. For the degenerated case when $\omega_1 = \omega_2$, we get the total output field of the probe beam has a general solution of the form

$$E(z) = E_1(0)\cosh r + e^{i\phi} E_1^*(0)\sinh r. \quad (4.29)$$

Therefore, probe beam power

$$P = |E(z)|^2 = |E_1(0)|^2(\cosh^2 r + \sinh^2 r) + |E_1(0)|^2 \sinh 2r \cos \phi. \quad (4.30)$$

When $\phi = 0$, the probe beam power is amplifier to the maximum value

$$P_{max} = |E_1(0)|^2(\cosh r + \sinh r)^2 = |E_1(0)|^2 e^{2r}, \quad (4.31)$$

with the parametric amplification gain

$$G_{max} = e^{2r}. \quad (4.32)$$

Spontaneous parametric down conversion

Spontaneous parametric down conversion (SPDC) happens when there is only pump field ω_3 inserted into the nonlinear medium. It occurs by the amplification of noise photons generated by fluorescence. The initial conditions of SPDC is $E_1(0) = E_2(0) = 0$ and the Eq. (4.24) do not have solutions. This process can only be describe by quantizing the field as shown in Section 2.1.

SPDC is a process that a pump photon of frequency ω_3 is annihilated while a signal photon at ω_1 and an idler photon ω_2 are created. The Hamiltonian of SPDC then can be written as

$$H = H_0 + H_I = \sum_{i=1,2,3} \hbar \omega_i (a_i^\dagger a_i + \frac{1}{2}) + i\hbar \frac{\chi}{2} (a_3 a_1^\dagger a_2^\dagger - a_3^\dagger a_1 a_2), \quad (4.33)$$

where the first term H_0 is the free field evolution and H_I is the interaction of three fields. With negligible pump depletion, the pump field is treated as classical field,

which is a coherent state shown in Section 2.3.2. With $a_3 \rightarrow \beta$, the interaction Hamiltonian is given by

$$H_I = i\hbar \frac{\chi}{2} (\beta a_1^\dagger a_2^\dagger - \beta^* a_1 a_2). \quad (4.34)$$

The evolution equation in interaction pictures for the annihilation and creation operators are

$$\begin{aligned} \frac{da_1}{dt} &= \kappa a_2^\dagger, \\ \frac{da_1^\dagger}{dt} &= \kappa^* a_2, \\ \frac{da_2}{dt} &= \kappa a_1^\dagger, \\ \frac{da_2^\dagger}{dt} &= \kappa^* a_1, \end{aligned} \quad (4.35)$$

where $\kappa = \chi\beta$. Solving these evolution equations, we get the Bogoliubov transformation

$$a_1(t) = a_1(0) \cosh r + a_2^\dagger(0) \sinh r, \quad (4.36)$$

$$a_1^\dagger(t) = a_1^\dagger(0) \cosh r + a_2(0) \sinh r, \quad (4.37)$$

$$a_2(t) = a_2(0) \cosh r + a_1^\dagger(0) \sinh r, \quad (4.38)$$

$$a_2^\dagger(t) = a_2^\dagger(0) \cosh r + a_1(0) \sinh r, \quad (4.39)$$

where $r = \kappa t$ is what we called the squeezing parameter and t is the nonlinear interaction time. Compared to Previous section, this is two-mode squeezed state.

When $\omega_1 = \omega_2$, it is the degenerated case, single-mode squeezed state

$$a_1(t) = a_1(0) \cosh r + a_1^\dagger(0) \sinh r, \quad (4.40)$$

$$a_1^\dagger(t) = a_1^\dagger(0) \cosh r + a_1(0) \sinh r. \quad (4.41)$$

4.1.3 4-mirror OPO used in the experiment

The OPO setup in this experiment is shown in Fig. 4.5. It consists of a four-mirror bow-tie cavity and a periodically-poled KTiOPO_4 (KTP) crystal (PPKTP).

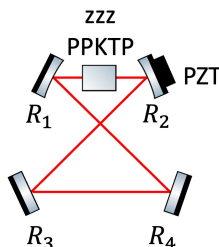


Figure 4.5: Optical parametric oscillator consists of 4-mirror bow-tie cavity and a nonlinear crystal PPKTP.

The four-mirror bow-tie cavity has two concave mirrors (R_1 , R_2) and two flat mirrors (R_3 , R_4). The mirrors are all fabricated by Advanced Thin Films. The two concave mirrors have 50 mm radius. Mirrors R_1 , R_2 and R_3 have near-zero transmittance at 1064 nm and near-unity transmittance at 532 nm. The output coupler R_4 has 17% transmittance at 1064 nm and less than 0.01% transmittance at 532 nm. This cavity has FSR at about 1 GHz. For 1064 nm light, the cavity linewidth is 36 MHz. This cavity has two beam waists. One beam waist is $135 \mu\text{m}$ at the middle between mirror R_3 and R_4 . The other beam waist is $35 \mu\text{m}$ located at the middle between mirror R_1 and R_2 , where the PPKTP nonlinear crystal is placed.

The PPKTP crystal provided by Raicol, Inc. is x-cut with size $1 \times 2 \times 10 \text{ mm}^3$. The poling period is $9 \mu\text{m}$ at room temperature. It is a zzz crystal which makes the pump, signal and idler beam are all in z-polarization. The crystal is anti-reflection coated by Advanced Thin Films both at 1064 nm and 532 nm. The temperature of crystal is stabilized to few tenths of a millidegree by servo loops to reach the maximum quasi-phase matching bandwidth of 3.18 THz, the details of which can be found in

[68, 69].

Quantum optical frequency comb

This OPO is pumped by 532 nm laser light. Its power is 550 mW, below the OPO lasing threshold. The parametric down conversion process happens in the PPKTP crystal and the pump photons are converted to idler and signal photons, the spectrum of which is continuous over the quasi phase matching bandwidth (3.2 THz). The two down-converted photons are correlated and form a two-mode squeezed state. However, only the light of the OPO resonant frequencies can be build up and emitted out of OPO. The emission spectrum of OPO is a quantum optical frequency comb as shown in Fig.4.6. The green arrow denotes the half of the pump frequency. The red dashed lines connect the two-mode squeezing mode pairs. Therefore, a QOFC consist of a larger number of two-mode squeezing pairs that are equally distributed around the half of pump frequency.

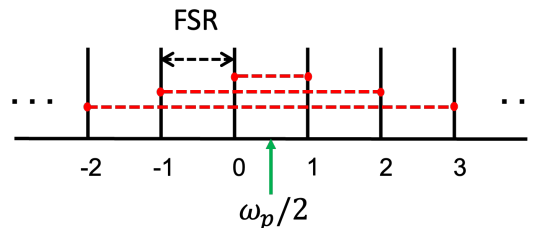


Figure 4.6: Quantum optical frequency comb.

4.2 Pound-Drever-Hall (PDH) locking

4.2.1 PDH locking principles

Pound-Drever-Hall (PDH) technique is a powerful approach for stabilizing the frequency of the laser by locking to a stable cavity. It can also be used the other way to lock an optical cavity so that the resonant frequency follows a specific laser. PDH locking was first proposed by R. W. P. Drever et al. in 1983 [70] and the detailed calculation can be found in [71]. See also [72] for simple fundamentals of FM spectroscopy. Here I will briefly introduce the principles.

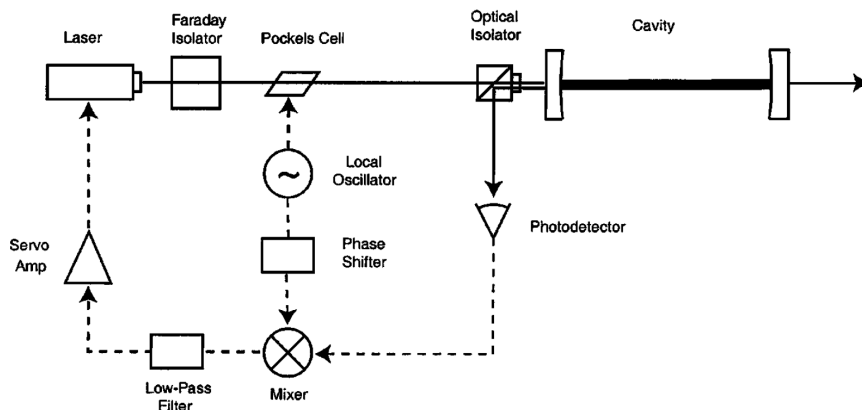


Figure 4.7: The basic layout for PDH locking. Solid lines are optical paths and dashed lines are signal paths. The signal going to the laser controls its frequency [71].

A basic setup of PDH locking is shown in Fig.4.7. A laser emits light with single frequency ω . After going through the Pockels cell, the light is phase modulated at frequency Ω and the electric field is

$$E_i = E_0 e^{i(\omega t + \beta \sin \Omega t)}, \quad (4.42)$$

where β is the modulation depth. With small β , we have the approximation

$$E_i \approx E_0 [J_0(\beta)e^{i\omega t} + J_1(\beta)e^{i(\omega+\Omega)t} - J_1(\beta)e^{i(\omega-\Omega)t}], \quad (4.43)$$

where J_n is the Bessel function of the first kind. The light is reflected by a cavity with the reflection coefficient $R(\omega)$ Eq. (4.13). The reflected light field is

$$E_r = E_0 [R(\omega)J_0(\beta)e^{i\omega t} + R(\omega + \Omega)J_1(\beta)e^{i(\omega+\Omega)t} - R(\omega - \Omega)J_1(\beta)e^{i(\omega-\Omega)t}]. \quad (4.44)$$

The photodetector measures the reflected light power $P_r = |E_r|^2$. We ignore the DC part and 2Ω terms in the expression. The Ω term include the phase of the reflected beam is

$$P_r = 2J_0J_1P_0 \{ \text{Re} [A] \cos\Omega t + \text{Im} [A] \sin\Omega t \}, \quad (4.45)$$

where $A = R(\omega)R^*(\omega + \Omega) - R^*(\omega)R(\omega - \Omega)$.

Now consider two cases: first, the modulation frequency is small compared to the linewidth, so that we have the approximation

$$R^*(\omega + \Omega) \approx R^*(\omega) + \frac{d}{d\omega}R^*(\omega)\Omega \quad (4.46)$$

$$R(\omega - \Omega) \approx R(\omega) - \frac{d}{d\omega}R(\omega)\Omega. \quad (4.47)$$

So, A becomes pure real number

$$A \approx 2\text{Re} \left\{ R(\omega) \frac{d}{d\omega} R^*(\omega) \right\} \Omega \approx \frac{d|R|^2}{d\omega} \Omega. \quad (4.48)$$

The reflected power is

$$P_r = (\text{constant}) + 2J_0(\beta)J_1(\beta)P_0 \frac{d|R|^2}{d\omega} \Omega \cos\Omega t + (2\Omega \text{terms}), \quad (4.49)$$

with the approximation $J_0(\beta) \approx 1$, $J_1(\beta) \approx \frac{\beta}{2}$ and $P_0 = E_0^2$. This reflected signal mixed with $\cos\Omega t$ and with a low pass filter to keep only the DC terms, we have the PDH error signal

$$\epsilon = \beta P_0 \frac{d|R|^2}{d\omega} \Omega. \quad (4.50)$$

With the expression of reflection coefficient Eq. (4.13), we can plot the error signal for small modulation frequency Ω as Fig.4.8 (a).

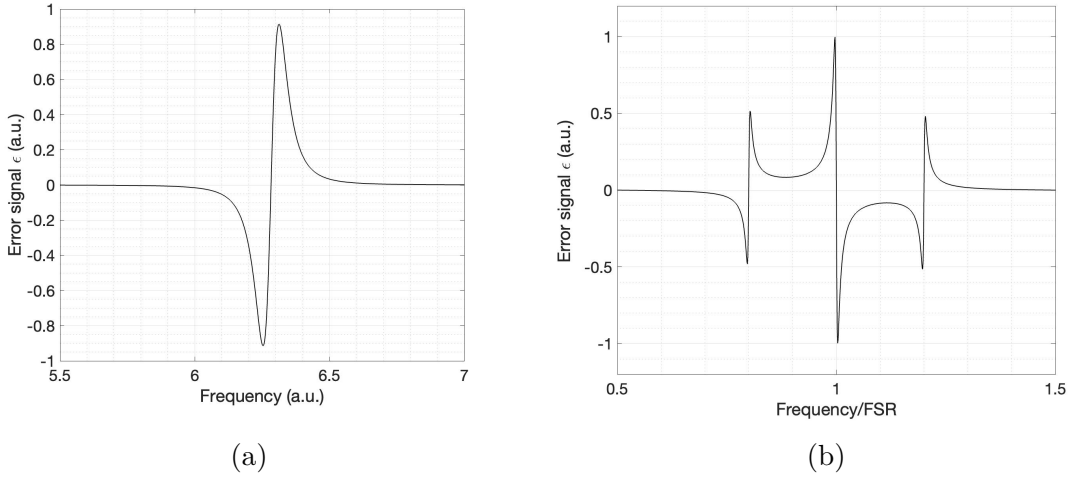


Figure 4.8: PDH error signal when (a) modulation frequency Ω is small ($\Omega \approx \text{half of linewidth}$), (b) Modulation frequency is large ($\Omega = 20 \text{ linewidth}$).

Second, the modulation frequency is large compared to linewidth. Under this condition, the sidebands are totally reflected $R(\omega \pm \Omega) \approx -1$. Then A becomes pure imaginary:

$$A \approx -2i\text{Im}\{R(\omega)\}. \quad (4.51)$$

The cosine terms in Eq. (4.45) are negligible. After the mixer and low pass filter, the error signal is given by the coefficient of sine term

$$\epsilon = -4\beta P_0 \text{Im} \{R(\omega)\} \quad (4.52)$$

The plot for this error signal is shown in Fig.4.8 (b).

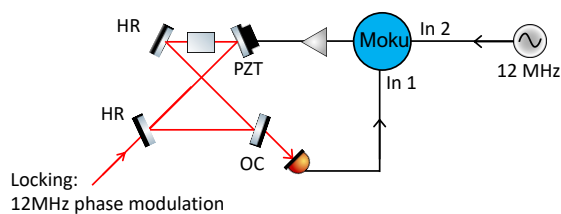
4.2.2 PDH locking setup

In the experiment, a problem with OPO locking was the long-term stability. We observed that the OPO cavity length drifted slowly because of the reasons such as temperature drifting. When the cavity length drifted out of the feedback signal correction range. The OPO went off lock. With this issue, the OPO could only stay locked for one minute. To solve this problem, we used the laser lock box instrument in Moku:Lab to separate the PDH error signal into two channels, the fast control and the slow control. The slow control channel separates the low frequency components of the error signal and sends them to a 0-340V high-voltage channel which can follow the large drift excursion for a longer time. The fast frequency components are sent to the previously used regular $\pm 10\text{V}$ channel. to be amplified more. So that the feedback control signal applied to the PZT mounted on the OPO mirror has larger amplitude at low frequency to correct the long term drifting better. In the experiment, a problem with OPO locking was the long-term stability. We observed that the OPO cavity length drifted slowly because of the reasons such as temperature drifting. When the cavity length drifted out of the feedback signal correction range. The OPO went off lock. With this issue, the OPO could only stay locked for one minute. To solve this

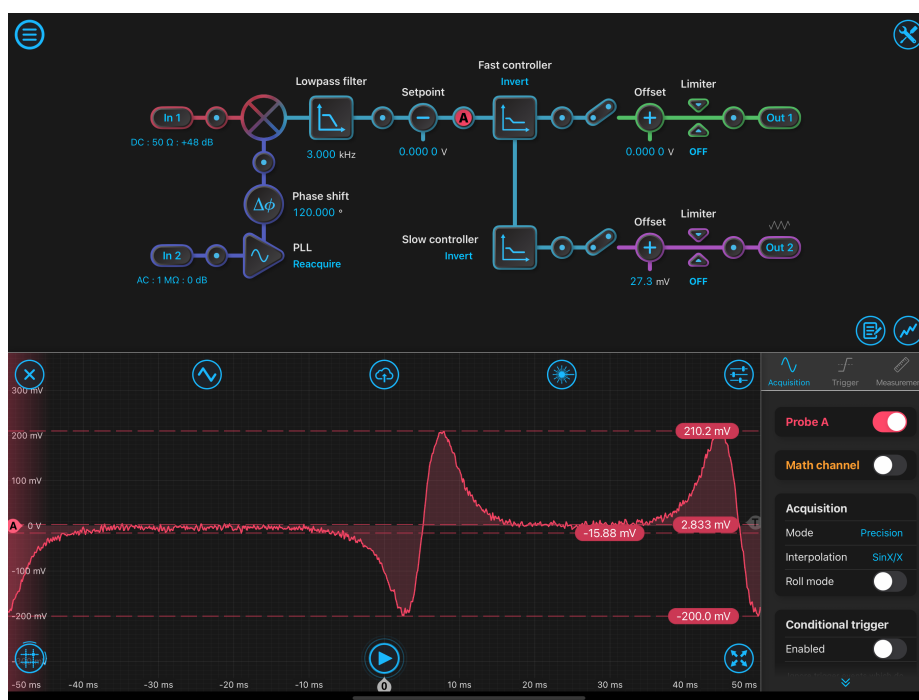
problem, we used the laser lock box instrument in Moku:Lab to separate the PDH error signal into two channels, the fast control and the slow control. The slow control channel separated the low frequency components of the error signal and sent them to a 0-340V high-voltage channel which can follow the large drift excursion for a longer time. The fast frequency components were sent to the previously used regular $\pm 10V$ channel.

The PDH locking setup is shown in Fig.4.9 (a). The locking beam is injected on the HR mirror and a photodetector detects the transmitted light from the output coupler. The transmitted light signal connects to Moku:Lab input 1. The laser itself has a 12 MHz phase modulation on the locking beam. This 12 MHz signal is connected to Moku:Lab input 2. A 12 MHz signal that is phase locked to input 2 is generated by Moku:Lab to mix with the signal from input 1. After a low pass filter, the error signal is separated into two channels: fast control and slow control. The fast control channel amplifies the signal up to 1.5 kHz and the slow control channel amplifies the frequency smaller than 500 mHz.

One limit of the Moku:Lab is the output feedback signal has the maximum value of 1 V. So the fast and slow control signals are further amplified before sent to the PZT mounted on the OPO mirror. The fast control signal amplitude is amplified to 20 times by Vescent D125 laser servo proportional gain, and then sent to the lab built PZT controller modulation channel, which has the gain of 1. The slow control signal is sent to the ramp channel of the same PZT controller, which amplifies the slow control signal by 35 times. Then the fast control signal from the modulation channel and the slow control signal from the ramp channel are added together and applied to the PZT mounted on one of the OPO mirror. The separation of fast and slow control signal is needed because the ramp channel has only 1 kHz bandwidth so that



(a)



(b)

Figure 4.9: (a) The experimental setup of OPO PDH locking. (b) Moku:Lab control panel. Upper part is the electronic scheme including mixer, low pass filter, fast and slow controller. Lower part is the PDH locking error signal.

it can only amplify the small control signal with frequency smaller than its bandwidth. Compared to the old setup where all the feedback signal with a bandwidth of 3 kHz only went through the modulation channel without amplification, the new setup with small frequency feedback signal being amplified more makes the PZT on the OPO mirror has longer tuning range. Therefore we observe that the OPO can stay locked longer with slow drifting being better corrected.

Before locking, there is a triangle wave scan generated from output 2. With this ramp, we got the error signal in Fig.4.9 (b) and the corresponding signal to noise ratio is

$$\text{SNR} = \frac{2\sqrt{2}V_{pp}}{V_{noise}} = 62.4, \quad (4.53)$$

where V_{pp} is the peak-to-peak value of PDH locking error signal and V_{noise} is the peak-to-peak value of the noise in PDH locking error signal. With this slow control correcting the low frequency drifting, the OPO can stay locked for 30 minutes before the PZT reaching the length limits.

4.3 Pump and probe phase locking

In order to monitor the QOFC phase, we inserted a probe beam into the OPO in the same propagating direction as the quantum light. As shown in previous section, there is three-wave mixing effect among the pump beam, probe beam and quantum light. The parametric down conversion generates the quantum light and the phase satisfies $\phi_P - 2\phi_q = 0$, where ϕ_p is the pump phase and ϕ_q is the quantum light phase. However the parametric down conversion starts from vacuum and there is no

quantum light at the beginning which mean ϕ_q is defined only by ϕ_p . Therefore, to get stable QOFC phase, the pump phase must be locked.

On the other hand, when the probe beam and pump beam phase satisfy $\phi_p - 2\phi_r = 0$, where ϕ_r is the probe beam phase, parametric amplification makes the probe beam power maximum as shown in Eq. (4.31). Therefore, if the pump phase is locked to the probe beam phase to make $\phi_p - 2\phi_r = 0$, we can get stable quantum light phase, which is the same as the probe beam phase.

In this section, I will first give theoretical calculations of getting error signal of locking pump phase from the power of probe beam. Then I will show the design of the circuit to get the probe beam power information using balanced homodyne detector. Finally, I will present the pump-probe beam phase locking setup and results.

4.3.1 Theoretical calculation

I will show the derivation of pump-probe phase locking error signal in this section.

By scanning the PZT mounted on a mirror with a sinusoidal RF signal, the pump light path is changed so that the pump phase becomes

$$\phi = \phi_0 + m\sin(\Omega t + \theta), \quad (4.54)$$

where ϕ_0 is the initial phase of the pump, m is the modulation depth, Ω is the modulation frequency and θ is the initial phase of the RF signal. Assume m is small, from Section 4.1.2, in the parametric process, the probe beam power shown in

Eq. (4.30) becomes

$$\begin{aligned}
P &= |E_1(0)|^2(\cosh^2 r + \sinh^2 r) + |E_1(0)|^2 \sinh 2r \cos \phi \\
&= |E_1(0)|^2(\cosh^2 r + \sinh^2 r) + |E_1(0)|^2 \sinh 2r \cos [\phi_0 + m \sin(\Omega t + \theta)] \\
&= |E_1(0)|^2(\cosh^2 r + \sinh^2 r) \\
&\quad + |E_1(0)|^2 \sinh 2r \{ \cos(\phi_0) \cos [m \sin(\Omega t + \theta)] - \sin(\phi_0) \sin [m \sin(\Omega t + \theta)] \} \quad (4.55) \\
&\approx |E_1(0)|^2(\cosh^2 r + \sinh^2 r) \\
&\quad + |E_1(0)|^2 \sinh 2r \{ \cos(\phi_0) - \sin(\phi_0) [m \sin(\Omega t + \theta)] \} \\
&= P_0(\cosh 2r + \sinh 2r \cos \phi_0) - m P_0 \sinh 2r \sin \phi_0 \sin(\Omega t + \theta),
\end{aligned}$$

where $P_0 = |E_1(0)|^2$ is the initial power of probe beam. Using a high-pass filter to get the AC term and mixing it with RF wave $\sin(\Omega t + \delta)$:

$$\begin{aligned}
& m P_0 \sinh 2r \sin \phi_0 \sin(\Omega t + \theta) \times \sin(\Omega t + \delta) \\
&= \frac{1}{2} m P_0 \sinh 2r \sin \phi_0 \cos(\theta - \delta) + (2\Omega \text{ term}), \quad (4.56)
\end{aligned}$$

with the 2Ω term filtered out and the RF signal initial phase difference $\theta - \delta = 0$, the error signal of the pump-probe phase lock is

$$\epsilon = \frac{1}{2} m P_0 \sinh 2r \sin \phi_0. \quad (4.57)$$

By scanning the pump phase ϕ_0 with a 10 Hz ramp signal, we can get a sinusoidal error signal. The locking point is $\epsilon = 0$, which mean ϕ can be both 0 or π , corresponding to amplification and deamplification. This can be checked by monitoring the probe beam power to make sure probe beam power is locked at the maximum.

4.3.2 Circuit design

To perform the pump-probe beam phase lock, it is important to detect the power of the probe beam. Previously, we used balanced homodyne detector which subtracts the photon current and cannot give the information of the power that each photodiode detects. Based on the balanced homodyne detector circuit, we designed a supplementary circuit to detect the probe beam power.

The circuit is shown in Fig.4.10. The first part in the blue rectangular frame is the balanced homodyne circuit. Two photodiodes that are -5 V biased produce the photo current I_1 and I_2 . A capacitor selects the AC component of the photon current difference and a transimpedance amplifier converts the current to AC output voltage

$$V_{out} = I_{in}R, \quad (4.58)$$

where R is the feedback resistor for the op-amp OPA686. An inductor filters the DC component of the photon current and an op-amp (OPA27) voltage buffer output the DC voltage

$$V_{out} = V_{in}. \quad (4.59)$$

The supplementary part in the red frame is used to extract the single PD photon current, which is proportional to the probe beam power. The photon current I_2 is sent to a transimpedance amplifier and converted to a voltage signal. The op-amp used here is OPA686, powered by ± 12 V voltage resource. The positive input of the op-amp is connected to -5 V voltage source, which makes sure the PD is still properly biased.

The single PD output signal of the probe beam power is shown in Fig. 4.11

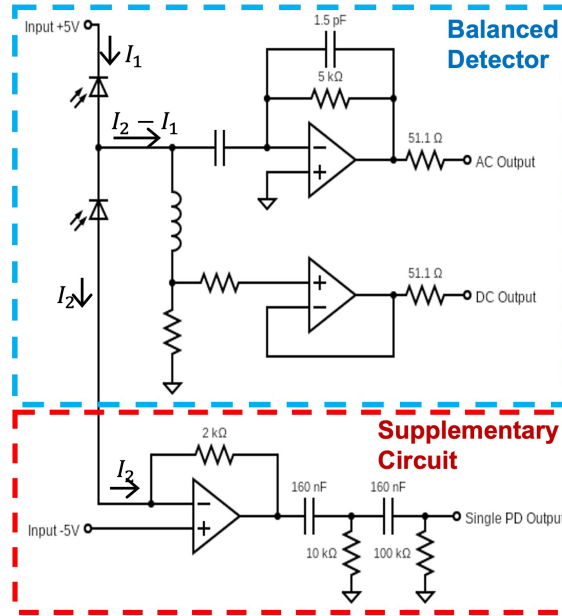


Figure 4.10: Detector circuit design. The AC and DC outputs are used for balanced homodyne detection. The single PD output signal gives the power of probe beam.

(without the second order high pass filter shown in Fig.4.10). When there is no light, the output voltage is -5.012 V which is the bias voltage of the PD. With light shining on the PD, the output voltage absolute value increases and the voltage difference represent the light power detected by single PD. When scanning the pump at 200 Hz, the probe beam power changes with a period of 5.00 ms. The probe beam power, without pump, shining on single PD is $17 \mu\text{W}$ with the output voltage increased by 24.8 mV. When parametric amplification condition was satisfied, the probe beam power is amplified and the voltage absolute value increased by 96.9 mV. The parametric gain is 3.91 . Using Eq. (4.32), the squeezing parameter $r = 0.681$, corresponding to -5.92 dB of squeezing.

To get rid of the DC biased voltage of the single PD output signal, a second order high pass filter is added to the output port. The second order high pass filter is built by cascading two first order high pass filter with resistors and capacitors set to be



Figure 4.11: Probe beam power changes with the pump phase scanning.

$R_1 = 10k\Omega$, $C_1=160$ nF and $R_2 = 100k\Omega$, $C_2=16$ nF. The cut off frequency of this second order high pass filter is

$$f = \frac{1}{2\pi R_1 C_1 R_2 C_2} = \frac{1}{2\pi R_2 C_2} = 99.47Hz. \quad (4.60)$$

The slope of this filter is -40 dB/decade.

4.3.3 Experimental setup and locking results

The schematic setup for pump-probe beam phase locking is shown in Fig.4.12. The pump phase is modulated by a 3 kHz RF signal generated by Moku:Lab, by applying to a PZT to changing the pump path length. The single PD output signal went through a band pass filter to get this 3 kHz signal which is sent to Moku:Lab input 1. After mixing with 3 kHz RF signal, the error signal is separated into fast and slow control channels. The fast control amplifies the signal up to 200 kHz and the slow control amplifies the signal smaller than 5 Hz.

When performing pump phase locking in the experiment, the single PD output

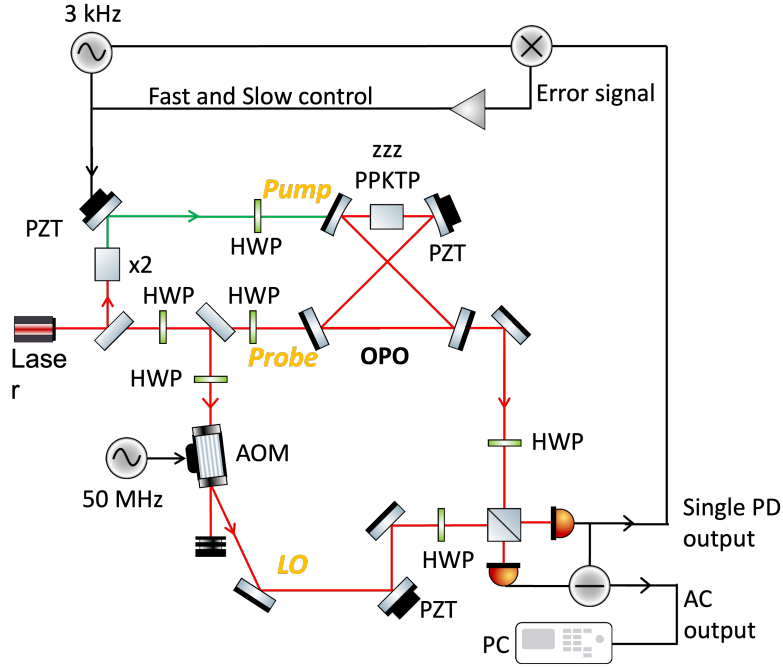


Figure 4.12: Pump-probe beam phase lock set up.

signal is the beat signal between the probe beam and LO. LO frequency is shifted 50 MHz from probe beam frequency. The signal detected by the PD is

$$\begin{aligned}
 & |E_{probe} + E_{LO}|^2 \\
 &= |E_1 e^{i\omega_1 t + \phi_1} + E_2 e^{i\omega_2 t + \phi_2}|^2 \\
 &= |E_1|^2 + |E_2|^2 + 2 |E_1 E_2| \cos(\Delta\omega t + \Delta\phi),
 \end{aligned} \tag{4.61}$$

where $\Delta\omega = \omega_1 - \omega_2 = 50$ MHz and $\Delta\phi = \phi_1 - \phi_2$. Therefore, the beat signal amplitude is proportional to the probe beam field amplitude. Fig.4.13 shows the locking result by measuring the beat signal amplitude with LO power remains constant. Without the pump phase locking, as shown by the red line, the beat signal amplitude kept drifting. When the pump phase is locked, the beat signal amplitude stays at the maximum value as shown by the blue line, which is a proof that the probe beam power is locked to its maximum.

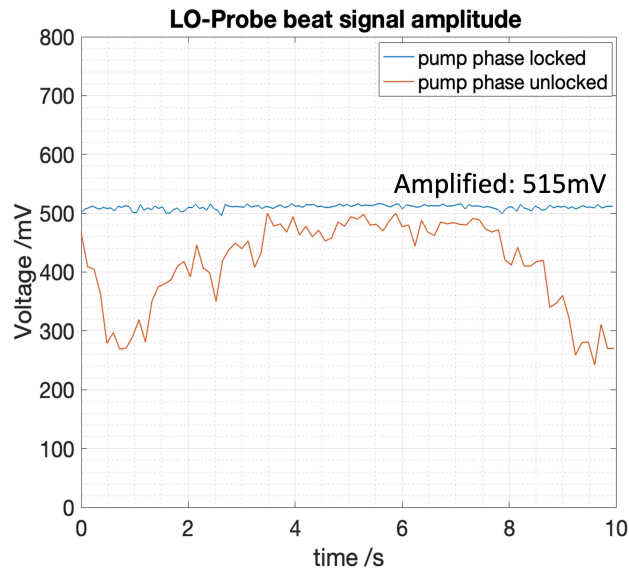


Figure 4.13: Probe beam and LO beat signal amplitude measured with and without pump phase locking.

So, for now, it has been shown that the amplitude of 50 MHz beat signal between probe beam and LO is stabilized by locking the pump phase to probe beam. In the next section, I will present the stabilization of this beat signal phase by locking the LO phase to probe beam.

4.4 Local oscillator and probe phase locking

We can derive the LO and probe beam phase lock error signal from Eq.4.61. This beat signal is mixed with a 50 MHz RF signal

$$\begin{aligned}
 & 2 |E_1 E_2| \cos(\Delta\omega t + \Delta\phi) \times \cos(\Delta\omega t + \theta) \\
 & = 2 |E_1 E_2| [\cos(2\Delta\omega t + \Delta\phi + \theta) + \cos(\Delta\phi - \theta)],
 \end{aligned} \tag{4.62}$$

where $\Delta\omega = 50\text{MHz}$, $\Delta\phi$ is the initial phase difference between LO and probe beam, θ is the initial phase of RF signal. After the low pass filter, we get the error signal

$$\epsilon = 2 |E_1 E_2| \cos(\Delta\phi - \theta). \quad (4.63)$$

The locking point is when $\epsilon = 0$, which means $\Delta\phi - \theta = n\pi/2$. This works because the relative phase between LO and probe beam needs to be stable and we don't need to know the exact LO phase value. So, the LO phase can be locked to any value.

Fig.4.14 shows the schematic setup of LO probe beam phase lock. The LO and probe beam are linearly polarized in perpendicular direction and mixed by a polarized beam splitter (PBS). A half wave plate (HWP) rotates their polarizations by 45° and then a PBS is used to mixed then so that both output port of PBS have LO beating with probe beam, which are detected by two photodiodes. The subtraction of two photo currents gives only AC signal, which is sent to input one of Moku:Lab laser lock instrument and mixed with a 50 MHz RF signal to generate the error signal. This error signal is shown in Fig.4.15.

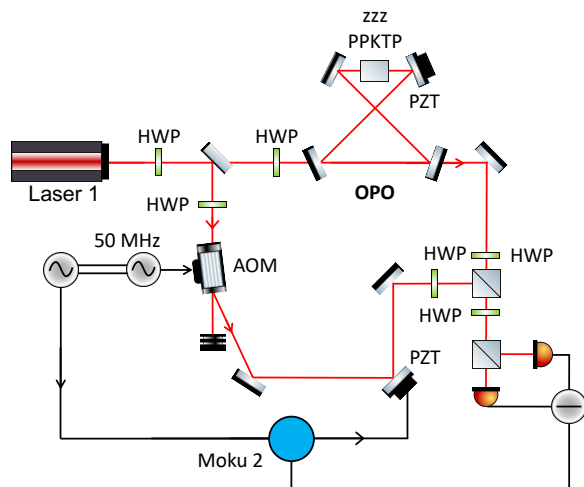


Figure 4.14: LO and probe beam phase lock experimental setup.

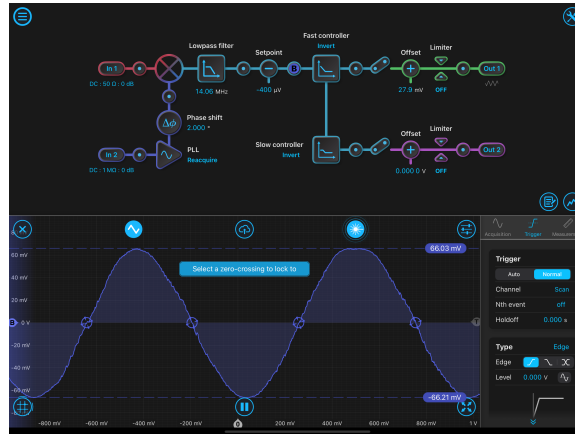


Figure 4.15: LO and probe beam phase lock error signal.

With LO probe beam phase locked, the phase of the 50 MHz beat note is stabilized. The meaning of this AC signal phase stabilization is confusing since the phase at different time is not constant because of the $\Delta\omega t$ evolution in the phase term. However, the locking of this relative phase can give us the same phase when it is measured at time interval equal to multiples of the period $T = 1/\Delta\omega$. This is proved with the results showing in Section 5.4.

Chapter 5

Quadrature measurement by homodyne/heterodyne detection

To measure cluster states, it is important to get the quadrature (P and Q) information. One way to measure the cluster state is to measure its nullifiers by homodyne detection, like the previous experiment of generating 60-mode cluster state [3]. Here we need to clarify the meanings of homodyne and heterodyne detection. In the classical context of radio/optical measurements, a homodyne measurement refers to an interferometric signal between the measured field and a calibrated local oscillator (LO) *of the same frequency*, while a heterodyne measurement refers to the beat note of the measured field with a frequency-shifted LO. In quantum optics, the latter case yields undesirable contamination of the signal by “image-band” vacuum field modes placed spectrally outside the signal and LO fields, at the same frequency spacing as the beat frequency [73]. It is crucial for quadrature measurements (and for any quantum optical measurement) to ensure that no such contamination by vacuum modes of the quantum electromagnetic field occur. This can be ensured in different ways: *(i)*, by having the LO exactly at the same frequency as the modes to be measured, i.e., by frequency-homodyne detection, or *(ii)*, in a two-mode measurement, by having the LO frequency exactly halfway between the two modes. This is how the first-ever squeezing measurement was made [74] and, even though it was a frequency-heterodyne

measurement of a 482 MHz beat note, it was nonetheless termed a (quantum-) homodyne measurement, because negligible vacuum contamination was present. We will, from now on, use the terms homodyne and heterodyne in the quantum context, meaning, respectively, with and without vacuum contamination. The former will comprise both frequency-homodyne and frequency-heterodyne configurations, while the latter will only comprise frequency-heterodyne configurations.

Here, we want to go beyond nullifier measurements and reconstruct the whole covariance matrix, Eq. (A.9), in order to access the whole graph state, including errors, i.e., $\mathbf{Z}=\mathbf{V}+i\mathbf{U}$ rather than just \mathbf{V} . While quantum homodyne measurements can be used to reconstruct nullifiers, which I will present in Section 5.3, they cannot reconstruct the complete set of quantum correlations of the covariance matrix because quantum homodyne measurements suffer from fundamental limits due to their symmetric field configuration [75]. For this reason, I have designed and implemented a quantum heterodyne measurement scheme that will be presented in Section 5.4.

Frequency-heterodyne detection combined with Fourier transformation provide a compact method to measure large scale multimode cluster state. In this chapter, I discuss the principles of this method and present some preliminary results of measuring the two-mode squeezed state based on the experimental setup in chapter 4.

5.1 Fourier transform and sampling

5.1.1 Fourier transform basics

Fourier transform is a method that express a function by a sum of waves with different frequencies, amplitudes and phases. It is used to convert the signal acquired in time

domain to frequency domain so that a complex number associated with each frequency mode can be calculated.

For an arbitrary one dimensional function in time domain $f(t)$, Fourier transform function at frequency ν is given by

$$F(\nu) = \int_{-\infty}^{\infty} f(t)e^{-i2\pi\nu t} dt. \quad (5.1)$$

$f(t)$ can also be represented as a recombination of complex exponentials of all possible frequencies, which is the Fourier inversion integral is

$$f(t) = \int_{-\infty}^{\infty} F(\nu)e^{i2\pi\nu t} d\nu. \quad (5.2)$$

The Fourier transform provides information on the sinusoidal components of a signal because

$$e^{i2\pi\nu t} = \cos(2\pi\nu t) + i\sin(2\pi\nu t). \quad (5.3)$$

For real valued $f(t)$ and positive t , Eq. (5.2) becomes

$$\begin{aligned} f(t) &= 2 \int_0^{\infty} \text{Re} [F(\nu)e^{i2\pi\nu t}] d\nu \\ &= 2 \int_0^{\infty} \{ \text{Re} [F(\nu)] \cos(2\pi\nu t) - \text{Im} [F(\nu)] \sin(2\pi\nu t) \} d\nu, \end{aligned} \quad (5.4)$$

where the complex Fourier coefficients $F(\nu) = F_R(\nu) + iF_I(\nu)$, with its magnitude and phase:

$$|F(\nu)| = \sqrt{F_R(\nu)^2 + F_I(\nu)^2}, \quad (5.5)$$

$$\phi = \tan^{-1} \frac{F_I(\nu)}{F_R(\nu)}. \quad (5.6)$$

This complex coefficients are related to the amplitude and phase quadrature when doing heterodyne measurement which will be discussed in details later.

Convolution theorem

The convolution of two functions $f(t)$ and $h(t)$ is defined as

$$f(t) * h(t) = \int_{-\infty}^{\infty} f(\nu)h(t - \nu)d\nu. \quad (5.7)$$

The convolution theorem is that the Fourier transform of a convolution of two functions is the point-wise multiplication of their Fourier transforms

$$\mathbf{F} [f(t) * g(t)] = \mathbf{F} [f(t)] \cdot \mathbf{F} [g(t)]. \quad (5.8)$$

It can be proved that the Fourier transform of the product of two functions equals to the convolution of the Fourier transforms of individual function, which is shown in the following equation

$$\mathbf{F} [f(t) \cdot g(t)] = \mathbf{F} [f(t)] * \mathbf{F} [g(t)]. \quad (5.9)$$

These mathematical properties are used in the data acquisition and sampling theorem, which will be discussed next.

5.1.2 Data acquisition

The signal generated in the experiment is continuous and can propagate for infinite long time. However, when we acquire the data, we can only take it as discrete points

within a finite time window. These are the problems that we need to consider when performing data sampling.

Sampling

Sampling is the process that transform continuous signals $f(t)$ into discrete signals, as shown in Fig.5.1 (a). The sampling function is

$$\delta_s(t, \Delta t) = \sum_n \delta(t - n \cdot \Delta t), \quad (5.10)$$

which is a comb function with Δt being the time interval between each discrete data points, n being an integer. $\delta(t)$ is the Dirac delta “function” which we take to be $\delta(t) = 1$ when $t = 0$, and $\delta(t) = 0$ for else. The sampling rate $F_s = 1/\Delta t$. The mathematical expression of sampling process is

$$f_s(t) = f(t) \cdot \delta_s(t, \Delta t) = \sum_n f(n\Delta t)\delta(t - n \cdot \Delta t), \quad (5.11)$$

where $f_s(t)$ is the sampled function. The Fourier transform of this sampled function is

$$\mathbf{F}[f_s(t)] = \mathbf{F}[f(t) \cdot \delta_s(t, \Delta t)] = \mathbf{F}[f(t)] * \mathbf{F}[\delta_s(t, \Delta t)], \quad (5.12)$$

where the Fourier transform of a comb function is still a comb function

$$\begin{aligned} \mathbf{F}[\delta_s(t, \Delta t)] &= \int_{-\infty}^{\infty} \sum_n \delta(t - n \cdot \Delta t) e^{-i2\pi\nu t} dt \\ &= \sum_n e^{-i2\pi\nu n\Delta t} \\ &= \frac{1}{\Delta t} \sum_n \delta\left(\nu - \frac{n}{\Delta t}\right). \end{aligned} \quad (5.13)$$

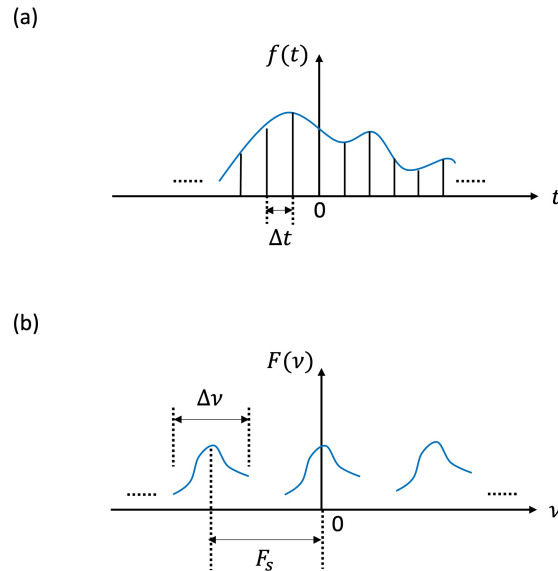


Figure 5.1: (a) Sampling a continuous function $f(t)$ using a comb function with sample interval Δt , sampling rate $F_s = 1/\Delta t$. (b) Frequency spectrum of sampled data. $\Delta\nu$ is the bandwidth of signal.

Thus, Eq. (5.12) becomes

$$\begin{aligned} \mathbf{F}[f_s(t)] &= \frac{1}{\Delta t} \sum_n \left[\delta(\nu - \frac{n}{\Delta t}) * F(\nu) \right] \\ &= \frac{1}{\Delta t} \sum_n F(\nu - \frac{n}{\Delta t}). \end{aligned} \quad (5.14)$$

This equation shows that the sampling in time domain replicates the signal spectrum in frequency domain as shown in Fig. 5.1 (b). In the replicated spectrum, the replication frequency period is $1/\Delta t = F_s$. If the signal $f(t)$ has a bandwidth of $\Delta\nu$, to avoid overlapping (aliasing), it must be satisfied that

$$F_s \gg \Delta\nu \quad (5.15)$$

Data acquisition time

Another fact that needs to be taken into account is the finite data acquisition time. Although the signal function can propagate for infinitely long time, we can only acquire data within a finite time ΔT , which is a window function

$$\Pi\left(\frac{t}{\Delta T}\right) = \begin{cases} 1 & \text{if } t \in \left[-\frac{\Delta T}{2}, \frac{\Delta T}{2}\right], \\ 0 & \text{otherwise.} \end{cases} \quad (5.16)$$

The sampled function within this time window becomes

$$G(t) = f(t) \cdot \delta_s(t, \Delta t) \cdot \Pi\left(\frac{t}{\Delta T}\right). \quad (5.17)$$

Fast Fourier transform (FFT) algorithm is based on the repetitive signal of $G(t)$ as shown in Fig.5.2 (a). This periodical signal has a Fourier series

$$f_{\Delta T}(t) = \sum_{n=-\infty}^{+\infty} D_n e^{i\omega_0 t}, \quad (5.18)$$

with the coefficient D_n being the Fourier transform of $f(t)$ in the expression of

$$\begin{aligned} D_n &= \frac{1}{\Delta T} \int_0^{\Delta T} f(t) e^{-in\omega_0 t} dt \\ &= \frac{1}{\Delta T} F(n\omega_0), \end{aligned} \quad (5.19)$$

where $\omega_0 = 2\pi\nu_0 = \frac{2\pi}{\Delta T}$. This means that the frequency spacing is the reciprocal of data acquisition time as shown in Fig.5.2 (b). For example, in the experiment, if we need to get the frequency separation of 10 kHz, data acquisition time needs to be longer than 0.1 ms.

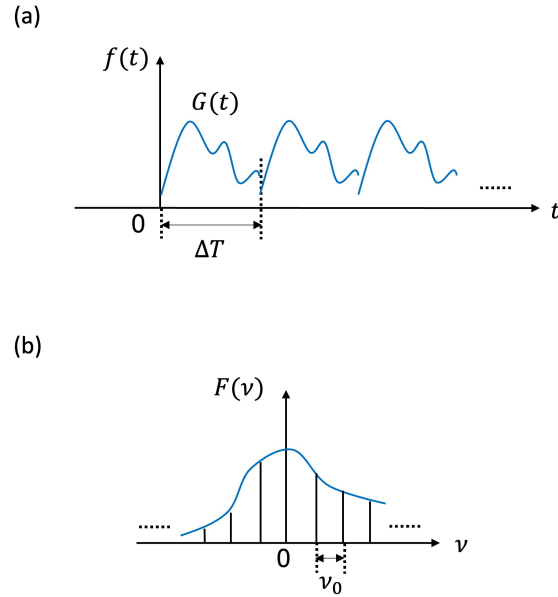


Figure 5.2: (a) Periodic signal generated based on finite data acquisition time ΔT . (b) Frequency domain data separation.

Intra-mode definition

In previous section, the cluster states are generated by phase modulated QOFC, the lines of which are OPO cavity modes. In our experiment, the FSR of the OPO is 1 GHz. If we are going to use the frequency heterodyne detection method, introduced in the next section Section 5.2, to measure the cluster state generated by the OPO modes, which has signal bandwidth of much larger than 1 GHz, the sampling rate needs to be larger than this signal bandwidth. However we have the data acquisition card used in this experiment that has the maximum sampling rate of 2 GHz. It could not be used to measure the cluster state generated by OPO modes here.

Considering the fact that each cavity mode has a linewidth of continuous spectrum in frequency domain, we can treat it as discrete intra-mode with frequency spacing $1/\Delta T$, where ΔT is the data acquisition time, as shown in Fig.5.3. Since the linewidth of our OPO was 10 MHz and then increased to 30 MHz, the signal bandwidth of

frequency heterodyne detection is around hundreds of MHz. Therefore, we measured only the intra-mode cases and the results are presented in this chapter.

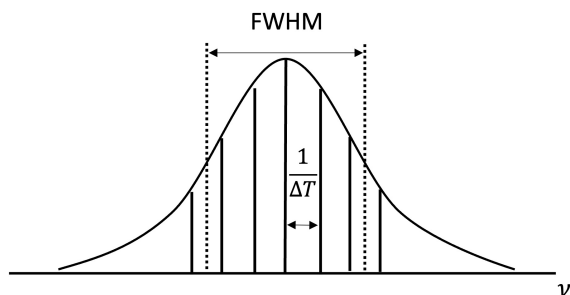


Figure 5.3: Intra-modes definition.

5.2 Quantum detection

5.2.1 Quantum-homodyne detection by balanced frequency-homodyne detection

One method to measure the nullifiers of cluster state is balanced homodyne detection. The general setup is shown in Fig.5.4. It consists of a 50:50 beam splitter (BS), the

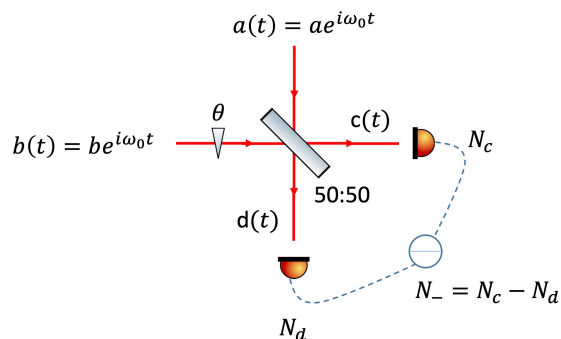


Figure 5.4: Balanced homodyne detection setup.

reflection and transmission coefficient of which are $r = t = \frac{1}{\sqrt{2}}$. The signal mode

$a(t) = ae^{i\omega_0 t}$ is incident on one of the BS input port. The local oscillator (LO) $b(t) = be^{i\omega_0 t}$, which in this case has the same frequency ω_0 as the signal mode, is incident on the other side of BS. Two photo diodes connected together are used to detect two output beam of the BS, $c(t)$ and $d(t)$, and their photocurrents are subtracted. Using the beam splitter matrix Eq. (2.80), we can get

$$c(t) = \frac{1}{\sqrt{2}}(a(t) + b(t)), \quad (5.20)$$

$$d(t) = \frac{1}{\sqrt{2}}(a(t) - b(t)). \quad (5.21)$$

So the photon numbers detected by the photo diodes are

$$N_c = c^\dagger(t)c(t) = \frac{1}{2}(a^\dagger a + b^\dagger b + a^\dagger b + b^\dagger a), \quad (5.22)$$

$$N_d = d^\dagger(t)d(t) = \frac{1}{2}(a^\dagger a + b^\dagger b - a^\dagger b - b^\dagger a). \quad (5.23)$$

Subtracting these two signals, the photon number difference N_- is

$$N_- = N_c - N_d = a^\dagger b + b^\dagger a. \quad (5.24)$$

Assuming the LO is a coherent state of light $b = |\beta| e^{i\theta}$ and inserting the definition of quadrature Q and P (Eq.2.9) for quantum signal, the photon number difference can be expressed as

$$\begin{aligned} N_- &= |\beta| (a^\dagger e^{i\theta} + a e^{-i\theta}) \\ &= \sqrt{2} |\beta| (Q \cos\theta + P \sin\theta). \end{aligned} \quad (5.25)$$

The photon number difference is amplified by the LO amplitude $|\beta|$, meanwhile the LO phase θ defines which quadrature of the target mode is measured: Q quadrature is measured when $\theta = n\pi$, and P quadrature is measured when $\theta = n\pi/2$, where n is

an integer. The LO phase can be scanned by adding a PZT mounted mirror to the LO light path to change its light path length.

5.2.2 Quantum-homodyne detection by balanced frequency-heterodyne detection

The general setup for balanced heterodyne detection is shown in Fig.5.5. Compared to the homodyne detection, balanced heterodyne detection also consists of a 50:50 BS, with the signal and LO being incident onto two sides of BS. However, the difference from homodyne detection is that the local oscillator used for heterodyne detection has a different frequency from the signal. An example is shown in Fig.5.5 (b): the frequency of LO is ω_0 , the signal consists of multiple frequencies $\omega_{\pm n} = \omega_0 \pm \Omega_n$.

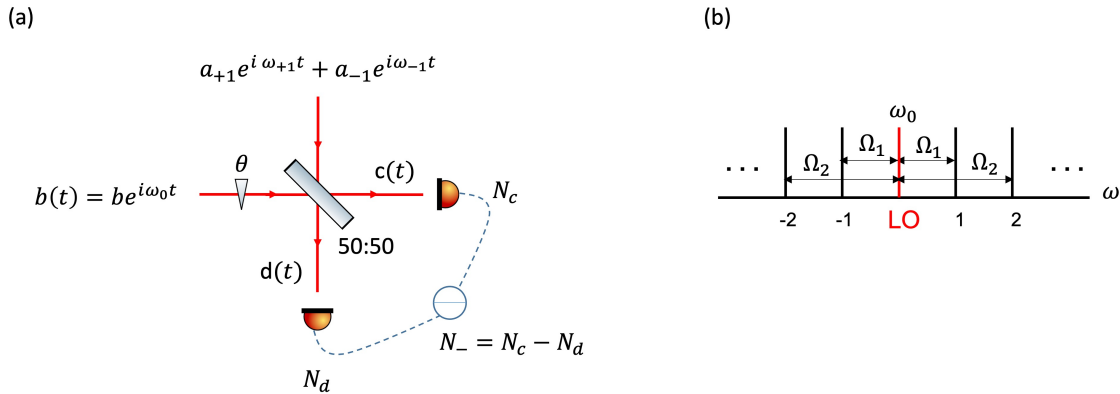


Figure 5.5: Balanced heterodyne detection (a) setup, and (b) frequency relation.

Taking Ω_1 as an example, the signal has two frequencies $\omega_{\pm 1} = \omega_0 \pm \Omega_1$. Taking the LO as $b = |\beta| e^{i\theta}$ and using the same calculations for homodyne detection, the

photon number at two detectors in heterodyne detection are

$$N_c = \frac{1}{2}(a_{+1}^\dagger + a_{-1}^\dagger + \beta e^{i\theta})(a_{+1} + a_{-1} + \beta e^{-i\theta}), \quad (5.26)$$

$$N_d = \frac{1}{2}(a_{+1}^\dagger + a_{-1}^\dagger - \beta e^{i\theta})(a_{+1} + a_{-1} - \beta e^{-i\theta}), \quad (5.27)$$

where θ is the initial phase of LO. Because the initial phase of signal is taken as 0, θ also means the initial phase difference between LO and signal fields. Subtracting N_c and N_d to get the photon number difference

$$N_- = \beta \left[(a_{+1} e^{i\Omega_1 t} + a_{-1} e^{-i\Omega_1 t}) e^{i\theta} + (a_{+1}^\dagger e^{-i\Omega_1 t} + a_{-1}^\dagger e^{i\Omega_1 t}) e^{-i\theta} \right], \quad (5.28)$$

Express N_- in terms of quadrature Q and P as

$$N_- = \sqrt{2}\beta(R\cos\Omega_1 t + I\sin\Omega_1 t), \quad (5.29)$$

where R and I correspond to the real and imaginary FT coefficients at frequency Ω_1 :

$$R_1 = \cos\theta(Q_{+1} + Q_{-1}) - \sin\theta(P_{+1} + P_{-1}), \quad (5.30)$$

$$I_1 = \sin\theta(-Q_{+1} + Q_{-1}) + \cos\theta(-P_{+1} + P_{-1}). \quad (5.31)$$

Furthermore, if the signal have more than two frequencies $\omega_{\pm n} = \omega_0 \pm \Omega_n$, the photon difference becomes the sum of all the frequency components

$$N_- = \sqrt{2}\beta \sum_n (R_n \cos\Omega_n t + I_n \sin\Omega_n t). \quad (5.32)$$

Using FT, we can get the real (R_n) and (I_n) terms for each Ω_n :

$$R_n = \cos\theta(Q_{+n} + Q_{-n}) - \sin\theta(P_{+n} + P_{-n}), \quad (5.33)$$

$$I_n = \sin\theta(-Q_{+n} + Q_{-n}) + \cos\theta(-P_{+n} + P_{-n}). \quad (5.34)$$

5.3 Quantum homodyne measurement of the entangled comb

In previous section, we discussed about the heterodyne detection involving vacuum mode because the LO frequency is shifted out of the range of OPO mode frequency, making LO beat with quantum light and vacuum at the same time. In this section, another case where the LO frequency is at the center of OPO mode and LO only beats with quantum light (no vacuum mode is involved) will be discussed.

The experimental setup is shown in Fig.5.6. The OPO we used in this experiment is an old version which has 10 MHz linewidth. The details of this OPO setup can be found in Chun-Hung's thesis [76]. The LO frequency is the same as center frequency

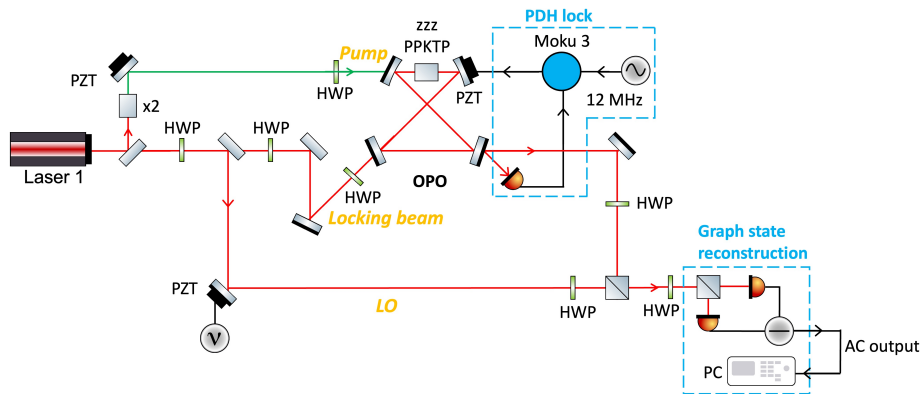


Figure 5.6: Experimental setup for intra-mode squeezing measurement.

of an OPO mode, which equal to half of pump frequency. The frequency relationship is shown in Fig.5.7. The linewidth of LO is 1 kHz. Therefore, LO beats with all the intra-mode within the OPO linewidth. The modes that we measure are two modes that have frequency $\omega_0 \pm \Omega_1$ beating with LO, which are quantum mode only and no vacuum is involved in this measurement. From Eq. (5.33) and Eq. (5.34), when

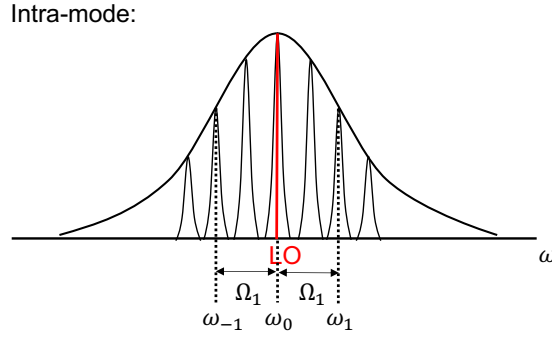


Figure 5.7: Intra-mode squeezing frequency relationship.

phase between LO and signal is $\theta = \pi/2$, the R_n and I_n becomes the TMS squeezed quadrature

$$R_n = -(P_{-n} + P_{+n}), \quad (5.35)$$

$$I_n = -Q_{-n} + Q_{+n}. \quad (5.36)$$

In the experiment, the phase θ can be tuned by applying different voltage to the PZT mounted on the mirror to change the path length of LO.

The sampling rate is set to be 50 MHz, which is larger than the linewidth of the cavity mode in order to avoid aliasing. One measurement lasts for 100 μ s so that the frequency domain resolution bandwidth is 10 kHz. We performed N measurements and calculated the variance of squeezed quadrature shown in Eq. (5.35). The

squeezing level is

$$S_{dB} = 20\log_{10} \frac{\Delta(Q_{+N} - Q_{-N})_{signal}}{\Delta(Q_{+N} - Q_{-N})_{shotnoise}} = 20\log_{10} \frac{\Delta(P_{+N} + P_{-N})_{signal}}{\Delta(P_{+N} + P_{-N})_{shotnoise}}, \quad (5.37)$$

where the signal quadrature was measured by interfering LO and quantum signal, and the shot noise was measured by blocking the pump so that there was no quantum light emitted by OPO and the LO was interfered with vacuum.

The intra-mode squeezed quadrature of is plotted as in Fig.5.8. The x axis is the frequency difference between the two-mode squeezed pairs and the OPO center mode, and y axis is the squeezing level calculated in Eq. (5.37). We measured the maximum squeezing of 1 dB at 2 MHz. However, we expected the squeezing to be around 3.2 dB, which is the level we measured before [3]. This was caused by the loss and phase noise in this experimental setup. The careful investigation of these reasons can be found in Chapter 5 of Chun-Hung's thesis [76]. For the results that we have here, it is obvious that the squeezing level decreases obviously at 5 MHz, which is the half frequency of cavity mode linewidth, and the squeezing is not detectable at frequency larger than 10 MHz. Fig.5.8 (a) shows the variance of 1875 measurements and Fig.5.8 (b) shows the variance of 18750 measurements, which is more accurate than the results in Fig.5.8 (a).

One problem of this measurement is the LO phase was not stabilized. If the LO phase drifted away from $\pi/2$, the real and imaginary part of FT is a mixture of squeezed and anti-squeezed quadrature, which resulted in a smaller squeezing level. To solve this problem, a possible method is adding a probe beam and locking LO phase to probe beam as discussed Section 4.4.

This method can only measure the squeezing quadrature which are the quadrature

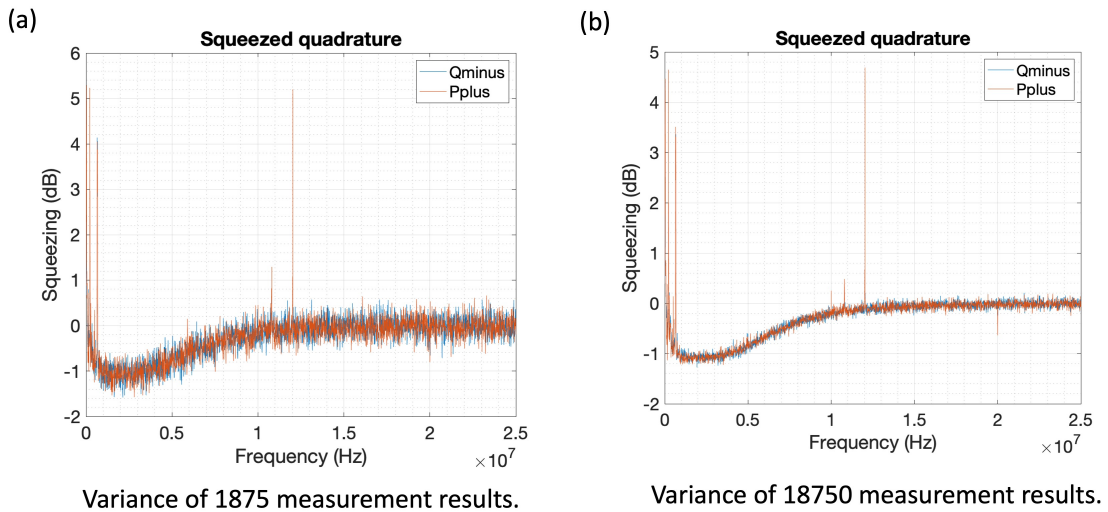


Figure 5.8: Two-mode squeezing inside an OPO cavity mode.

combinations of two modes. It is impossible to calculate the quadrature of each mode using this method [75]. In order to measure the quadrature of each mode, LO frequency needs to be shifted away from the center frequency of the OPO mode and letting LO interfere with both quantum light and vacuum as discussed in Section 5.4.

5.4 Quantum heterodyne measurement of the entangled comb

In this section, I will present some results of intra-modes quadrature measurements using the experimental setup shown in Fig.4.1, with the EOM after OPO turned off. Using an AOM to shift the LO frequency 50 MHz away from the center of OPO mode frequency as shown in Fig.5.9. The OPO mode has 30 MHz FWHM. We are interested in the signal within bandwidth of 100 MHz so that it allows LO beating with entire OPO mode. Therefore, the sampling rate is set to be 2 GHz, which is 20 times larger

than the signal bandwidth. We performed 1000 times of measurements with each measurement lasted for 10^{-5} s, which gives the resolution (frequency spacing) of 100 kHz.

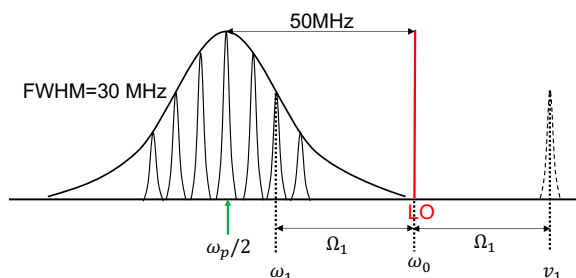


Figure 5.9: Heterodyne measurement signal bandwidth.

5.4.1 Fourier transform spectrum

Fourier transform amplitude

The Fourier transform amplitudes of detected signals are shown in Fig.5.10. The x axis are the frequency range from DC to 100 MHz and the y axis shows the average value of signal's the Fourier transform amplitude over 1000 times of measurements.

We first measured the dark noise spectrum (Fig.5.10 (a)). In this case, all the light was blocked out. There are radio frequency signal pickups at 10 MHz, 50 MHz and 80 MHz. The LO spectrum (Fig.5.10 (b)) was measured when only LO was turned on. It has a weak 12 MHz signal coming from the laser phase modulation which is used to do PDH locking. Comparing the dark noise and LO spectrum, the photon detector has a detection bandwidth of 100 MHz.

Fig.5.10 (c) shows the spectrum of LO and probe beam beat note spectrum. The frequency difference between LO and probe beam is 50 MHz and both LO and probe

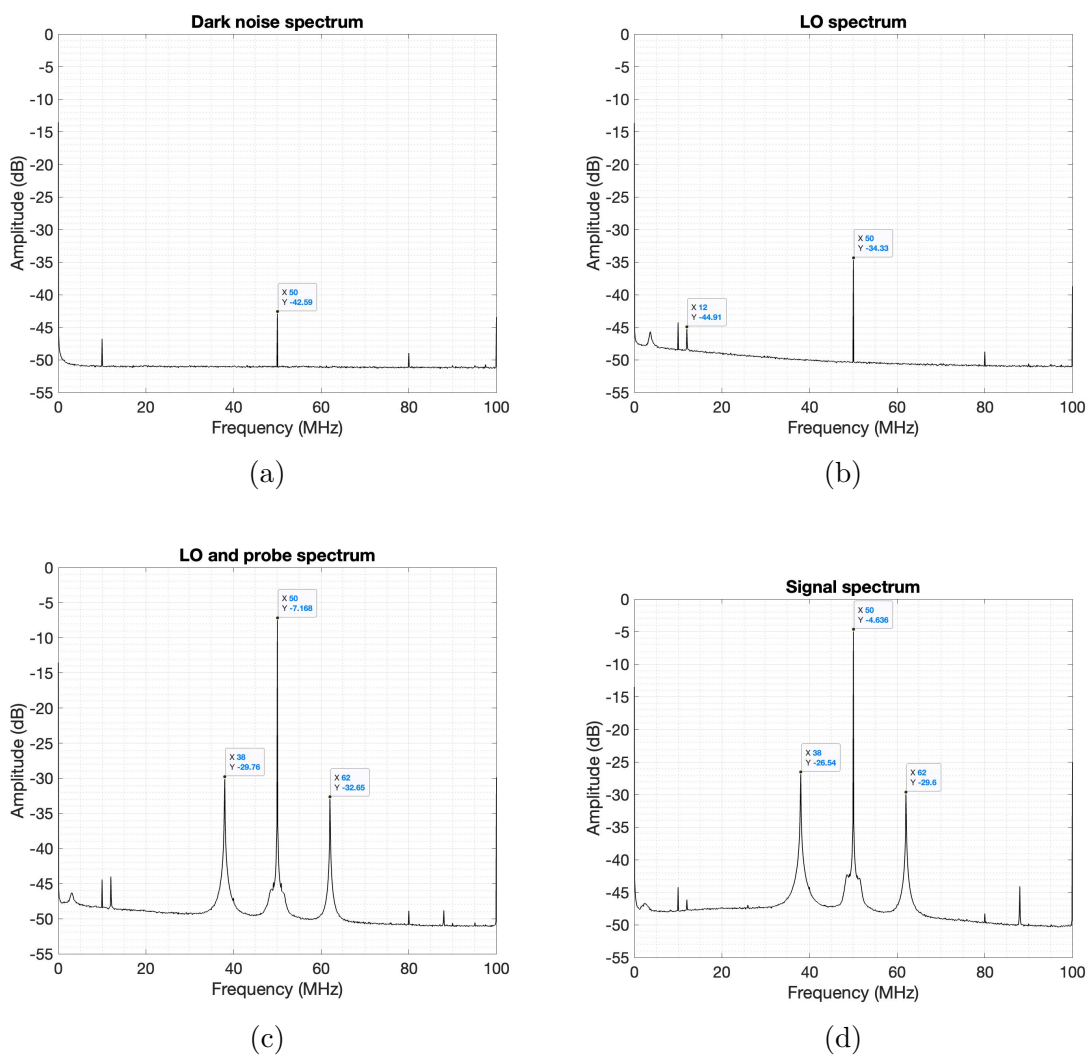


Figure 5.10: Fourier transform amplitude of different signals. (a) Spectrum of dark noise, measured without any light. (b) Spectrum of LO. (c) Spectrum of LO and probe beam without pump. (d) Spectrum of LO and probe beam with pump.

beam have weak 12 MHz modulations. The 50 MHz peak shown in this case contains three components: beat between LO and probe beam, beat between LO and probe beam's ± 1 st order 12 MHz sidebands. Meanwhile, the 38 MHz and 62 MHz peaks are LO carrier beating with the probe beam sidebands plus probe beam carrier beating with LO sidebands. Because the LO power (7.1 mW) is much larger than probe beam power (37.4 μ W), the beating between LO carrier and probe beam has the main contribution to those two peaks.

Fig.5.10 (d) shows the spectrum of LO and probe beat when pump is turned on and pump phase locking with probe beam is engaged so that the probe beam power is locked to maximum because of parametric amplification. Since the probe beam power is amplified, the 50 MHz peak is 2.532 dB higher than the peak without pump shown in Fig.5.10 (c), which corresponds probe beam power parametric gain is 3.21. We can see that the OPO amplifies the probe field approximately by a factor of 1.79, which would hint at a squeezing level of 4.94 dB.

Fourier transform phase

In chapter 4, I have already showed that relative phase between LO and probe beam are locked. This means the initial phase of the 50 MHz signal, generated by beating LO with probe beam, should be stable. I will discuss how this phase is related to the Fourier transform phase we measured.

The FT phase of this 50 MHz signal from LO and probe beam beat with pump off and on is shown in Fig.5.11. In this figure, the phase of 1000 time of measurements are plotted and they are distributed at 5 different values. From subsection 5.4.2, this FT phase is the initial phase difference between LO and probe beam. Because LO

and probe beam phase was locked, the relative phase is stable. However, as we started recording the data at different time, the initial phase has different values. Those 1000 times of measurements were performed in this way: each measurement lasted for 10^{-5} s, and the starting time of each measurement had an interval of $\Delta t = 1.00096 \times 10^{-4}$ s, which contains 5004.8 periods of 50 MHz signal. Therefore, if the first measurement started with initial phase θ_0 , the second, third, fourth and fifth measurements initial phases are $\theta_0 + 0.8 \times 2\pi$, $\theta_0 + 1.6 \times 2\pi$, $\theta_0 + 2.4 \times 2\pi$, $\theta_0 + 3.2 \times 2\pi$. Starting from the sixth measurement, the initial phase is θ_0 again. This is the reason why there are 5 different values of initial phase. Also, because the fact that the first measurement has the same trigger level, the average value of each phase set keeps the same no matter if pump turned on or off.

5.4.2 Quadrature measurement

Meaning of the initial phase

In order to solve the equations Eq. (5.33) and Eq. (5.34) to get Q_n and P_n , it is important to know the value of θ , which is the initial phase difference between LO and the signal.

From Eq. (4.61), the relative phase $\Delta\phi$ between LO and probe beam is the initial phase (when $t = 0$) of their 50 MHz beat signal. A problem in the experiment is how to define this initial phase since the light is propagating as free field and its phase is different at different time or position. I will prove next that this initial phase $\Delta\phi$ is the FT phase θ and can be calculated using Eq. (5.6).

In this experiment (Fig.4.1), the mode a_{-1} in Eq. (5.28) is the probe beam, which is treated as coherent state so that $a \rightarrow |\alpha|$ (its phase is considered as 0 for simplicity

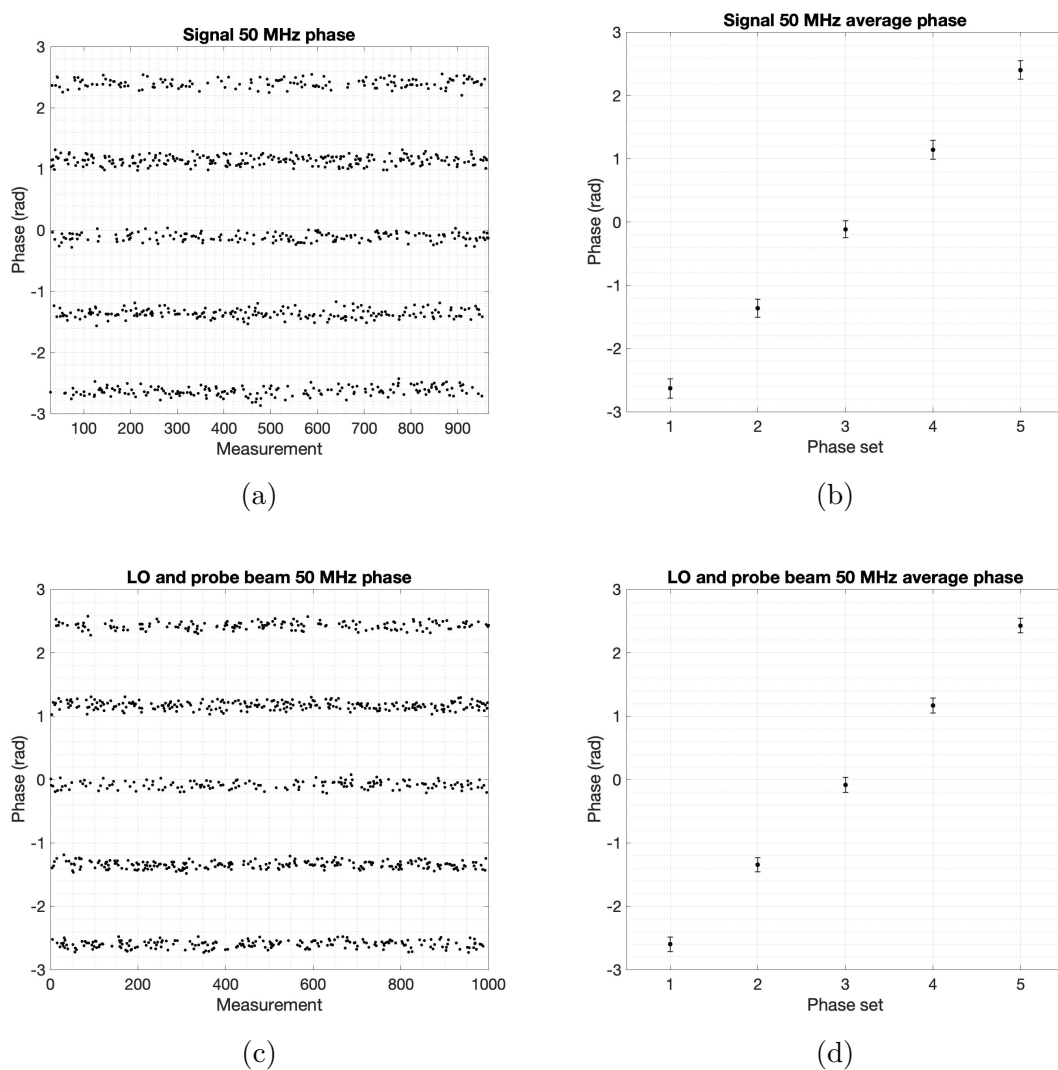


Figure 5.11: Fourier transform phase of 50 MHz beat signal between LO and probe beam with pump turned on and off. (a) and (c) are 50 MHz phase distribution of 1000 times of measurements with pump turned on and off. There are 5 phase sets in both cases. (b) and (d) show the 50 MHz phase average for 5 different phase sets with pump turned on and off. Error bar shown the range including 95.8% data points.

without the loss of generality). The mode a_{+1} in Eq. (5.28) is the vacuum mode so that $v \rightarrow 0$. Replacing the phase θ with the relative phase between LO and probe beam $\Delta\phi$, the photon number difference Eq. (5.28) becomes

$$\begin{aligned} N_- &= \beta [(|\alpha|e^{i\Omega t})e^{i\Delta\phi} + (|\alpha|e^{-i\Omega t})e^{-i\Delta\phi}] \\ &= 2\beta [\cos\Omega t(|\alpha|\cos\Delta\phi) + \sin\Omega t(|\alpha|\sin\Delta\phi)], \end{aligned} \quad (5.38)$$

where $2\beta|\alpha|\cos\Delta\phi = R$ is the real part of FT and $2\beta|\alpha|\sin\Delta\phi = I$ is the imaginary part of FT. Using Eq. (5.6), the phase given by the FT is

$$\Delta\phi = \tan^{-1} \frac{I}{R}. \quad (5.39)$$

The free field evolution of the probe beam and LO introduces a phase shift in $\Delta\phi \rightarrow \Delta\phi' = \Delta\phi + \delta\phi$. Therefore, $\Delta\phi'$ still can be calculated by the FT phase which means the free field evolution phase is already included in the FT phase and the start point defining the initial phase is when we start to acquire data.

Measuring quadratures of the probe beam

We can use the FT complex value of 50 MHz component to calculate the quadratures of probe beam. The linear combinations of Eq.5.30 and Eq.5.31 give

$$R \sin\theta + I \cos\theta = \sin 2\theta Q_v + \cos 2\theta P_v - P_a, \quad (5.40)$$

$$R \cos\theta - I \sin\theta = -\sin 2\theta P_v + \cos 2\theta Q_v + Q_a, \quad (5.41)$$

where $R + iI$ is the FT complex number of 50 MHz signal, phase $\theta = \tan^{-1} \frac{I}{R}$. Q_a and P_a are the amplitude and phase quadrature of probe beam. Q_v and P_v are the

amplitude and phase quadrature of vacuum mode. For n times of measurement, the average of P_a and Q_a are

$$\langle P_a \rangle = \langle R \sin\theta + I \cos\theta \rangle - \langle \sin 2\theta Q_v \rangle - \langle \cos 2\theta P_v \rangle, \quad (5.42)$$

$$\langle Q_a \rangle = \langle R \cos\theta - I \sin\theta \rangle + \langle \sin 2\theta P_v \rangle - \langle \cos 2\theta Q_v \rangle. \quad (5.43)$$

The quadrature average of vacuum state satisfies $\langle P_v \rangle = \langle Q_v \rangle = 0$ when $n \rightarrow \infty$, therefore

$$\langle \sin 2\theta Q_v \rangle \leq \langle Q_v \rangle \rightarrow 0, \quad (5.44)$$

$$\langle \sin 2\theta P_v \rangle \leq \langle P_v \rangle \rightarrow 0, \quad (5.45)$$

$$\langle \cos 2\theta Q_v \rangle \leq \langle Q_v \rangle \rightarrow 0, \quad (5.46)$$

$$\langle \cos 2\theta P_v \rangle \leq \langle P_v \rangle \rightarrow 0. \quad (5.47)$$

When n is large enough, the quadrature average of the probe beam is

$$\langle P_a \rangle = \langle R \sin\theta + I \cos\theta \rangle = A \sin 2\theta, \quad (5.48)$$

$$\langle Q_a \rangle = \langle R \cos\theta - I \sin\theta \rangle = A \cos 2\theta, \quad (5.49)$$

where A is the FT amplitude, thus $R = A \cos\theta$ and $I = A \sin\theta$. Using this method, we can calculate the expectation and standard deviation of P and Q quadratures for probe beam at different phase shown in Fig.5.11a. The results are shown in Fig.5.12. The coordinates of each point correspond to the measured mean value of Q and P with different phase set in Fig.5.11.

The error bar shows the range of mean value plus and minus the standard deviation (ΔQ and ΔP). The quadrature averages are amplified when pump is turned

on compared to pump turned off, which can be explained by Eq. (5.48) since A is amplified by the pump. The error bars shown in Fig.5.12 are dominated by the measurement errors. Form Eq. (5.48), the measured phase error contributes to the quadrature errors and the errors of amplitude A can be neglected because the probe beam power is stabilized by locking loops (the measured standard deviation of power is about 50 time smaller than the phase standard deviation). Therefore, the quadrature errors can be estimated as

$$\Delta P = 2A\cos 2\theta\Delta\theta, \quad (5.50)$$

$$\Delta Q = 2A\sin 2\theta\Delta\theta, \quad (5.51)$$

which explain that when $2\theta \rightarrow k\pi$, ΔQ is small and ΔP is large, while $2\theta \rightarrow (2k + 1)\pi/2$, ΔQ is large and ΔP is small (k is integer).

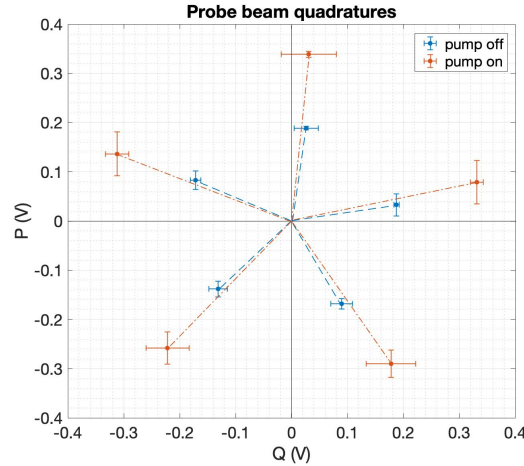


Figure 5.12: Probe beam quadrature plot.

In this experiment (Fig.4.1), the signal we are measuring is the full spectrum of single OPO mode, including the quantum light generated from spontaneous parametric down conversion and the probe beam being amplified by parametric amplification

process. From the analysis in Section 4.3, when the pump phase is locked to the probe beam phase to maximize the probe beam power, the initial phase of quantum light is the same as the initial phase of probe beam. When the light propagates in the air, the dispersion can be ignored. The measured phase between LO and probe beam is the same as the phase between LO and the quantum light, which can't be measured accurately because the quantum light is too weak.

The heterodyne detection combined with FFT provides a method to measure quadrature related properties of a cluster state, such as the nullifiers and covariance matrix. In the next part, I will show the results of intra-mode squeezing nullifiers and give an explanation why we currently can't see squeezing. The covariance matrix mathematical derivations from the FT complex number of the heterodyne detection signal is presented in Appendix A.

Intra-mode squeezing measurement

Considering the LO frequency ω_0 , two-mode squeezed state (TMS) mode pairs are mode a and b , which have frequency $\omega_0 - \Omega_1$ and $\omega_0 - \Omega_2$. The corresponding vacuum mode are v and u , with frequencies $\omega_0 + \Omega_1$ and $\omega_0 + \Omega_2$.

The results of Fourier transform give the real and imaginary part of frequency components Ω_1 and Ω_2 . For frequency component Ω_1 :

$$R_1 = \cos\theta(Q_a + Q_v) - \sin\theta(P_a + P_v), \quad (5.52)$$

$$I_1 = \sin\theta(-Q_a + Q_v) + \cos\theta(-P_a + P_v). \quad (5.53)$$

For frequency component Ω_2 :

$$R_2 = \cos\theta(Q_b + Q_u) - \sin\theta(P_b + P_u), \quad (5.54)$$

$$I_2 = \sin\theta(-Q_b + Q_u) + \cos\theta(-P_b + P_u). \quad (5.55)$$

Using the vacuum state quadrature relations Eq.A.1, the squeezed quadrature variance is

$$\Delta^2(Q_a - Q_b) = \Delta^2[(R_1 - R_2)\cos\theta - (I_1 - I_2)\sin\theta] - 1, \quad (5.56)$$

$$\Delta^2(Q_a + Q_b) = \Delta^2[(R_1 + R_2)\cos\theta - (I_1 + I_2)\sin\theta] - 1. \quad (5.57)$$

Using the equations above, the modes a and b being the intra-mode pairs whose frequencies are symmetric to the mode center, the variance of $Q_{minus} = Q_a - Q_b$ and $Q_{plus} = Q_a + Q_b$ are plotted in Fig.5.13. We performed 1000 times of measurements and the resolution is 100 kHz. The blue and red traces were measured when pump

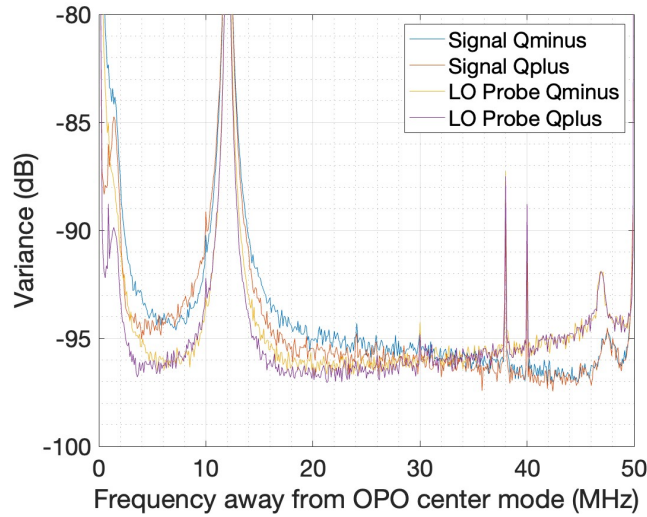


Figure 5.13: Intra-mode Q_{minus} and Q_{plus} variance plot.

was turned on, which were the signal of intra-mode two-mode squeezed states. It is

important to compare this quantum signal with the case where there is no quantum light but all the other conditions are kept the same. A straightforward method is comparing the signal with pump turned on to the signal with pump turned off, which is the shotnoise. However, in this experimental setup, the probe beam power is amplified by the pump, so that we can't make the comparison simply by turning on or off the pump. A good calibration based on the parametric gain needs to be applied to the signal when pump turned off. The yellow and purple traces in Fig.5.13 are the calibrated variance of Q_{minus} and Q_{plus} for the LO and probe beam only with pump off.

We expected that we could see squeezing in this plot at the frequency lower than 35 MHz within the OPO linewidth, which means the noise (variance) of the signal quadrature Q_{minus} or Q_{plus} should be reduced smaller than the calibrated shotnoise. However, we did not see this in our results. This could be due to several reasons. First, there is too much classical noise from the LO and probe beam beat signal, including the intensity noise and the phase noise. This classical noise is not well subtracted and controlled making the quantum fluctuations buried and are not observable. Second, the number of measurements is not large enough, making the residual noise, which should be 0 with averaging infinite number of measurements, comparable with or even larger than the quantum noise. We haven't found the solutions to these problems due to lab moving and other facility reasons. In order to observe the squeezing and even measure other cluster states successfully in the future, these problems need further investigation.

Chapter 6

Conclusion

In this thesis, I have presented theoretical analysis of generating CV cluster states of arbitrary dimension by a quantum optical frequency comb with phase modulation at multiples of the comb frequency spacing. The dimension of this state is determined by the number and the ratio of phase modulation frequencies. With careful error analysis, it is proved that these CV cluster states can have low error levels which make them compatible with the fault tolerance in CV quantum computing. Note that the phase modulation can be performed both external to the OPO or intrinsic to the OPO, which is a simple and compact approach compared to all previous generation of cluster states.

Then, I have discussed the experimental works to stabilize the optical system which was designed to generate the cluster state based on the theory work mentioned above. The stabilization systems including using Pound-Drever-Hall locking technique to stabilize the OPO cavity length against both long term drifting and high frequency perturbation, pump and probe beam phase locking to make the probe beam power stay at the maximum value and LO-probe beam phase locking to stabilize the relative initial phase between LO and probe beam.

Finally, I discuss the quadrature measurement using both quantum homodyne

and heterodyne detection combined with Fourier transform. I presented the results of intra-mode squeezing measurement using quantum homodyne frequency-heterodyne method. I also presented the preliminary results using quantum heterodyne detection to measure the intra-mode squeezing. Frequency-heterodyne detection with Fourier transformation is a method towards reconstructing the whole large scale cluster state by calculating the covariance matrix. Instead of only get the nullifiers, this method provide a more direct access to the cluster state characterization, including graph itself showing quantum correlations and their errors. Further investigations about the reduction of classical noise are required in order to achieve this kind of fully characterization of cluster states.

Bibliography

- [1] R. Raussendorf and H. J. Briegel. “A one-way quantum computer”. In: *Phys. Rev. Lett.* 86 (2001), p. 5188.
- [2] H. J. Briegel and R. Raussendorf. “Persistent entanglement in arrays of interacting particles”. In: *Phys. Rev. Lett.* 86 (2001), p. 910.
- [3] Moran Chen, Nicolas C. Menicucci, and Olivier Pfister. “Experimental realization of multipartite entanglement of 60 modes of a quantum optical frequency comb”. In: *Phys. Rev. Lett.* 112 (12 Mar. 2014), p. 120505. DOI: [10.1103/PhysRevLett.112.120505](https://doi.org/10.1103/PhysRevLett.112.120505). URL: <http://link.aps.org/doi/10.1103/PhysRevLett.112.120505>.
- [4] Warit Asavanant et al. “Generation of time-domain-multiplexed two-dimensional cluster state”. In: *Science* 366.6463 (2019), pp. 373–376. ISSN: 0036-8075. DOI: [10.1126/science.aay2645](https://doi.org/10.1126/science.aay2645). eprint: <https://science.sciencemag.org/content/366/6463/373.full.pdf>. URL: <https://science.sciencemag.org/content/366/6463/373>.
- [5] Mikkel V. Larsen et al. “Deterministic generation of a two-dimensional cluster state”. In: *Science* 366.6463 (2019), pp. 369–372. ISSN: 0036-8075. DOI: [10.1126/science.aay4354](https://doi.org/10.1126/science.aay4354). eprint: <https://science.sciencemag.org/content/366/6463/369.full.pdf>. URL: <https://science.sciencemag.org/content/366/6463/369>.
- [6] Seiji Armstrong et al. “Programmable multimode quantum networks”. In: *Nat. Commun.* 3:1026 (2012), pp. 1–8.

- [7] Rafael N. Alexander et al. “One-way quantum computing with arbitrarily large time-frequency continuous-variable cluster states from a single optical parametric oscillator”. In: *Phys. Rev. A* 94 (3 Sept. 2016), p. 032327. DOI: [10.1103/PhysRevA.94.032327](https://doi.org/10.1103/PhysRevA.94.032327). URL: <http://link.aps.org/doi/10.1103/PhysRevA.94.032327>.
- [8] Richard P. Feynman. “Simulating Physics With Computers”. In: *Int. J. Theor. Phys.* 21 (1982), pp. 467–488.
- [9] D. Deutsch and R. Jozsa. “Rapid solution of problems by quantum computation”. In: *Proc. Roy. Soc. Lond. A* 439.1907 (1992), pp. 553–558.
- [10] L. Grover. “A fast quantum mechanical algorithm for database search”. In: *Proc. 28th Annual ACM Symposium on Theory of Comput.* Philadelphia, PA, 1996, pp. 212–219.
- [11] Michael A. Nielsen and Isaac L. Chuang. *Quantum computation and quantum information*. Cambridge, U.K.: Cambridge University Press, 2000.
- [12] P. W. Shor. “Algorithms for quantum computation: discrete logarithms and factoring”. In: *Proceedings, 35th Annual Symposium on Foundations of Computer Science*. Ed. by S. Goldwasser. Santa Fe, NM: IEEE Press, Los Alamitos, CA, 1994, pp. 124–134.
- [13] Frank Arute et al. “Quantum supremacy using a programmable superconducting processor”. In: *Nature* 574.7779 (2019), pp. 505–510. DOI: [10.1038/s41586-019-1666-5](https://doi.org/10.1038/s41586-019-1666-5). URL: <https://doi.org/10.1038/s41586-019-1666-5>.
- [14] P Walther et al. “Experimental One-Way Quantum Computing”. In: *Nature (London)* 434 (2005), p. 169. DOI: [10.1038/nature03347](https://doi.org/10.1038/nature03347).

- [15] Nicolas C. Menicucci. “Fault-tolerant measurement-based quantum computing with continuous-variable cluster states”. In: *Phys. Rev. Lett.* 112 (12 Mar. 2014), p. 120504. DOI: [10.1103/PhysRevLett.112.120504](https://doi.org/10.1103/PhysRevLett.112.120504). URL: <http://link.aps.org/doi/10.1103/PhysRevLett.112.120504>.
- [16] Blayne W. Walshe et al. “Robust fault tolerance for continuous-variable cluster states with excess antisqueezing”. In: *Phys. Rev. A* 100 (1 July 2019), p. 010301. DOI: [10.1103/PhysRevA.100.010301](https://doi.org/10.1103/PhysRevA.100.010301). URL: <https://link.aps.org/doi/10.1103/PhysRevA.100.010301>.
- [17] Kosuke Fukui et al. “High-Threshold Fault-Tolerant Quantum Computation with Analog Quantum Error Correction”. In: *Phys. Rev. X* 8 (2 May 2018), p. 021054. DOI: [10.1103/PhysRevX.8.021054](https://doi.org/10.1103/PhysRevX.8.021054). URL: <https://link.aps.org/doi/10.1103/PhysRevX.8.021054>.
- [18] N. C. Menicucci et al. “Universal quantum computation with continuous-variable cluster states”. In: *Phys. Rev. Lett.* 97 (2006), p. 110501. DOI: [doi:10.1103/PhysRevLett.97.110501](https://doi.org/10.1103/PhysRevLett.97.110501).
- [19] R Raussendorf, J Harrington, and K Goyal. “A fault-tolerant one-way quantum computer”. In: *Ann. Phys. (NY)* 321.9 (2006), pp. 2242–2270.
- [20] D. F. Walls and G. J. Milburn. *Quantum Optics*. Springer, Berlin, 1994.
- [21] Pierre Meystre and Murray Sargent III. *Elements of Quantum Optics*. Springer, 2007.
- [22] Olivier Pfister. “Continuous-variable quantum computing in the quantum optical frequency comb”. In: *Journal of Physics B: Atomic, Molecular and Optical Physics* 53 (2020), p. 012001. DOI: [10.1088/1361-6455/ab526f](https://doi.org/10.1088/1361-6455/ab526f). URL: <http://iopscience.iop.org/10.1088/1361-6455/ab526f>.

- [23] Mile Gu et al. “Quantum computing with continuous-variable clusters”. In: *Phys. Rev. A* 79 (2009), p. 062318.
- [24] Christian Weedbrook et al. “Gaussian quantum information”. In: *Rev. Mod. Phys.* 84 (2 May 2012), pp. 621–669. DOI: [10.1103/RevModPhys.84.621](https://doi.org/10.1103/RevModPhys.84.621). URL: <http://link.aps.org/doi/10.1103/RevModPhys.84.621>.
- [25] Seth Lloyd and Samuel L. Braunstein. “Quantum computation over continuous variables”. In: *Phys. Rev. Lett.* 82 (1999), p. 1784.
- [26] Dave Bacon. “Too entangled to quantum compute one-way”. In: *Physics* 2 (May 2009), p. 38. DOI: [10.1103/Physics.2.38](https://doi.org/10.1103/Physics.2.38). URL: <http://link.aps.org/doi/10.1103/Physics.2.38>.
- [27] D. Gross, S. T. Flammia, and J. Eisert. “Most quantum states are too entangled to be useful as computational resources”. In: *Phys. Rev. Lett.* 102 (19 May 2009), p. 190501. DOI: [10.1103/PhysRevLett.102.190501](https://doi.org/10.1103/PhysRevLett.102.190501). URL: <http://link.aps.org/doi/10.1103/PhysRevLett.102.190501>.
- [28] Michael J. Bremner, Caterina Mora, and Andreas Winter. “Are Random Pure States Useful for Quantum Computation?” In: *Phys. Rev. Lett.* 102 (19 May 2009), p. 190502. DOI: [10.1103/PhysRevLett.102.190502](https://doi.org/10.1103/PhysRevLett.102.190502). URL: <http://link.aps.org/doi/10.1103/PhysRevLett.102.190502>.
- [29] M. Hein, J. Eisert, and H. J. Briegel. “Multipartite entanglement in graph states”. In: *Phys. Rev. A* 69.6, 062311 (2004), p. 062311.
- [30] Jing Zhang and Samuel L. Braunstein. “Continuous-variable Gaussian analog of cluster states”. In: *Phys. Rev. A* 73.3, 032318 (2006), p. 032318.
- [31] Nicolas C. Menicucci, Steven T. Flammia, and Peter van Loock. “Graphical calculus for Gaussian pure states”. In: *Phys. Rev. A* 83 (2011), p. 042335.

- [32] Olivier Pfister et al. “Multipartite continuous-variable entanglement from concurrent nonlinearities”. In: *Phys. Rev. A* 70.2 (2004), p. 020302. DOI: [10.1103/PhysRevA.70.020302](https://doi.org/10.1103/PhysRevA.70.020302).
- [33] Nicolas C. Menicucci, Steven T. Flammia, and Olivier Pfister. “One-way quantum computing in the optical frequency comb”. In: *Phys. Rev. Lett.* 101 (2008), p. 130501. DOI: [10.1103/PhysRevLett.101.130501](https://doi.org/10.1103/PhysRevLett.101.130501).
- [34] S. T. Flammia, N. C. Menicucci, and O. Pfister. “The optical frequency comb as a one-way quantum computer”. In: *J. Phys. B*, 42 (2009), p. 114009.
- [35] Matthew Pysher et al. “Parallel generation of quadripartite cluster entanglement in the optical frequency comb”. In: *Phys. Rev. Lett.* 107.3 (July 2011), p. 030505. DOI: [10.1103/PhysRevLett.107.030505](https://doi.org/10.1103/PhysRevLett.107.030505).
- [36] Jonathan Roslund et al. “Wavelength-Multiplexed Quantum Networks with Ultrafast Frequency Combs”. In: *Nat. Photon.* 8 (2014), p. 109.
- [37] Shota Yokoyama et al. “Ultra-large-scale continuous-variable cluster states multiplexed in the time domain”. In: *Nat. Photon.* 7 (2013), p. 982.
- [38] Jun-ichi Yoshikawa et al. “Invited Article: Generation of one-million-mode continuous-variable cluster state by unlimited time-domain multiplexing”. In: *APL Photonics* 1.6, 060801 (2016), p. 060801. DOI: <http://dx.doi.org/10.1063/1.4962732>. URL: <http://scitation.aip.org/content/aip/journal/app/1/6/10.1063/1.4962732>.
- [39] Raphael Pooser and Jietai Jing. “Continuous-variable cluster-state generation over the optical spatial mode comb”. In: *Phys. Rev. A* 90 (4 Oct. 2014), p. 043841. DOI: [10.1103/PhysRevA.90.043841](https://doi.org/10.1103/PhysRevA.90.043841). URL: <https://link.aps.org/doi/10.1103/PhysRevA.90.043841>.

- [40] Rongguo Yang et al. “Spatiotemporal graph states from a single optical parametric oscillator”. In: *arXiv:1911.01453 [quant-ph]* (2019). URL: <https://arxiv.org/abs/1911.01453>.
- [41] Nicolas C. Menicucci. “Temporal-mode continuous-variable cluster states using linear optics”. In: *Phys. Rev. A* 83.6 (June 2011), p. 062314. DOI: [10.1103/PhysRevA.83.062314](https://doi.org/10.1103/PhysRevA.83.062314).
- [42] Pei Wang et al. “Weaving quantum optical frequency combs into hypercubic cluster states”. In: *Phys. Rev. A* 90 (2014), p. 032325. URL: <http://dx.doi.org/10.1103/PhysRevA.90.032325>.
- [43] Xuan Zhu et al. “Cluster state engineering by phase modulation of the quantum optical frequency comb”. In: *arXiv:1912.11215 [quant-ph]* (2020).
- [44] Carlos González-Arciniegas et al. “Cluster States from Gaussian States: Essential Diagnostic Tools for Continuous-Variable One-Way Quantum Computing”. In: *PRX Quantum* 2 (3 Sept. 2021), p. 030343. DOI: [10.1103/PRXQuantum.2.030343](https://doi.org/10.1103/PRXQuantum.2.030343). URL: <https://link.aps.org/doi/10.1103/PRXQuantum.2.030343>.
- [45] J. U. Fürst et al. “Quantum Light from a Whispering-Gallery-Mode Disk Resonator”. In: *Phys. Rev. Lett.* 106 (11 Mar. 2011), p. 113901. DOI: [10.1103/PhysRevLett.106.113901](https://doi.org/10.1103/PhysRevLett.106.113901). URL: <https://link.aps.org/doi/10.1103/PhysRevLett.106.113901>.
- [46] Avik Dutt et al. “On-Chip Optical Squeezing”. In: *Phys. Rev. Applied* 3 (4 Apr. 2015), p. 044005. DOI: [10.1103/PhysRevApplied.3.044005](https://doi.org/10.1103/PhysRevApplied.3.044005). URL: <https://link.aps.org/doi/10.1103/PhysRevApplied.3.044005>.
- [47] Francesco Lenzini et al. “Integrated photonic platform for quantum information with continuous variables”. In: *Sci. Adv.* 4.12 (2018). DOI: [10.1126/sciadv](https://doi.org/10.1126/sciadv).

- aat9331. eprint: <https://advances.sciencemag.org/content/4/12/eaat9331.full.pdf>. URL: <https://advances.sciencemag.org/content/4/12/eaat9331>.
- [48] F. Mondain et al. “Chip-based squeezing at a telecom wavelength”. In: *Photon. Res.* 7.7 (July 2019), A36–A39. DOI: [10.1364/PRJ.7.000A36](https://doi.org/10.1364/PRJ.7.000A36). URL: <http://www.osapublishing.org/prj/abstract.cfm?URI=prj-7-7-A36>.
- [49] V. D. Vaidya et al. “Broadband quadrature-squeezed vacuum and nonclassical photon number correlations from a nanophotonic device”. In: *Science Advances* 6.39 (2020). DOI: [10.1126/sciadv.aba9186](https://doi.org/10.1126/sciadv.aba9186). URL: <https://advances.sciencemag.org/content/6/39/eaba9186>.
- [50] E. Wigner. “On the Quantum Correction For Thermodynamic Equilibrium”. In: *Phys. Rev.* 40.5 (June 1932), pp. 749–759. DOI: [10.1103/PhysRev.40.749](https://doi.org/10.1103/PhysRev.40.749).
- [51] Jonatan Bohr Brask. “Gaussian states and operations – a quick reference”. In: *arXiv:2102.05748v2 [quant-ph]* (2022). arXiv: [2102.05748v2 \[quant-ph\]](https://arxiv.org/abs/2102.05748v2).
- [52] Mattia Walschaers. “Non-Gaussian Quantum States and Where to Find Them”. In: *arXiv:2104.12596v3 [quant-ph]* (2021). arXiv: [2104.12596v3 \[quant-ph\]](https://arxiv.org/abs/2104.12596v3).
- [53] R. Simon, E. C. G. Sudarshan, and N. Mukunda. “Gaussian pure states in quantum mechanics and the symplectic group”. In: *Phys. Rev. A* 37 (8 Apr. 1988), pp. 3028–3038. DOI: [10.1103/PhysRevA.37.3028](https://doi.org/10.1103/PhysRevA.37.3028). URL: <http://link.aps.org/doi/10.1103/PhysRevA.37.3028>.
- [54] Mitsuyoshi Yukawa et al. “Experimental generation of four-mode continuous-variable cluster states”. In: *Phys. Rev. A* 78 (2008), p. 012301.

- [55] Daniel Gottesman. “The Heisenberg Representation of Quantum Computers”. In: arXiv:quant-ph/9807006v1, *Proceedings of the XXII International Colloquium on Group Theoretical Methods in Physics*. Ed. by S. P. Corney et al. Cambridge, MA: International Press, 1999, p. 32.
- [56] M. Ohliger, K. Kieling, and J. Eisert. “Limitations of quantum computing with Gaussian cluster states”. In: *Phys. Rev. A* 82 (2010), p. 042336.
- [57] José Capmany and Carlos R. Fernández-Pousa. “Quantum model for electro-optical phase modulation”. In: *J. Opt. Soc. Am. B* 27.6 (June 2010), A119–A129. DOI: [10.1364/JOSAB.27.00A119](https://doi.org/10.1364/JOSAB.27.00A119). URL: <http://josab.osa.org/abstract.cfm?URI=josab-27-6-A119>.
- [58] Wen-Chyuan Yueh. “Eigenvalues of several tridiagonal matrices”. In: *Applied mathematics e-notes* 5.66-74 (2005), pp. 210–230.
- [59] Z. Y. Ou et al. “Realization of the Einstein-Podolsky-Rosen paradox for continuous variables”. In: *Phys. Rev. Lett.* 68 (1992), p. 3663.
- [60] C. Schori, J. L. Sørensen, and E. S. Polzik. “Narrow-band frequency tunable light source of continuous quadrature entanglement”. In: *Phys. Rev. A* 66 (2002), p. 033802.
- [61] N. C. Menicucci et al. “Ultracompact generation of continuous-variable cluster states”. In: *Phys. Rev. A* 76 (2007), 010302(R).
- [62] Pei Wang, Wenjiang Fan, and Olivier Pfister. “Engineering large-scale entanglement in the quantum optical frequency comb: influence of the quasiphase-matching bandwidth and of dispersion”. In: *arXiv:1403.6631 [physics.optics]* (2014).

- [63] Joseph M. Lukens and Pavel Lougovski. “Frequency-encoded photonic qubits for scalable quantum information processing”. In: *Optica* 4.1 (Jan. 2017), pp. 8–16. DOI: [10.1364/OPTICA.4.000008](https://doi.org/10.1364/OPTICA.4.000008). URL: <http://www.osapublishing.org/optica/abstract.cfm?URI=optica-4-1-8>.
- [64] Michael Kues et al. “Quantum optical microcombs”. In: *Nature Photonics* 13.3 (2019), pp. 170–179. DOI: [10.1038/s41566-019-0363-0](https://doi.org/10.1038/s41566-019-0363-0). URL: <https://doi.org/10.1038/s41566-019-0363-0>.
- [65] B. E. A. Saleh and M. C. Teich. *Fundamentals of Photonics*. New York, NY: Wiley and Sons, 1991.
- [66] Robert W. Boyd. *Nonlinear Optics*. 3rd Edition. Academic Press, 2008.
- [67] Y. R. Shen. *The Principles of Nonlinear Optics*. New York: Wiley, 1984.
- [68] Moran Chen. “Large-scale cluster-state entanglement in the quantum optical frequency comb”. In: *University of Virginia Thesis* (2015).
- [69] Pei Wang. “Weaving the Quantum Optical Frequency Combs into Hypercubic Cluster States”. In: *University of Virginia Thesis* (2016).
- [70] R. W. P. Drever et al. “Laser phase and frequency stabilization using an optical resonator”. In: *Appl. Phys. B* 31 (1983), pp. 97–105.
- [71] Eric D. Black. “An introduction to Pound–Drever–Hall laser frequency stabilization”. In: *Am. J. Phys.* 69.1 (2001), pp. 79–87.
- [72] Gary C. Bjorklund. “Frequency-modulation spectroscopy: a new method for measuring weak absorptions and dispersions”. In: *Opt. Lett.* 5 (1980), p. 15.
- [73] Horace P. Yuen and Jeffrey H. Shapiro. “Optical Communication with Two-Photon Coherent States- Part III: Quantum Measurements Realizable with Photoemissive Detectors”. In: *IEEE Trans. Inform. Theory* 26 (1980), p. 78.

- [74] R. E. Slusher et al. “Observation of squeezed states generated by four-wave mixing in an optical cavity”. In: *Phys. Rev. Lett.* 55 (1985), p. 2409.
- [75] F. A. S. Barbosa et al. “Beyond Spectral Homodyne Detection: Complete Quantum Measurement of Spectral Modes of Light”. In: *Phys. Rev. Lett.* 111 (20 Nov. 2013), p. 200402. DOI: [10.1103/PhysRevLett.111.200402](https://doi.org/10.1103/PhysRevLett.111.200402). URL: <https://link.aps.org/doi/10.1103/PhysRevLett.111.200402>.
- [76] Chun-Hung Chang. “Stability and Performance Improvement of a Cluster State Generator for Universal Quantum Computing”. In: *University of Virginia Thesis* (2021).
- [77] M. Shirasaki. “Large angular dispersion by a virtually imaged phased array and its application to a wavelength demultiplexer”. In: *Opt. Lett.* 21.5 (1996), pp. 366–368.
- [78] A. M. Weiner A. Vega and C. Lin. “Generalized grating equation for virtually-imaged phased-array spectral dispersers”. In: *Appl. Opt.* 42.20 (2003), pp. 4152–4155.
- [79] Shijun Xiao, Andrew M. Weiner, and Christopher Lin. “A Dispersion Law for Virtually Imaged Phased-Array Spectral Dispersers Based on Paraxial Wave Theory”. In: *IEEE J. Quantum Electron.* 40 (2004), p. 420.
- [80] C. M. Caves. “Quantum-mechanical noise in an interferometer”. In: *Phys. Rev. D* 23 (1981), p. 1693.
- [81] The LIGO Collaboration. “A gravitational wave observatory operating beyond the quantum shot-noise limit”. In: *Nat Phys* 7.12 (Dec. 2011), pp. 962–965. URL: <http://dx.doi.org/10.1038/nphys2083>.

- [82] The LIGO Scientific Collaboration. “Advanced LIGO”. In: *arXiv:1411.4547 [gr-qc]* (2014).
- [83] Onur Hosten et al. “Measurement noise 100 times lower than the quantum-projection limit using entangled atoms”. In: *Nature* 529.7587 (Jan. 28, 2016), pp. 505–508. URL: <http://dx.doi.org/10.1038/nature16176>.
- [84] Henning Vahlbruch et al. “Detection of 15 dB Squeezed States of Light and their Application for the Absolute Calibration of Photoelectric Quantum Efficiency”. In: *Phys. Rev. Lett.* 117 (11 Sept. 2016), p. 110801. DOI: [10.1103/PhysRevLett.117.110801](https://doi.org/10.1103/PhysRevLett.117.110801). URL: <http://link.aps.org/doi/10.1103/PhysRevLett.117.110801>.
- [85] H. Zaidi et al. “Entangling the optical frequency comb: simultaneous generation of multiple 2x2 and 2x3 continuous-variable cluster states in a single optical parametric oscillator”. In: *Laser Phys.* 18 (2008). Revised version at <http://arxiv.org/pdf/0710.4980v3>, p. 659.
- [86] S. L. Braunstein and P. van Loock. “Quantum information with continuous variables”. In: *Rev. Mod. Phys.* 77.2, 513 (2005), p. 513. DOI: [10.1103/RevModPhys.77.513](https://doi.org/10.1103/RevModPhys.77.513).

Appendices

Appendix A

Quadrature derivations in quantum heterodyne detection

Based on the vacuum mode involved quantum heterodyne detection method discussed in Section 5.4, using the FT results in Eq. (5.33) and Eq. (5.34), the mathematical derivations cluster state covariance matrix, \mathbf{V} and \mathbf{U} matrices will be shown in this appendix.

For the case where the LO beats with signal modes as well as the vacuum modes, the average of the vacuum quadratures and the average of multiples of vacuum quadratures are either 0 or constant value as below

$$\langle Q_v \rangle = \langle P_v \rangle = 0, \quad (\text{A.1})$$

$$\langle Q_v^2 \rangle = \frac{1}{2} \langle (a + a^\dagger)^2 \rangle = \frac{1}{2}, \quad (\text{A.2})$$

$$\langle P_v^2 \rangle = -\frac{1}{2} \langle (a - a^\dagger)^2 \rangle = \frac{1}{2}, \quad (\text{A.3})$$

$$\langle Q_v P_v \rangle = \frac{i}{2}, \quad (\text{A.4})$$

$$\langle P_v Q_v \rangle = -\frac{i}{2}. \quad (\text{A.5})$$

These conditions make it possible to get the expectations of quadratures for the modes that we want to measure.

For a N-mode cluster state, we construct a column vector \mathbf{x} that contains all the quadratures

$$\mathbf{x} = \begin{pmatrix} \mathbf{Q} \\ \mathbf{P} \end{pmatrix}, \quad (\text{A.6})$$

where $\mathbf{Q} = (Q_1, Q_2 \dots Q_N)^T$ and $\mathbf{P} = (P_1, P_2 \dots P_N)^T$. For a Gaussian state that has zero mean value, the unique covariance matrix is [31]

$$\text{Cov } \mathbf{x} = \frac{1}{2} \langle \{ \mathbf{x}^\dagger, \mathbf{x}^T \} \rangle, \quad (\text{A.7})$$

where the anticommutator product is defined as

$$\{ \mathbf{x}^\dagger, \mathbf{y}^T \} = \mathbf{x} \mathbf{y}^T + (\mathbf{y} \mathbf{x}^T)^T. \quad (\text{A.8})$$

The covariance matrix thus can be expressed as matrix blocks

$$\text{Cov } \mathbf{x} = \begin{pmatrix} \text{Cov}[\mathbf{Q}, \mathbf{Q}] & \text{Cov}[\mathbf{Q}, \mathbf{P}] \\ \text{Cov}[\mathbf{P}, \mathbf{Q}] & \text{Cov}[\mathbf{P}, \mathbf{P}] \end{pmatrix} \quad (\text{A.9})$$

with each block has the expression

$$\text{Cov}[Q_i, Q_j] = Q_i Q_j, \quad (\text{A.10})$$

$$\text{Cov}[P_i, P_j] = P_i P_j, \quad (\text{A.11})$$

$$\text{Cov}[Q_i, P_j] = \begin{cases} Q_i P_j & \text{for } i \neq j, \\ \frac{1}{2}(Q_i P_j + P_j Q_i) & \text{for } i = j, \end{cases} \quad (\text{A.12})$$

$$\text{Cov}[P_i, Q_j] = \begin{cases} P_i Q_j & \text{for } i \neq j, \\ \frac{1}{2}(P_i Q_j + P_j P_i) & \text{for } i = j. \end{cases} \quad (\text{A.13})$$

For frequency component Ω_i , the FT real and imaginary have the expression

$$R_i = \cos\theta(Q_i + Q_{vi}) - \sin\theta(P_i + P_{vi}), \quad (\text{A.14})$$

$$I_i = \sin\theta(-Q_i + Q_{vi}) + \cos\theta(-P_i + P_{vi}). \quad (\text{A.15})$$

where, Q_i and P_i are the amplitude and phase quadrature of signal mode, Q_{vi} and P_{vi} are the quadratures of vacuum. Using the quadrature relations for vacuum state, the signal mode quadrature combinations are given by

$$Q_i P_j = (I_i I_j - R_i R_j) \sin\theta \cos\theta - R_i I_j \cos^2\theta + I_i R_j \sin^2\theta, \quad (\text{A.16})$$

$$P_i Q_j = (I_i I_j - R_i R_j) \sin\theta \cos\theta + R_i I_j \sin^2\theta - I_i R_j \cos^2\theta, \quad (\text{A.17})$$

$$Q_i Q_j = -(R_i I_j + I_i R_j) \sin\theta \cos\theta + I_i I_j \sin^2\theta + R_i R_j \cos^2\theta, \quad (\text{A.18})$$

$$P_i P_j = (R_i I_j + I_i R_j) \sin\theta \cos\theta + I_i I_j \cos^2\theta + R_i R_j \sin^2\theta. \quad (\text{A.19})$$

Knowing the covariance matrix, it is easy to get the cluster state \mathbf{U} and \mathbf{V} matrices,

which can be calculated as

$$\mathbf{U} = 2\text{Cov}[\mathbf{Q}, \mathbf{Q}]^{-1}, \quad (\text{A.20})$$

$$\mathbf{V} = 2\text{Cov}[\mathbf{P}, \mathbf{Q}]\mathbf{U}. \quad (\text{A.21})$$

Appendix B

Virtually imaged phase array for qumode separation

Virtually imaged phased array (VIPA) is an optical spectral disperser that was first demonstrated by M. Shirasaki in 1996 [77]. Compared to the common diffraction gratings, VIPA has the advantages including large angular dispersion, low dependence of polarization, simple and compact structure.

In this chapter, I will first introduce the basic setup of VIPA and the Fresnel approximation model. Then, I will provide the simulation based on several parameters. Finally, I will show the experimental design with preliminary results, and analyze the possibility of being used to separate quantum modes.

B.1 Basic principles

B.1.1 Setup

VIPA can be described as a modified Fabry Perot etalon. The setup is shown in Fig. B.1 [77]. It consists of two parallel glass plates separated by a distance of t . The

the entry side glass plate has a small window that is anti-reflected (AR) coated with reflectance $R = 0$ and other area is coated with reflectance $R_1 \approx 1$. The transmitted glass plate is coated with $R_2 \geq 0.95$. A collimated beam is focused by a cylindrical lens. It enters the VIPA through the small AR coated window with an incident angle θ and the beam waist position is at the transmitted plate. The laser beam is reflected back and forth multiple times between two plates. The output fields can be viewed as the interference between many diverging beams generated from virtual source of individual virtual images of the beam waists, which are as a phase array. The phase difference between the array elements (virtual sources) is frequency dependent, the direction of the output beam varies with frequency, which makes the VIPA a spectral disperser.

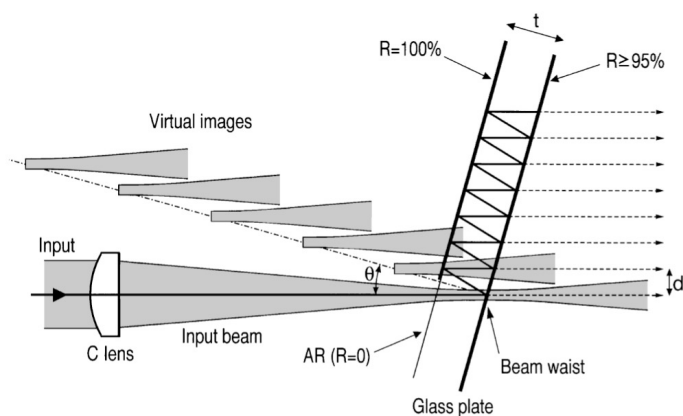


Figure B.1: VIPA setup [77]. A glass plate that is 100 mm thick has 95%-reflection coating on the right surface and 100%-reflection coating on the left surface. There is a window area on the left surface, which has antireflection coating (AR) instead of 100%-reflection coating. The glass plate produces many beams diverging from individual virtual images of the beam waist. These beams interfere and form collimated light.

The spectral dispersion law was derived based on different theories. One dispersion law was derived by Vega [78] using plane wave theory and tested to match well with experimental data using relatively large incident angles ($\theta > 5^\circ$). For small inci-

dent angles, another modified dispersion law proposed by Shijun Xiao [79] is a result from the Fresnel diffraction theory with paraxial wave approximation and Gaussian beam model. It approaches to the same results as the plane wave theory for large incident angle and the small angle results are also verified by experiments. In the next part, I will briefly summarize the Gaussian beam based dispersion law from Shijun Xiao's work.

B.1.2 Fresnel approximation

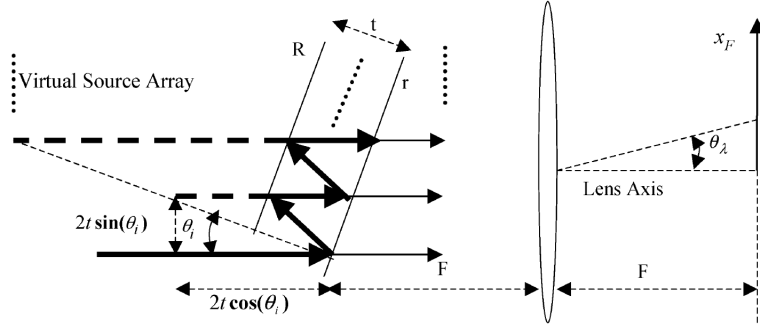


Figure B.2: VIPA geometry [79]. θ_i is the incident angle. θ_λ is the dispersion angle of the output light from VIPA. F is the focal length of the convex lens after VIPA.

Fig.B.2 shows the geometric relations of the virtual sources array. The displacement of the n th virtual resource can be calculated from the geometric relations. The transverse (Δx_n) and longitudinal (Δy_n) displacement are

$$\Delta x_n = n_0 2t \sin \theta_i, \quad (\text{B.1})$$

$$\Delta y_n = n_0 2t \cos \theta_i, \quad (\text{B.2})$$

where $n = 0, 1, 2, \dots$, θ_i is the incident angle, t is the distance two reflective plates, n_0 is the refraction index of the medium between two plates and from now on we will

only consider the medium of air, which gives $n_0 = 1$. The field of n th virtual source is a Gaussian beam in the form of

$$E_n(x) = (Rr)^n E_0 \exp\left[-\frac{(x - \Delta x_n)^2}{w_0^2}\right], \quad (\text{B.3})$$

where R is the reflectance of the VIPA left plate and r is the reflectance of the VIPA right plate. E_0 is the initial amplitude. w_0 is the beam waist of the incident light. A lens is used to focus the field, the focal length of which is F . Assuming the waves are paraxial and using the Fresnel approximation, the spacial Fourier transform of a thin lens gives the output field

$$E_{out}(x_F, \lambda) = \frac{i}{\lambda F} \exp(-ikF) \exp(-ikd) \exp\left[i\pi \frac{d-F}{\lambda F^2} x_F^2\right] \mathbf{F}(\nu_x) \quad (\text{B.4})$$

where ν_x is the spacial frequency and $\mathbf{F}(\nu_x)$ is the Fourier transform of the input field. With far field approximation that F is very long, the output angle satisfies $\theta_\lambda \approx x_F/F \approx \lambda \nu_x$. The Fourier transform is

$$\mathbf{F}(\nu_x) = \mathbf{F}\left(\frac{x}{\lambda F}\right) = \int_{-\infty}^{\infty} E_{in}(x) \exp\left(i2\pi \frac{x_F x}{\lambda F}\right) dx. \quad (\text{B.5})$$

Considering the n th virtual source has the displacement

$$d_n = F + \Delta y_n \quad (\text{B.6})$$

Substituting Eq. (B.1), Eq. (B.3) and Eq. (B.6) into Eq. (B.4) to get the output field of the n th virtual source and then summarizing all the virtual source output field to

get the intensity distribution as

$$I_{out}(x_F, \lambda) = |E_{out}(x_F, \lambda)|^2 \propto \exp\left(-\frac{2f^2 x_F^2}{F^2 W^2}\right) \frac{1}{(1 - R_1 R_2)^2 + 4R_1 R_2 \sin^2\left(\frac{k\Delta}{2}\right)}, \quad (\text{B.7})$$

where

$$\Delta = 2t\cos\theta_i - 2t\sin\theta_i \frac{x_F}{F} - t\cos\theta_i \frac{x_F^2}{F^2}. \quad (\text{B.8})$$

With the Fresnel paraxial approximation, $x_F/F \approx \theta_\lambda$. In Eq. B.7, when $k\Delta = 2m\pi, m = 0, 1, 2, \dots$, the intensity has the maximum value. The phase matching equation is

$$k [2t\cos\theta_i - 2t\sin\theta_i \theta_\lambda - t\cos\theta_i \theta_\lambda^2] = 2m\pi. \quad (\text{B.9})$$

We define the central wavelength λ_0 when $\theta_\lambda = 0$, so that

$$m\lambda_0 = 2t\cos\theta_i. \quad (\text{B.10})$$

Therefore the output field wavelength λ depends on the output angle θ_λ as

$$\lambda - \lambda_0 = -\lambda_0 [(\tan\theta_i)\theta_\lambda + \frac{1}{2}\theta_\lambda^2], \quad (\text{B.11})$$

and the spectral dispersion law is

$$\frac{d\lambda}{d\theta_\lambda} = -\lambda_0 [(\tan\theta_i) + \theta_\lambda], \quad (\text{B.12})$$

which only depends on the incident angle θ_i .

B.2 Experimental and simulation results

B.2.1 Setup design

We built a VIPA using two flat mirrors with air between them to successfully separate light at 1064 nm with frequency difference of about 979 MHz. The experimental setup is shown in Fig.B.3. The laser with frequency 1064 nm is phase modulated

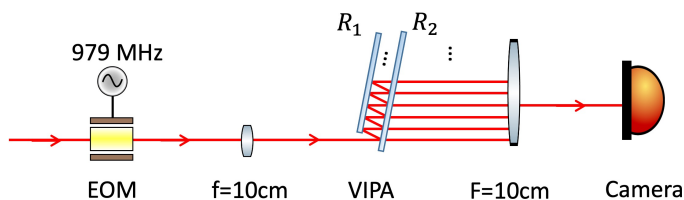


Figure B.3: Schematic setup of VIPA.

at 979.087 MHz. VIPA has two flat mirrors with reflectance $R_1 = 99.99\%$ and $R_2 = 97.5\%$. The distance between these two mirrors is about 2 cm. A lens before the first mirror focuses the beam waist to be exactly on the second mirror, the beam waist of which is $84.86 \mu\text{m}$. After R_2 , the fields are focused by a lens with focal length $F = 10 \text{ cm}$ and a camera is used to observe the interference pattern. Fig.B.4 (a) shows the interference pattern when the EOM is turned off and all the fringes in this picture have the same frequency. There are 4 orders of constructively interfered fringes. Fig.B.4 (b) shows the pattern when EOM is turned on and the 979 MHz sidebands appear as there are three bright fringes in each order.

However, the loss of this system is very large caused by two factors. The first is the diffraction fringes. Since the flat mirrors used to built VIPA have thickness of 5 mm and the incident beam is very close to the edges, this cause the diffraction fringes both when EOM is on and off. The second factor is there are more than one

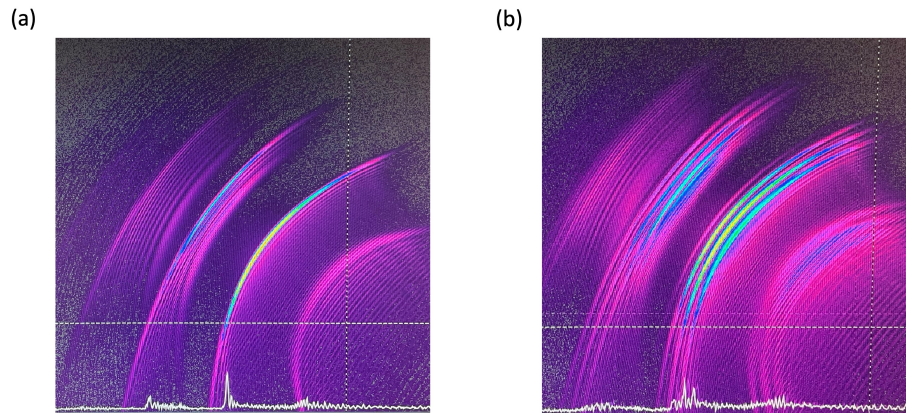


Figure B.4: VIPA separates frequencies with difference of 979 MHz. (a) EOM turned off. (b) EOM turned on.

orders of fringes, which are the higher orders of VIPA. I will show what parameters can influence the higher order fringes by plotting simulation results of the intensity distribution in the following part.

B.2.2 Discussion

There are several parameters that will influence the interference pattern of VIPA. These parameters are the inserting angle θ_i , distance t , between two VIPA mirrors, the reflectance of two mirrors R_1 and R_2 , and the beam waist w . In this section, I will shown how these parameters affect the interference pattern in terms of the angular dispersion, FSR and linewidth, based on the experimental setup we have.

Spectral dispersion

Wavelength dispersion is given by Eq. (B.12). The spectral dispersion only depends on the incident angle θ_i . Smaller incident angle gives a larger wavelength dispersion. Here I present some numerical simulation results of the output field intensity distribution

by setting $R = 99.99\%$, $r = 97.5\%$, $t=2$ cm, $f = 10$ cm, $W = 0.000349$ m and changing the incident angle to 1° , 2° , 3° and 4° . The intensity distribution is shown in Fig.B.5. The bright lines indicate the constructively interfered pattern. The slope of the bright line is the spectral dispersion. Small slope means that for the same frequency difference, the angular separation is larger. It verifies that smaller the inserting angle gives larger the spectral dispersion. Therefore, to separate the 1 GHz better, we need a smaller θ_i .

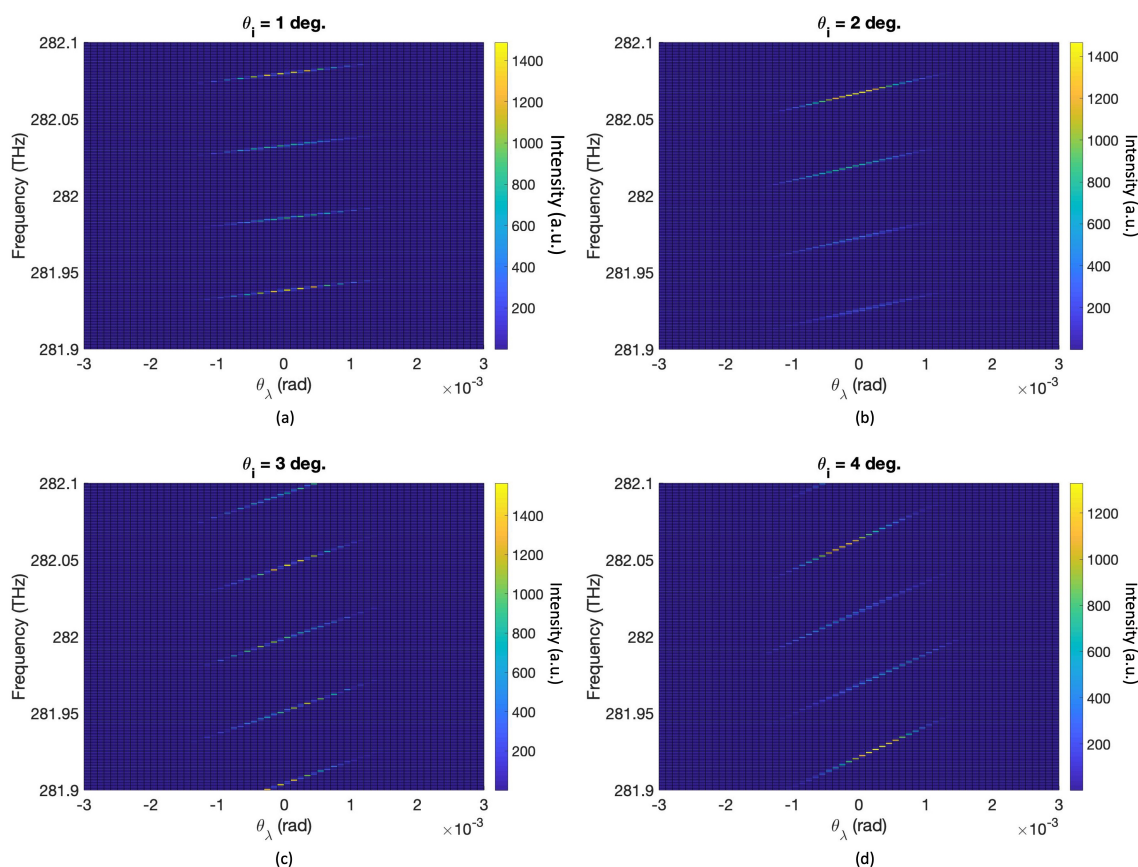


Figure B.5: VIPA intensity distribution for different incident angles.

Free spectral range

Free spectral range (FSR) of a VIPA can be calculated from Eq. (B.9):

$$\text{FSR} = \frac{c}{t(2\cos\theta_i - 2\theta_\lambda\sin\theta_i - \theta_\lambda^2\cos\theta_i)}. \quad (\text{B.13})$$

For small θ_i and θ_λ , we have the approximation that $\text{FSR} \approx \frac{c}{2t}$, which is the expression of an optical cavity. With $R_1 = 99.99\%$, $R_2 = 97.5\%$, $f = 10\text{cm}$ and $\theta_i = 3^\circ$ fixed, Fig.B.6 shows the intensity distribution plots for t equal to 1 cm, 2 cm, 3 cm, 4 cm. The FSR of the VIPA is the frequency difference of the nearest two constructive interference at the same angle. Increasing t results smaller FSR. In order to avoid the case that multiple frequencies are mixed at the same output angle and one frequency has constructively interference at different angles, larger FSR is needed.

Beam size

In VIPA setup, both the initial beam waist w and the focal length f of the lens before VIPA will determine beam waist incidenting on the second mirror of VIPA and further influence the size of the output interference field. With setting $R_1 = 99.99\%$, $R_2 = 97.5\%$, $t=2\text{ cm}$, $f = 10\text{cm}$, $\theta_i = 3^\circ$, for fixed $f = 10\text{cm}$, the intensity distribution plots with different initial beam waist $w = 349\mu\text{m}$ and $w = 1396\mu\text{m}$ are shown in Fig.B.7. Larger beam waist makes a larger interference field, making the single frequency light distributed over a larger range of output angles, which corresponding to the higher order fringes we observed in our experiment shown in Fig.B.4.

On the other hand, for fixed $w = 349\mu\text{m}$, the intensity distribution results are pollted in Fig.B.8 for different focal length $f = 10\text{cm}$, 2cm . Smaller focal length makes

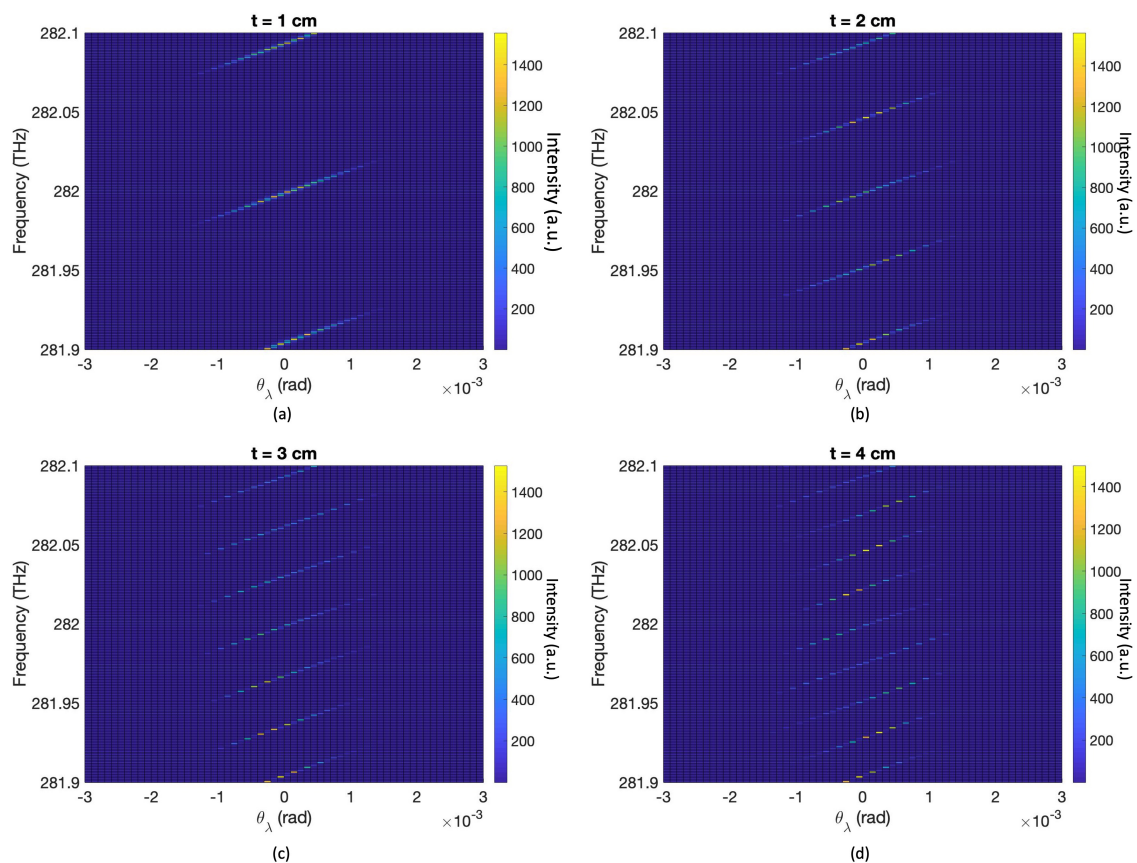


Figure B.6: VIPA intensity distribution for different distance t between two flat mirrors.

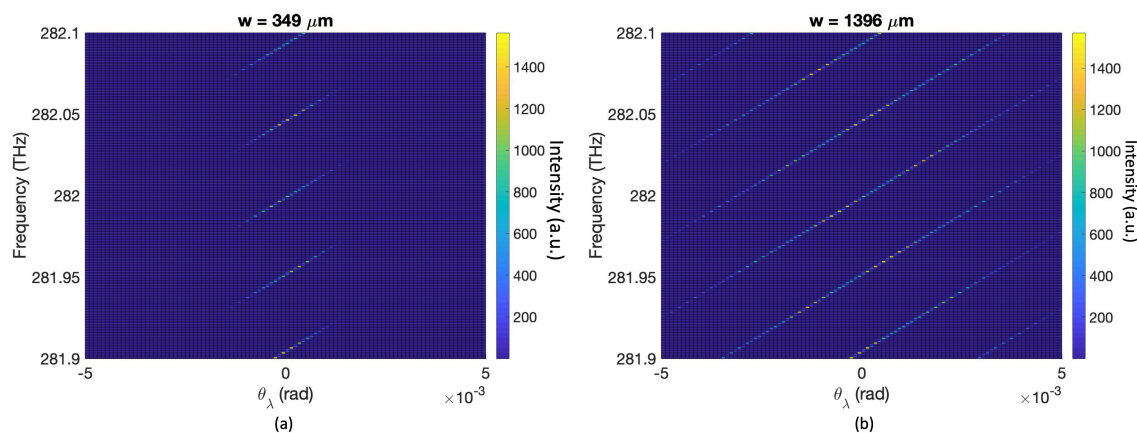


Figure B.7: VIPA intensity distribution for different initial beam waist.

the Gaussian beam diverging faster resulting a larger size of output field. Therefore, to avoid interference at large output angle, small focal length is needed.

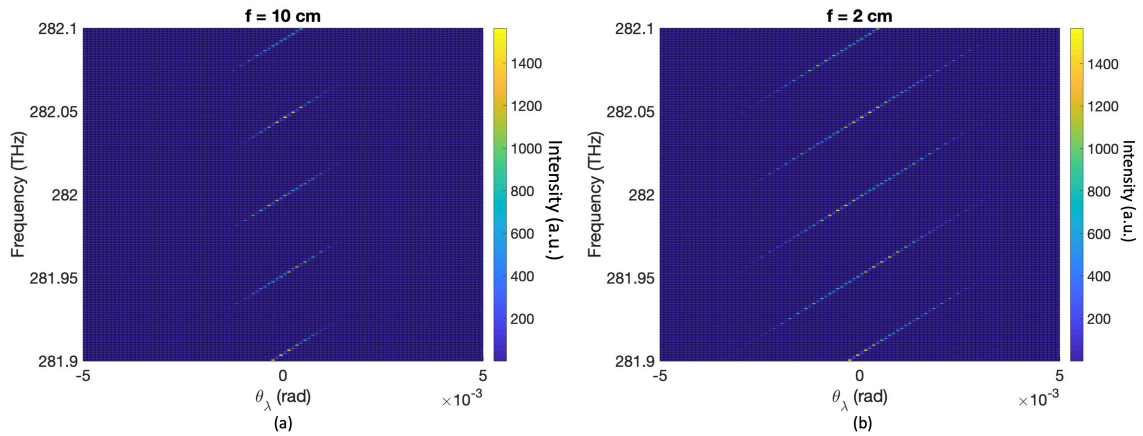


Figure B.8: VIPA intensity distribution for different focal length f before VIPA.

Finesse

The finesse of VIPA is determined by the reflectance of the second mirror r (which is served as the output coupler in an optical cavity). With $R = 99.99\%$, $t=2$ cm, $f = 10\text{cm}$, $\theta_i = 3^\circ$, $f = 10\text{cm}$ fixed, changing the reflectance of two flat mirrors $r = 0.975, 0.5$, the intensity distribution are plotted in Fig.B.9. Higher reflectance gives a higher finesse, resulting the frequencies are better separated.

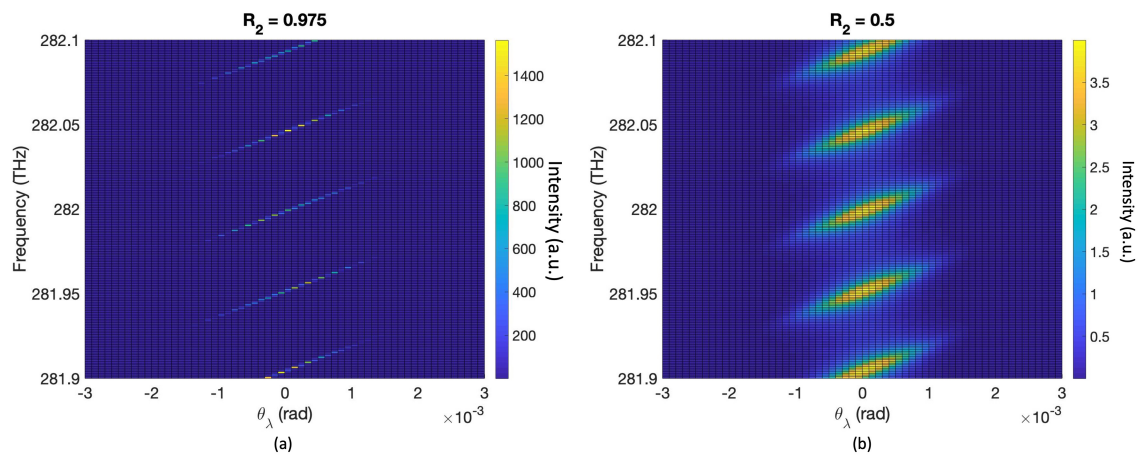


Figure B.9: VIPA intensity distribution for different reflectance r .

Appendix C

Pulsed-squeezing quantum states

Highly squeezed states are a crucial resource for quantum technologies such as quantum sensing, quantum metrology [80, 81, 82] and quantum computing [37, 3]. Squeezing can be defined as quantum noise reduction below the level of minimum uncertainty with both variances equal (e.g. $\Delta Q = \Delta P = \sqrt{\hbar/2}$) that defines the vacuum-induced shot-noise limit of classical systems. Recently, record levels of quantum noise reduction have been obtained in widely different physical systems, such as spin squeezing in cavity QED atomic systems (20 dB) [83], or quadrature squeezing in optical fields in the optical parametric oscillator (OPO, 15 dB) [84]. These squeezing levels are germane to the fault tolerance threshold of CV quantum computing, which is 20.5 dB of squeezing for an error rate of 10^{-6} [15].

The generation of highly squeezed states faces, as do other quantum resources such as entanglement, the daunting challenge of overcoming decoherence. For example, any residual absorption or scattering inside the OPO cavity is resonantly enhanced, which degrades the quantum correlations and therefore the squeezing level, e.g., 50% total loss limits total squeezing to 3 dB, 10% total loss limits total squeezing to 10 dB, 1% total loss limits total squeezing to 20 dB, etc. Intracavity losses are the main limitation on the current squeezing performance mentioned above.

In this chapter, I will theoretically show that it is possible, by pumping the OPO properly using a pulsed laser that has a frequency comb, to construct a large entangled

mode, which can be leveraged to increase the squeezing in one mode at the expense of all the others, by unitary redistribution. Furthermore, we generalized this discrete frequency entangled mode to a case without OPO cavity. We found the specific entanglement structure in a pulsed squeezing system, which forms super entangled modes in broadband spectrum. The squeezing of the super entangled mode can also be leveraged to form a highly squeezed eigen-quadrature.

C.1 Pulsed squeezing in optical parametric oscillator

We consider the generation of squeezing using spontaneously parametric down conversion in an OPO below threshold. The Interaction picture Hamiltonian for this process with a classical undepleted pump field can be written as

$$H = i\hbar \frac{\kappa}{2} \sum_{i=1}^N \sum_{j=1}^N G_{ij} a_i^\dagger a_j^\dagger + H.c., \quad (\text{C.1})$$

where $\kappa = \beta\chi$ is the coupling coefficient, product of the pump field amplitude β by the nonlinear susceptibility χ , and $a_{1,\dots,N}$ are the annihilation operators for N signal modes (OPO eigenmode). The $N \times N$ mode-coupling matrix \mathbf{G} is a symmetric matrix whose entries can only be zero or one, called the adjacency matrix of the \mathcal{H} -graph [85]. N can be very large, defined by the OPO mirrors' bandwidth and dispersion in the nonlinear material [62]. Therefore the Heisenberg equations are

$$\dot{\vec{Q}} = \mathbf{G}\vec{Q} \quad (\text{C.2})$$

$$\dot{\vec{P}} = -\mathbf{G}\vec{P} \quad (\text{C.3})$$

where $\vec{Q}=(Q_1, \dots, Q_N)^T$ and $\vec{P}=(P_1, \dots, P_N)^T$. These equations are solved by diagonalizing G , the eigenvalues giving the squeezing parameter(s) and the eigenvectors are the squeezed operator(s).

C.1.1 Single mode squeezing

Starting with the single-mode case ($N=1$), the corresponding \mathbf{G} matrix is $\mathbf{G} = (1)$. The \mathcal{H} -graph is shown in Fig.C.1. The black dot is the OPO mode 0 and the green line indicates the down-converted photon pair have the same frequency and populate the mode 0, which is entangled with itself. The squeezed phase quadrature $P_1(r)$ and anti-squeezed amplitude quadrature $Q_1(r)$ are given by solving the Heisenberg equation,

$$Q_1(r) = e^r Q_1, \quad (\text{C.4})$$

$$P_1(r) = e^{-r} P_1. \quad (\text{C.5})$$

The squeezing parameter is r .

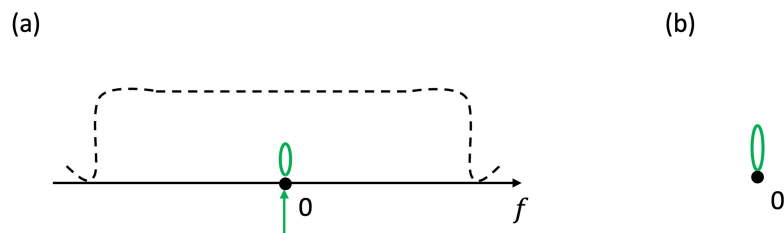


Figure C.1: (a) Single-mode squeezing mode frequency relations. Dashed line indicate the phase-matching bandwidth. Green arrow represents the half of pump frequency. There is only one pump frequency in this case. (b) Single-mode squeezing \mathcal{H} -graph.

C.1.2 N-fold single mode squeezing

The case of multimode ($N \geq 2$) squeezing becomes quite interesting if we consider the particular form of G that has all the elements equal to 1, $G_{ij} = 1, \forall(i, j)$. This kind of multimode squeezing can be generated by adding more pump modes with different frequencies to an OPO as shown in Fig.C.2 (a). The black dots on the axis are the OPO modes with frequency spacing at the free spectral range (FSR) of OPO. The arrows with different colors represent the half pump frequencies, which form a frequency comb realized by a pulsed laser, with equal frequency spacing at the FSR. The half of pump frequencies locate right at the resonance frequencies of OPO and the middle between the resonance frequencies. In this case, if we take N resonance mode of an OPO, there will be $2N + 1$ pump modes within the phase-matching bandwidth. All the resonance modes will be entangled together as shown in the \mathcal{H} -graph Fig.C.2 (b).

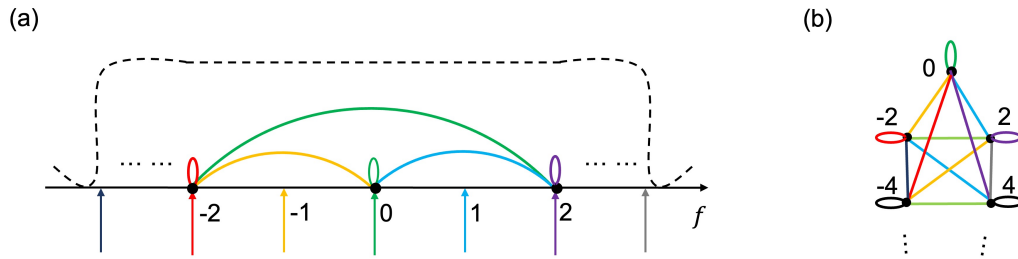


Figure C.2: (a) N-fold single-mode squeezing mode frequency relations. Dashed line indicate the phase-matching bandwidth. Arrows represents the half of pump frequency. (b) N-fold single-mode squeezing \mathcal{H} -graph.

Solving the Heisenberg equations for this system, the eigenvalues of this $N \times N$ adjacency matrix \mathbf{G} are $(N, 0, \dots, 0)$, and the eigenvectors related to nonzero eigenvalue is $\{(\sum_{i=1}^N Q_i), \dots, Q_i - Q_{j>i}, \dots\}$ (and similarly for P). Only the nonzero

eigenvalue results squeezing

$$\sum_{i=0}^N Q_i(r) = e^{Nr} \sum_{i=0}^N Q_i(0), \quad (\text{C.6})$$

$$\sum_{i=0}^N P_i(r) = e^{-Nr} \sum_{i=0}^N P_i(0). \quad (\text{C.7})$$

In this case, the only squeezed operator is the sum of all the phase quadrature, squeezed by Nr , and the anti-squeezed operator is the sum of all the amplitude quadrature, anti-squeezed by Nr . All other eigen-operators, associated with 0 eigenvalue, become constants of motion. It is important to note that no additional squeezing is introduced that wasn't there before, in line with Braunstein's notion of irreducibility [86]. One can view this as a squeezing redistribution from N modes into a single one, effected by the unitary operation which diagonalizes \mathbf{G} , i.e., an optical interferometer [86]. Because this redistribution occurs outside the squeezing emitter, it is not sensitive to the intrinsic physical limitations (e.g. intracavity losses in an OPO) that define the value of r , and it thereby leverages the easily accessible scalability of multimode squeezing. So we can call this state a N -fold single-mode squeezing.

For the N -fold single mode squeezing, the annihilation operator in Heisenberg picture is

$$a_m(t) = e^{-i\omega_m t} \frac{1}{N} \left\{ (\cosh Nr - 1) \sum_{j=1}^N a_j + \sinh Nr \sum_{j=1}^N a_j^\dagger + Na_m \right\}, \quad (\text{C.8})$$

where m is the mode number in one super squeezed mode. Thus the total mean photon number of the super squeezed vacuum is

$$\langle A^\dagger A \rangle = \frac{1}{N} \sinh^2 Nr \left(\sum_{j=1}^N e^{i\omega_j t} \sum_{j=1}^N e^{-i\omega_j t} \right), \quad (\text{C.9})$$

where A and A^\dagger are the sum of all the squeezed annihilation and creation operators.

C.2 Pulsed squeezing with nonlinear crystal

In the previous section, we have seen that use a frequency comb to pump a proper OPO can generate large entangled modes with frequencies are equally spaced at the FSR of OPO, which can be changed to get a confluent squeezing. In this section, we are going to present the entanglement structure generated by frequency comb without cavity, which will result in entangled states with unequally spaced frequency modes.

C.2.1 Two mode squeezing

Single mode squeezing we mentioned above is a degenerate case where the down-converted photons have the same frequency, which is the resonance frequency of the OPO. Considering the single pass nonlinear interaction (no OPO), it is more convenient to see the continuous down-converted spectrum within the phase-matching bandwidth. The two-mode squeezing, where the two down-converted photons have different frequencies, is shown in Fig.C.3. The two down-converted photons have the frequency $\omega_0 \pm \Omega$, where Ω varies in the full range of phase matching bandwidth. The corresponding qumodes can be represented by $a_{\omega_0 \pm \Omega}$ and $a_{\omega_0 \pm \Omega}^\dagger$. This two modes are entangled.

For two-mode squeezing, the adjacent G matrix of \mathcal{H} -graph is

$$\mathbf{G} = \begin{pmatrix} 0 & 1 \\ 1 & 0 \end{pmatrix}. \quad (\text{C.10})$$

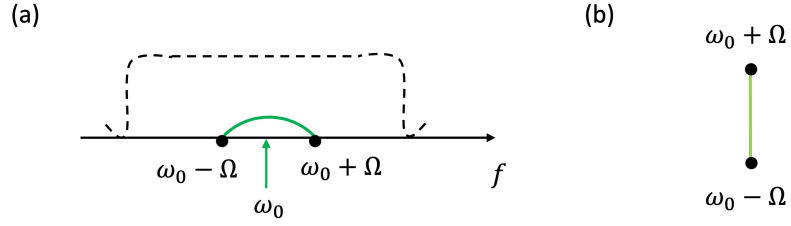


Figure C.3: (a) Two-mode squeezing mode frequency relations. Dashed line indicate the phase-matching bandwidth. Green arrow represents the half of pump frequency. (b) Two-mode squeezing \mathcal{H} -graph.

Solving the Heisenberg equations, we get the squeezed quadrature to be

$$Q_1(r) = e^r Q_1, \quad (\text{C.11})$$

$$P_1(r) = e^{-r} P_1, \quad (\text{C.12})$$

$$Q_2(r) = e^{-r} Q_2, \quad (\text{C.13})$$

$$P_2(r) = e^r P_2, \quad (\text{C.14})$$

where $Q_{1,2}(r) = Q_{\omega_0+\Omega}(r) \pm Q_{\omega_0-\Omega}(r)$ and $P_{1,2}(r) = P_{\omega_0+\Omega}(r) \pm P_{\omega_0-\Omega}(r)$. In this case, the the sum of phase quadrature and the different of the amplitude quadrature are squeezed, otherwise the sum of amplitude quadrature and the different of the phase quadrature are anti-squeezed, with the squeezing parameter r .

C.2.2 N-fold bipartite squeezing

Similar to the N-fold single mode squeezing mentioned before, using a frequency comb as pump fields can generate a super entangled mode (without OPO), which can be leveraged to achieve N-fold bipartite squeezing. As shown in Fig.C.4 (a), the colored arrows represent the frequency comb of pump modes, with each pump mode frequency equally separated by ω . The black dots represent qumodes. Two qumodes

are entangled if they are connected by the arc lines with different colors. The qumodes with frequencies $2n\omega \pm \Omega$ (n is an integer) form a super entangled mode. Within one super entangled mode, all the modes of frequencies $2n\omega + \Omega$ are entangled with the $2n\omega - \Omega$ modes, which form a bipartite entangled \mathcal{H} -graph, as shown in Fig.C.4 (b). However the modes in one super entangled mode are not entangled with other modes.

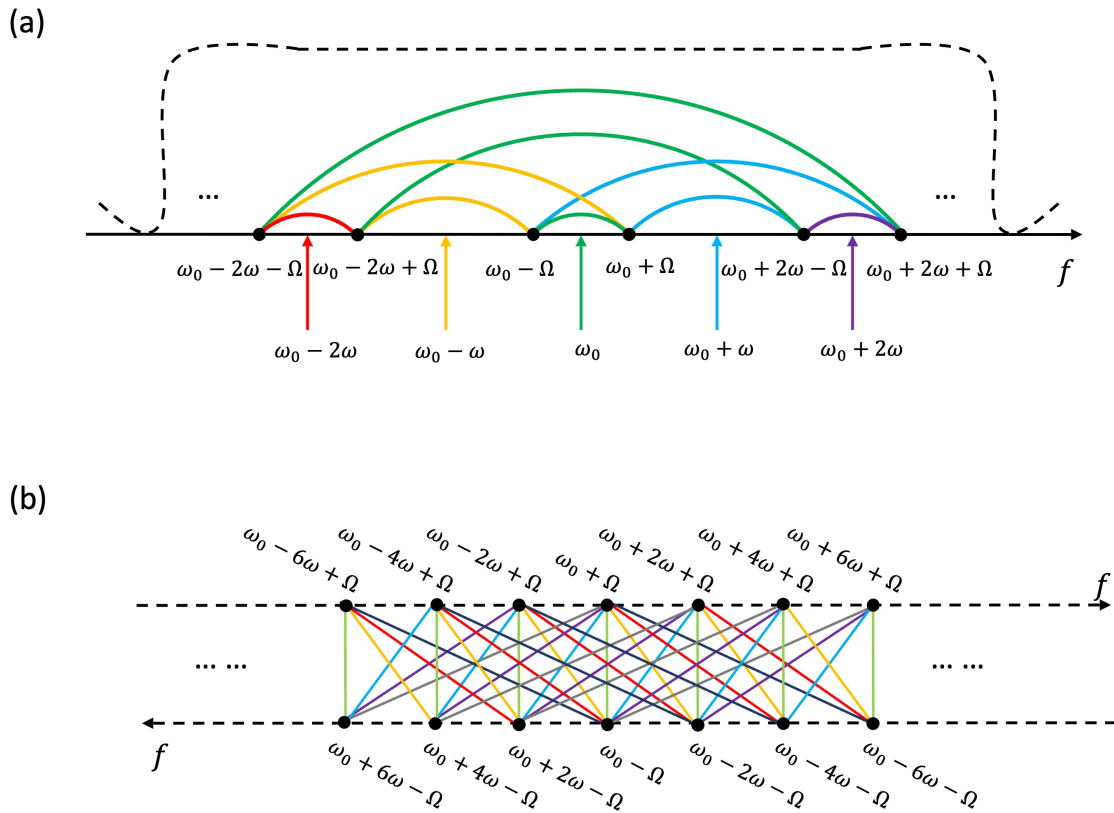


Figure C.4: (a) N-fold bipartite squeezing mode frequency relations. Dashed line indicate the phase-matching bandwidth. Arrows represents the half of pump frequency. (b) N-fold bipartite squeezing \mathcal{H} -graph.

The \mathbf{G} matrix for this N-fold bipartite entangled mode is now is a $2N \times 2N$

matrix, with $2N + 1$ pump modes taken into consideration,

$$\mathbf{G} = \begin{pmatrix} 0 & \dots & 0 & 1 & \dots & 1 \\ \vdots & \ddots & \vdots & \vdots & \ddots & \vdots \\ 0 & \dots & 0 & 1 & \dots & 1 \\ 1 & \dots & 1 & 0 & \dots & 0 \\ \vdots & \ddots & \vdots & \vdots & \ddots & \vdots \\ 1 & \dots & 1 & 0 & \dots & 0 \end{pmatrix}. \quad (\text{C.15})$$

The nonzero eigenvalues of this \mathbf{G} matrix are $\pm N$, with eigenvectors being

$$\sum_{i=0}^N Q_{i,+ \Omega}(r) \pm \sum_{j=N+1}^{2N} Q_{j,- \Omega}(r) \quad (\text{C.16})$$

respectively (similarly for P). This multimode squeezing is leveraged into a N -fold bipartite squeezing, with squeezing parameter being increased to Nr . The only squeezed and anti-squeezed operators are

$$Q_1(r) = e^{Nr} Q_1, \quad (\text{C.17})$$

$$P_1(r) = e^{-Nr} P_1, \quad (\text{C.18})$$

$$Q_2(r) = e^{-Nr} Q_2, \quad (\text{C.19})$$

$$P_2(r) = e^{Nr} P_2, \quad (\text{C.20})$$

where

$$Q_1(r) = \sum_{i=0}^N Q_{i,+\Omega}(r) + \sum_{i=1}^N Q_{j,-\Omega}(r), \quad (\text{C.21})$$

$$P_1(r) = \sum_{i=0}^N P_{i,+\Omega}(r) + \sum_{j=1}^N P_{j,-\Omega}(r), \quad (\text{C.22})$$

$$Q_2(r) = \sum_{i=0}^N Q_{i,+\Omega}(r) - \sum_{j=1}^N Q_{j,-\Omega}(r), \quad (\text{C.23})$$

$$P_2(r) = \sum_{i=0}^N P_{i,+\Omega}(r) - \sum_{j=1}^N P_{j,-\Omega}(r). \quad (\text{C.24})$$

The annihilation operator of the qumode with frequency $\omega_0 + 2n\omega \pm \Omega$ can also be solved in Heisenberg picture and the results are

$$\begin{aligned} a_{n,\pm\Omega}(t) = & e^{-i\omega_{n,\pm\Omega}t} \frac{1}{N} \left\{ (\cosh Nr - 1) \sum_{j=1}^N a_{j,\pm\Omega} \right. \\ & \left. + \sinh Nr \sum_{j=1}^N a_{j,\mp\Omega}^\dagger + N a_{j,\pm\Omega} \right\}. \end{aligned} \quad (\text{C.25})$$

The total mean photon number for one super squeezed vacuum mode is

$$\begin{aligned} \langle A^\dagger A \rangle = & \frac{1}{N} \sinh^2 Nr \left(\sum_{m=1}^N e^{i(m\omega_0+\Omega)t} \sum_{j=1}^N e^{-i(m\omega_0+\Omega)t} \right. \\ & \left. + \sum_{m=1}^N e^{i(m\omega_0-\Omega)t} \sum_{m=1}^N e^{-i(m\omega_0-\Omega)t} \right), \end{aligned} \quad (\text{C.26})$$

where A and A^\dagger are the sum of all the squeezed annihilation and creation operators.

Since we have shown that the modes in different family sets are not entangled, their optical field operators are not commute. The Hamiltonian of the whole pulsed squeezed system is the summation of all the different family sets decided by the value

of Ω ,

$$H_{all} = \int_0^\omega d\Omega H(\Omega) \quad (\text{C.27})$$

Thus the total intensity of the out put pulsed squeezing signal is just the sum of all the frequency modes in different family sets.

Conclusion

In this chapter, the entanglement structure of pulsed squeezing system was discussed. We found here that, every field operator can be solved exactly and expressed only by the frequency modes in one super entangled family set, with the squeezing parameter being changed to Nr . N is related to the pump mode numbers and is the eigenvalues of adjacency \mathbf{G} matrix of \mathcal{H} -graph. For a properly pulsed pumped OPO, the entanglement can be shown by a N-fold single-mode squeezing \mathcal{H} -graph, while for a pulsed pumped nonlinear crystal without optical cavity, the system is represented by N-fold bipartite entangled \mathcal{H} -graph.